POLYTECHNIC UNIVERSITY OF MARCHE

FACULTY OF ENGINEERING

Doctoral programme in Civil, Environmental, Building Engineering and Architecture

Final dissertation of Philosophiae Doctor

Nonlinear numerical approach to the analysis of Cross-Laminated Timber

Supervisor
Professor Stefano Lenci

Candidate
Agnese Scalbi

XXIX Edition

February 2017

Table of Contents

1 Research Project 19

1.1 Motivation 19

1.2 Research objectives 20

2 Properties of wood 21

2.1 Elastic orthotropic properties 22

2.2 Non-elastic properties 24

2.2.1 Failure types of wood 25

2.3 Natural characteristics affecting mechanical properties of wood 26

2.3.1 Reaction wood 26

2.3.2 Knots 26

2.3.3 Specific gravity 27

2.3.4 Annual ring orientation 27

2.3.5 Pitch pockets 28

2.3.6 Temperature and moisture content 29

2.4 Cross-laminated Timber Technology 29

2.4.1 Investigations on CLT: State of Art 31

2.4.2 European standardisation 35

3 Fracture mechanics and Damage mechanics 37

3.1 Linear Elastic Fracture Mechanics 38

3.1.1 Griffith's Work 38

3.1.2 Irwin's Work 39

3.2 Nonlinear Fracture Mechanics 40

3.3 Continuum Damage Mechanics 41

3.4 Smeared crack approach 42

4 Mechanical behavior of CLT panel under in-plane shear loads 44

4.1 The Cohesive Zone Model 47

5 Specimens *52*
5.1 Test setup 57
6 Discussion on experimental results *60*
7 Numerical modelling *72*
7.1 Initial modelling assumptions 73
7.2 Constitutive model for timber 75
7.3 Cohesive element 76
7.3.1 Fracture toughness: damage evolution 78
7.3.2 Interface strength was known 80
7.3.3 Interface strength was not known 82
7.3.4 Stiffness of the cohesive zone model 82
7.4 Viscous regularisation 83
8 Results *85*
8.1 Model performance without interface strength data 85
8.2 Model performance with adhesive strength data 101
8.2.1 Experimental data for adhesive strength 122
9 Conclusion *125*
9.1 New application and further research 128
BIBLIOGRAPHY *129*

List of figures:

Figure 2.1: three perpendicular axes: L (longitudinal), R (radial), T (tangential) on grain orientations **(Kretschmann 2010)**. 22

Figure 2.2: typical stress-strain curves for wood loaded in compression in L, R and T directions and for tension in the L direction. (**Holmberg et al. 1998**). 24

Figure 2.3: failure types in compression perpendicular to the grain: the crushing of earlywood under radial loading (a); buckling of growth rings under tangential loading (b); shear failure under loading at an angle to the growth rings (c). **(Gibson and Ashby, 1988)**. 25

Figure 2.4: failure types in tension parallel to the grain: splinter (a); shear and tension failure (b), shear failure (c) and pure tension failure (d). (**Feio, 2005**). 26

Figure 2.5: the direction of load in relation to the direction of annual growth rings: 90° or perpendicular (R), 45°, 0° or parallel (T). **(Kretschmann 2010)**. 28

Figure 3.1: fracture modes. Mode I is a normal opening mode, modes II and III are shear sliding modes **(Broek 1986)**. 40

Figure 3.2: total stress-strain curve (σ-ε) obtained by the sum of elastic strain ε_e and crack strain ε_c (**Jirásek 2016**). 43

Figure 4.1: superposition of load carrying mechanisms, (a) real shear stress τ_{net} (superposing b and c), (b) nominal shear stress τ_0 and (c) torsional stress τ_{tor} on the glueing interface. (**Bogensperger, Moosbrugger, and Schickhofer 2007**) 45

Figure 4.2: failure modes I, II and III (from left to right) in CLT element subjected to transversal forces in the plane direction **(Flaig and Blass 2013)**. 46

Figure 4.3: various forms of the traction-separation law used to define the cohesive zone models: a **(Needleman 1987)**, b **(Needleman 1990)**, c **(Hillerborg, Modeer, and Petersson 1976)**, d **(Bažant 2001)**, e **(Scheider and Brocks 2003)**, f **(Tvergaard and Hutchinson 1992)**. 49

Figure 5.1: specimens. 52

Figure 5.2: specimen S-1 has the shrinkage cracks (black lines) and presents knots in the external board (black arrows).Also, the red lines highlight the vacuum between the individual boards..... 54
Figure 5.3: specimen S-10 has the shrinkage cracks (black lines) and presents knots in the external board (black arrows). 54
Figure 5.4: specimen B12 has a cut (black lines) which interests half of the cross section of the external board and presents knots in the external board (black arrows)..... 55
Figure 5.5: specimen B14 has the shrinkage cracks (black lines) which interest the cross section of the external board. 55
Figure 5.6: specimen S-18 has the shrinkage cracks (black lines) which interest the cross section of the external board and presents knots in the external board (black arrows). 56
Figure 5.7: specimen S-19 has the shrinkage cracks (black lines) which interest the cross section of the external board. 56
Figure 5.8: specimen S-23 has the shrinkage cracks (black lines) which interest the cross section of the external board and presents knots in the external board (black arrows). 57
Figure 5.9: specimen S-24 has the shrinkage cracks (black lines) in the external board and the red lines highlight the vacuum between the individual boards..... 57
Figure 5.10: diagonal compression tests setup. 59
Figure 5.11: configuration for testing shear by loading in compression, including measurement of horizontal and vertical displacement. 59
Figure 6.1 representative load-displacement curves. 62
Figure 6.2: failure paths at the end of the shear test, lateral view of specimen S-5... 63
Figure 6.3: failure paths at the end of the shear test, frontal view (left) and bottom side (right) of specimen S-4. 64
Figure 6.4: failure paths at the end of the shear test, the bottom side of specimen S-15. 64
Figure 6.5: damaged configuration at the end of the shear test of specimen S-20. . 65

Figure 6.6: failure paths at the end of the shear test, lateral view (left) and a frontal view (right) of specimen S-20..... 65
Figure 6.7: failure paths at the end of the shear test, lateral view (left) and a frontal view (right) of specimen S-24..... 66
Figure 6.8: internal stress pattern in a 5-layers CLT element **(Andreolli, Rigamonti, and Tomasi 2014)**..... 68
Figure 6.9: calculated strength values for the specimens tested for shear stress perpendicular to the grain (τ_{yz}) compared to the strength value (12.8 MPa) reported in **(Jobstl, Bogensperger, and Schickhofer 2008)**, horizontal line..... 70
Figure 6.10: calculated strength values for the specimens tested for torsional stress (τ_{tor}) compared to the strength value (3.60 MPa) reported in **(Blass and Goerlacher 2002)**, horizontal line. 71
Figure 7.1: 3D FEM, partitioning of CLT specimens: a) five wooden layers and four cohesive elements and their finite element meshes; b) friction surface and its mesh. 74
Figure 7.2: response of cohesive element, linear softening (left) and exponential softening (right)..... 77
Figure 7.3: interaction between normal and shear separation. 80
Figure 8.1: load-displacement curves on varying of the ductility in the cohesive element. 87
Figure 8.2: specimens S-12, failure at the end of the test, failure load equal to 452.70 kN..... 88
Figure 8.3: finite element model for case II from maximum load reached in the simulation equal to 431 kN (a); at load equal to 363 kN (b); at load 234 kN (c) and at final load equal to 210 kN (d).Legend: MPa. 89
Figure 8.4: load-displacement curves on varying of the viscous parameters..... 90
Figure 8.5: load-displacement curves on varying of the friction coefficient. 92
Figure 8.6: load-displacement curves on varying of the ductility in the cohesive elements to different mesh size..... 94

Figure 8.7: finite element model for the CASE I_a at the first sliding of the layers at the displacement increment about of 3mm (276 kN). Legend: MPa. 95
Figure 8.8: finite element model for the CASE I_a at the load reached about of 569 kN and applied displacement equal to 7.7 mm. Legend: MPa. 95
Figure 8.9: finite element model for the CASE I_a at the reached load about of 587 kN and applied displacement equal to 9.2 mm. Legend: MPa. 96
Figure 8.10: finite element model for the CASE II_a at the first sliding of the layers at the reached load about of 335 kN and applied displacement equal to 3.4 mm. Legend: MPa. 96
Figure 8.11: finite element model for the CASE II_a at the maximum load reached about of 657 kN and applied displacement equal to 8.7 mm. Legend: MPa. 97
Figure 8.12: finite element model for CASE III_a at the maximum load reached about of 545 kN and applied displacement equal to 6.1 mm. Legend: MPa. 98
Figure 8.13: finite element model for CASE III_a at the reached load about of 343 kN and applied displacement equal to 8.3 mm. Legend: MPa. 98
Figure 8.14: load-displacement curves on varying of the damage initiation ratio. ..100
Figure 8.15: load-displacement curves obtained with different interface stiffness. ..103
Figure 8.16: progressive damage evolution in Zou et al. model: a) reached load equal to 526 kN corresponds to the failure of the friction surface at displacement 6.5 mm; b)and c)reached load 537 kN (maximum load reached in the simulation) and applied displacement equal to 7.7 mm. Legend: MPa. 105
Figure 8.17: failure of the CLT element with stiffness value from Diehl's formulation: case I at maximum displacement equal to 7 mm that corresponds at load 362 kN. Legend: MPa. 106
Figure 8.18: failure of the CLT element with stiffness value from Diehl's formulation: case II at maximum displacement about 8 mm that corresponds at load 234 kN. Legend: MPa. 107

Figure 8.19: failure of the CLT element with stiffness value from Turon's formulation, case IV, at maximum displacement about 7.4 that corresponds at load 336 kN. Legend: MPa. 108

Figure 8.20: contours of tensile stresses in the cohesive layer between external and internal layers from reached load equal to 185 kN (about 2mm) (a) to final step increment that corresponds to reached load equal to 342 kN (about 7 mm) (d) by Turon's formulation, case IV. Legend: MPa. 110

Figure 8.21: contours of tensile stresses in the cohesive element between internal layers from reached load equal to 185 kN, (about 2mm) (a) to final step increment that corresponds to reached load equal to 342 kN, (about 7 mm) (c) by Turon's formulation, case IV. Legend: MPa. 111

Figure 8.22: contours of the shear stresses in the cohesive element between the external and internal layers (left side) and between the internal layers (right side), by Turon's formulation, case IV. Legend: MPa. 113

Figure 8.23: load-displacement curves obtained with two different approaches, Diehl vs. Turon. 114

Figure 8.24: load-displacement curves obtained by setting stiffness and shear strength (perpendicular to the grain and the rolling shear) from the experimental results. ...116

Figure 8.25: failure of the CLT element with calibrated model, case with normal stiffness equal to 10^5 N/mm^{3}and interface strength equal to 16.2 MPa. Legend: MPa. 117

Figure 8.26: contours of tensile stresses in the cohesive element between the external and internal layers (left side) and between the inner layers (right side). From applied displacement equal to 4mm(a) to final load reached 360 kN and applied displacement equal to 5.6mm (c), case with normal stiffness equal to 10^5 N/mm^3 and interface strength equal to 16.2 MPa. Legend: MPa.....118

Figure 8.27: contours of the shear stresses in the cohesive element between the external and internal layers (left side) and between the internal layers (right side). From applied displacement equal to 4mm (a) to final load reached 360 kN and applied displacement equal to5.6mm (c), case with normal stiffness equal to 10^5 N/mm^3 and interface strength equal to 16.2 MPa Legend: MPa.....119

Figure 8.28: load-displacement curves obtained by setting normal (k_n) and tangential (k_s) stiffness with shear strength (perpendicular to the grain and the rolling shear) from the experimental results. 120
Figure 8.29: load-displacement curves obtained by setting a lower shear modulus to characterise the timber material (CASE I), and by setting a higher fracture energy to characterise the cohesive interfaces (CASE II). 121
Figure 8.30: specimens during the test in the shearing machine (left), specimen 9 after the shear test (right, 90% wood failure). 123
Figure 8.31: glue line 12_II (100%wood failure). 123

List of tables:

Table 1: torsional shear strength and rolling shear strength of crossing areas determined by tests with small specimens, expressed in N/mm^2. 47

Table 2: tested CLT elements 53

Table 3: results of the destructive tests: maximum load achieved during the tests.... 61

Table 4: calculated pure shear stress, strain and shear modulus (**Dujic, Klobcar, and Zarnic 2007**) and calculated shear stress in the layers (**Andreolli, Rigamonti, and Tomasi 2014**). 69

Table 5: material properties of timber boards. 76

Table 6: cases considered for simulation for cohesive elements. 85

Table 7: cases considered for simulation for the friction surface. 91

Table 8: different meshing considered in the simulation. 92

Table 9: values of δ_{ratio} considered in the simulation for the cohesive element. 99

Table 10: length of the cohesive zone (l_{cz}) and equivalent mesh size (l_e) at varying of the parameter M. 101

Table 11: interface stiffness K proposed by different authors (N/mm^3). 102

Table 12: thickness values for each board. 122

Table 13: shear strength and wood percentage failure. 124

Table 14: summary of predicted and experimental values of shear strength expressed in N/mm^2. 126

Abstract

This research project will investigate the shear behaviour of Cross Laminated Timber (CLT) product through an in-plane shear test. More precisely it will aim to study the post-elastic behaviour and the damage evolution in the CLT panels. Load-displacement curves were experimentally determined, and the Cohesive Zone Model (CZM) was used to identify cohesive crack properties and to simulate failure of the twenty-four specimens tested in the laboratory. The modelling procedure will be undertaken in the finite element modelling software; these models were built upon the experimental data for the mechanical properties of Spruce timber. The known modulus of elasticity and the orientation of grain direction were used to perform a finite elements analysis, calculating stress and strain distributions and damage evolution under applied loading. The cohesive zone model can capture the nonlinear behaviours, which often occurs in the fracture process zone ahead of the crack tip.

In the used constitutive model, one idealises timber as a quasi-brittle material. Thus, one considers the material as a continuum with discontinuities (adhesive layer). The continuous part is characterised by elastic orthotropic stress-strain law while traction-separation law describes the behaviour of the discontinuities. Cohesive Zone Model is used to represent the fracture in the cohesive layers. Before cracking, the "composite" material obeys the rules of orthotropic elasticity. The data gathered from these models will then be used to draw comparisons with the experimental results and to help assess with further research whether the development of an innovative system based on this wooden product, in the rehabilitation field, is viable (i.e. seismic strengthening of the existing reinforced concrete frame buildings).

Sommario

Nel seguente lavoro di tesi si analizza il comportamento a taglio di pannelli in legno a strati incrociati (Cross Laminated Timber - CLT), con principale attenzione al comportamento post-elastico del materiale, alla duttilità e alla sua capacità dissipativa. Test sperimentali sono stati condotti in laboratorio sottoponendo i pannelli a carico di taglio nel piano. I dati sperimentali ottenuti sono stati utilizzati per implementare un modello agli elementi finiti basato su elementi coesivi (Cohesive Zone Model - CZM), atto a riprodurre ed identificare le proprietà del CLT tenendo in considerazione le proprietà meccaniche e l'orientamento delle fibre dei singoli strati in legno. In particolare, si è considerato il materiale legno come elemento continuo ed ortotropo in contatto con elementi di interfaccia utilizzati per simulare l'incollaggio esistente tra i layer in legno che costituiscono il pannello.

Dalla comparazione dei risultati numerici con i risultati sperimentali si osserva che le capacità resistenti del pannello sono stimate con buona approssimazione e gli elementi di interfaccia replicano fedelmente l'interazione che si sviluppa nelle zone di contatto tra gli strati incrociati del pannello.

Il modello così realizzato risulta in grado di descrivere il comportamento non lineare del materiale e l'evoluzione del suo danneggiamento, entrambi aspetti particolarmente rilevanti nelle valutazioni di carattere sismico di edifici di nuova costruzione o esistenti.

Ulteriori analisi saranno rivolte all'approfondimento della conoscenza delle capacità ultime del materiale, dando particolare rilevanza alle proprietà degli incollaggi utilizzati nella composizione del pannello e alla loro influenza sulle capacità meccaniche degli strati lignei. Inoltre, ulteriori modelli numerici potrebbero essere sviluppati al fine di ottenere una migliore comparazione con i dati sperimentali.

Acknowledgments

I would like to thank and acknowledge the Trees and Timber Institute of the National Research Council of Italy, CNR-IVALSA, (San Michele all'Adige, Italy) for provided experimental data of timber and adhesive products that have been used within this thesis.

Also, I would like to acknowledge Centro Legno s.r.l. for their support and help in supplying of Cross-Laminated Timber panels, which have been tested in the research programme.

Chapter 1
Introduction

The aim of this research project is to investigate the structural performance of Cross-Laminated Timber (CLT) panels to use as sharing the load in the wall system and develop a new purpose for the CLT, if possible, in the structural rehabilitation field. This investigation will study both the strength limit property of the CLT as well as deformation performance.
What makes this material so interesting is a helpful combination of lightweight and high resistance in-plane and out-of-plane loading. This combination allows its use both as wall and floor elements. At present, many advantages make growing the application of this product in the construction field, in first its high performance in seismic events and fire resistance, its fast on-site installation, is an environmentally friendly and easily recyclable material. In particular, the advantages to transferring the load in the two transversal directions together with the low weight of the CLT panel were the most important reason to consider this product particularly suitable for strengthening of existing buildings as well as for resisting in a seismic event.
In this work, one investigates the shear behaviour in Cross-Laminated Timber panels, under in-plane loading. In particular, the shear failure of the CLT panels, commonly used as structural wall elements, was analysed. For CLT under in-plane loading, some properties were still in discussion, and codes and standards did not still give exhaustive guidelines about this product.

1.1 Motivation

Over recent decades the wood constructions in the field of seismic design have taken more space. Throughout Europe, timber buildings with various constructive systems are becoming a stronger and valid alternative than concrete and masonry buildings. This is one reason why the international scientific community has set itself a lot of questions about the response to the earthquake of the wooden buildings. Closer examination of the literature thus notes that the focus on the seismic behaviour of the wooden buildings and in particular of the CLT construction technology, are the steel connections, and numerous work are focused in this context. The main problems derive from the handling, difficulty in assembling, inadequate connection systems, the complexity in verifying the

connectors and in defining the actual load path within/between the panels (Jorissen and Fragiacomo 2011; Rinaldin, Amadio, and Fragiacomo 2013; Polastri et al. 2016; Bradner 2016). The mentioned above problems are not the only interesting aspects that the researchers have studied in the last years. For its particular configuration, the Cross-Laminated panels become an attractive subject for the analysis of the damage mechanisms. The purpose is to obtain a comprehensive understanding of the behaviour in the post-elastic field, the causes of the damage with the aim to develop new application strategies (Dourado et al. 2008; Ardalany, Deam, and Fragiacomo 2012; Ardalany, Fragiacomo, and Moss 2015; E. Saavedra Flores et al. 2016). The latest type of investigation is the focus of this research, aimed to investigate the capacity of the CLT panel when its peak load is reached, and the non-linear and softening behaviour take place. The motivation of this work is primarily the study of the CLT material, not considering the contribution due to the connection system.

1.2 Research objectives

This research project will investigate the shear behaviour of CLT product through in-plane shear tests. More precisely it will aim to study the post-elastic behaviour and the damage evolution in the CLT panels. The final goal of the whole research is to move the first step in developing a new field of application for the CLT.
The following are the objectives which have been outlined as critical components to the research.

- Conduct a review of the current literature on CLT panels to understanding and appreciation of the current technologies associated with CLT.
- Acquire and test the specimens provided by CentroLegno s.r.l. to develop the experimental campaign.
- Create Finite Element Model (FEM) to explore the non-linear response of the CLT panel.
- Using both experimental and theoretical results to validate the model to explain the non-linear behaviour of CLT.

Chapter 2
Properties of wood

Wood is a complex biological structure composed of many cell type that together ensure conduction of water, mechanical support of the plant body and storage of biochemicals. The first differences among wood species are established by the type, size, proportion and arrangement of different cells. These essential structure details can affect the properties and the use of wood; it is worth remember that the variability in performance of timber is one of its inherent deficiencies as a material.

Commercial timber is obtained from two categories, hardwood and softwood. The main difference between these two group consists of their component cells. In particular, the structure of hardwood is more complex than softwood type.

In the softwoods about 90% of the cells are aligned in the vertical axis, whereas in hardwoods there is a much wider range in the percentage of cells that are vertical (80-90%). The remaining percentage is present in bands, known as *rays*, aligned in one of the two horizontal planes referred to as the radial plane or quartersaw plane. This means that there is a different distribution of cells on the three principal axes and this is one of the main reasons for the high degree of anisotropy present in timber. In the softwood, two types of cells can be observed. Those present in greater number are known as *tracheids*, some from 2 to 4mm in length with an aspect ratio (L/D) of about 100:1. These cells, which lie vertically in the tree trunk, are responsible for both the supporting and the conducting roles. The small block-like cells, known as *parenchyma*, are mostly located in the rays and are responsible for the storage of food material. In contrast, in the hardwoods four types of cell are present albeit that one, the *tracheid*, is present in small amounts. The role of storage is again primarily taken by the *parenchyma*, which can be present horizontally in the form of a ray, or vertically, either scattered or in distinct zones. Support is effected by long thin cells with very tapered ends, known as *fibres*. Conduction is carried out in cells known as *vessels or pores,* are usually short (from 0.2 to 1.2mm) and relatively wide (up to 0.5mm) and when situated above one another form an efficient conducting tube. It can see, therefore, that whereas in the softwood the three functions are performed by two types of cell, in the hardwoods each function is performed by a single cell type. Although all cell types develop a secondary wall, this varies in thickness, being related to the role that the cell will perform. Thus, in hardwood, the wall thickness

of fibres is several times that of the vessel. Consequently, the density of the wood, and hence many of the strength properties, are related to the relative proportions of the various types of cell. The range in density of timber is from 120 to 1200 kg/m^3, corresponding to pore volumes of from 92% to 18%. In addition to determining many of the technical properties of wood, the distribution of cell types and their sizes is used as a means of timber identification (Dinwoodie 1981). This subchapter is concerned with the most relevant mechanical properties of wood with the aim to defined the behaviour of the timber in terms of its performance. In the subsequent paragraphs, one describes the elastic orthotropic properties, as Modulus of Elasticity (MoE), the Poisson's ratio, the shear modulus, the non-elastic properties, as a stress-strain curve and strength properties. Mention will be made at the end of this section about the natural defects affecting the mechanical properties of wood.

2.1 Elastic orthotropic properties

Wood is a complex fibre composite which must be considered as an orthotropic material with three main directions: *longitudinal* (parallel to fibre), *radial* (normal to the growth in the radial direction), and *tangential* (perpendicular to grain and tangent to the growth rings), see ***Figure 2.1***. Each one of the orthotropic directions has mechanical properties that are different from the other, and also in each direction the behaviour is different in tension and compression (Kretschmann 2010). Particularly in compression perpendicular to the grain, timber shows ductile behaviour with the appearance of the densification phenomenon.

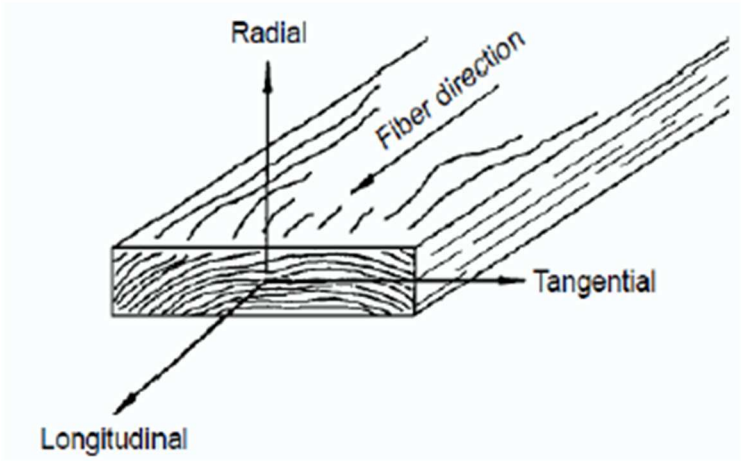

Figure 2.1: *three perpendicular axes: L (longitudinal), R (radial), T (tangential) on grain orientations* ***(Kretschmann 2010)***.

The MoE in the longitudinal direction is one of the principal elastic constants of the material. Elastic moduli values depend on species, growth condition, moisture

content or temperature, but with a good approximation they can generally be related according to the following ratio from (Bodig and Jayne 1993):

$$E_L : E_R : E_T \approx 20 : 1.6 : 1$$
$$G_{LR} : G_{LT} : G_{RT} \approx 10 : 9.4 : 1$$
$$E_L : G_{LR} \approx 14 : 1$$

The three MoE (E_L, E_R, E_T) are usually obtained from test methods, however, the data for E_R and E_T are not extensive.
A whole spectrum of test procedures exists for the determination of the elastic modulus. These methods can be conveniently subdivided into two groups, the first comprising static methods based on the application of a direct stress and the measurement of the resultant strain, while the second group comprising dynamic methods based on resonant vibration from flexural, torsional or ultrasonic pulse excitation. The determination of the elastic modulus from stress-strain curves has already been described, and it remains one of the more common methods. Although frequently carried out in the bending mode, it can also be derived from compression or tension tests. The value of the modulus in tensile, compressive and bending modes is approximately equal. The determination of the dynamic elastic modulus, E_d, can be obtained by either longitudinal or flexural vibration. The latter is used more frequently and may take the form of a small unloaded beam to which are attached thin metal plates. The beam vibrates under the action of an oscillating electromagnetic impulse. The response is measured as a function of the frequency, and the dynamic elastic modulus is calculated from the specimen dimensions and resonant frequency. The values of modulus obtained dynamically (E_d) are generally only marginally greater than those obtained by static methods (E_s). Although the mean value of E_d is only about 3% higher than that for E_s, the differences between the readings are nevertheless significant at the 0.1% level.
Within the elastic range of the material, the *shear modulus* (namely also modulus of rigidity) relates the shear stress to shear strain and denoted by the letter *G*. The three shear moduli (G_{LR}, G_{LT}, G_{RT}) are the elastic constants in the respective planes. Thus, G_{LR} is the shear modulus based on the shear strain on the LR plane and shear stress in the same plane. The shear moduli vary within the species and with moisture content and specific gravity (Kretschmann 2010). For structural size test pieces, the modulus of rigidity can be derived by one of two test procedures as described in (*EN 408:2010 Timber Structures - Structural Timber and Glued Laminated Timber - Determination of Some Physical and Mechanical Properties, CEN* 2010). In the first technique, the modulus is calculated from the difference in elastic modulus when derived by both four-point and three-point bending on the same test piece. In the second technique, the same test piece is loaded in three-point bending under at least four different spans.
In general, when a body is subjected to stress in one direction, the body will undergo a change in dimensions at right angles to the direction of stressing. Poisson's ratio represents the ratio of the contraction or extension to the applied

strain. In timber, because of its anisotropic behaviour, six Poisson's ratios occur (ν_{LR}, ν_{LT}, ν_{RT}, ν_{RL}, ν_{TL}, ν_{TR}). The first letter in the subscript refers to the direction of applied load, while the second one to the direction of lateral deformation. Also, the Poisson's ratios vary within the individual timber specimens of the same species depending on the moisture content of the wood and specific gravity.

2.2 Non-elastic properties

When a wood sample is loaded in tension, compression or bending, the instantaneous deformations obtained with increasing load are approximately proportional to the values of the applied load. It has become convenient to recognise a point of inflection on the load-deflection curve known as the *limit of proportionality*, below which the relationship between load and deformation is linear, and above which non-linearity occurs. Generally, the limit of proportionality in longitudinal tension is found to occur at about 60% of the ultimate load to failure, whereas in longitudinal compression the limit is considerably lower, varying from 30% to 50% of the failure value. Above this limit, wood behaves in a highly nonlinear way, and as the elastic properties, also non-elastic properties are influenced by density, moisture content, temperature and duration of loading. Holmberg in (Holmberg, Persson, and Petersson 1999) shown typical stress-strain curves for dry wood loaded in longitudinal (L), radial (R), and tangential (T) direction in compression and tension, as reported in ***Figure 2.2***.

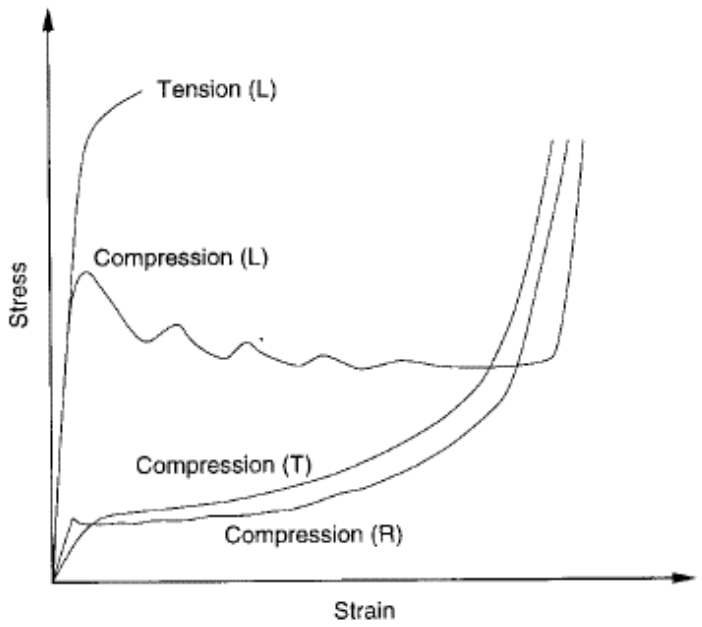

Figure 2.2*: typical stress-strain curves for wood loaded in compression in L, R and T directions and for tension in the L direction. (**Holmberg et al. 1998**).*

When the wood is loaded in compression, the response for the three main directions can be characterised by an initial elastic region, followed by a plateau region and finally a region of rapidly increasing stress. Compression in the tangential direction gives a smooth stress-strain curve which rises throughout the plateau, whereas compression in the radial direction tends to give a slightly irregular stress plateau and to be characterised by a small drop in stress after the linear elastic region has been passed. The tangential and radial yield stresses are about equal, while the yield stress in the longitudinal directions is considerably higher than that in the radial and tangential direction is serrated.

2.2.1 Failure types of wood

Three basic failure patterns can be distinguished from compression perpendicular to grain according to growth rings orientation and direction of load: the crushing of earlywood, buckling of growth rings and shear failure (Gibson and Ashby 1988), ***Figure 2.3.*** For radial compression, crushing failure in the earlywood zone occurs. Tangential compression results in a buckling of the growth rings, whereas shear failure often occurs for loading at an angle to the growth rings.

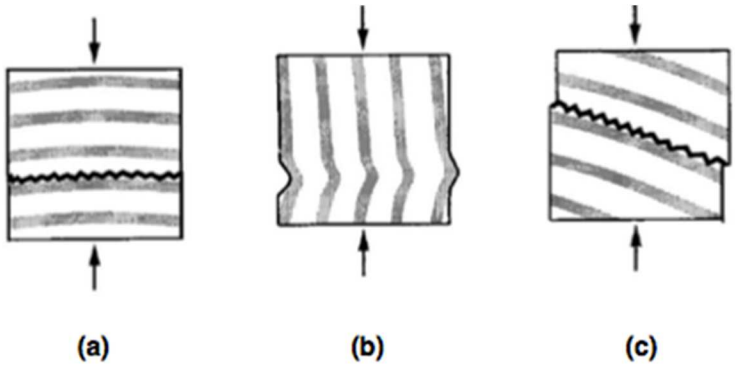

Figure 2.3*: failure types in compression perpendicular to the grain: the crushing of earlywood under radial loading (a); buckling of growth rings under tangential loading (b); shear failure under loading at an angle to the growth rings (c).* ***(Gibson and Ashby, 1988)***.

Failure modes that occur during a compression test in the longitudinal direction are the crushing in the approximately horizontal plane, wedge split, shearing rupture, splitting (usually occurs in specimens having internal defects), compression and shearing parallel to the grain.
Tensile loading perpendicular to the grain gives three failure patterns, similar to compression perpendicular to the grain: a tensile fracture in earlywood (radial loading), failure in wood rays (tangential loading) and shear failure along growth ring. In the case of tension parallel to grain, four type of failure may occur, namely shear, a combination of shear and tension, pure tension and splinter mode (***Figure 2.4***) (Feio 2005).

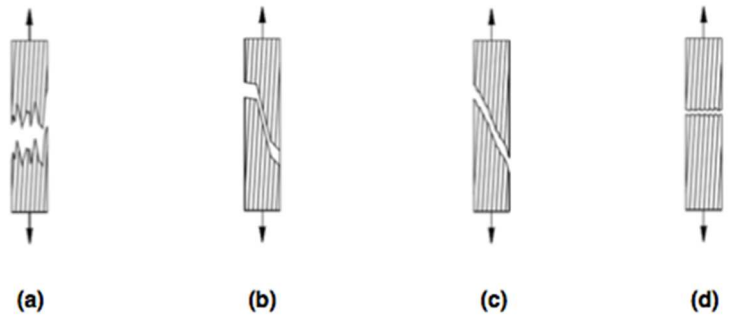

Figure 2.4: *failure types in tension parallel to the grain: splinter (a); shear and tension failure (b), shear failure (c) and pure tension failure (d). (**Feio, 2005**).*

2.3 Natural characteristics affecting mechanical properties of wood

Wood vary in its mechanical properties due to the natural characteristics or defects. Clear straight-grained wood is used for determining fundamental mechanical properties, however, because of natural growth characteristics of trees, wood products vary in specific gravity, may contain cross grain, or may have knots and localised slope of grain. Natural defects such as pitch pockets may occur as a result of biological or climatic elements influencing the living tree. These wood characteristics must be taken into account in assessing actual properties or estimating the actual performance of timber products.

2.3.1 Reaction wood

One of the most critical defects is the formation of *reaction wood*, usually as a consequence of wind action, resulting in the formation of an abnormal type of tissue. In softwood, the abnormal tissue is known as "*compression wood*", it is common to all softwood species and is found on the lower side of the limb or inclined tree trunk. In hardwoods, the abnormal tissue is known as "*tension wood*", it is located on the upper side of the inclined member, although in some instances it is distributed irregularly around the cross section. Reaction wood is more prevalent in some species than in others, which are considerably more brittle than normal wood and resulting in difficulties in sawing and machining.

2.3.2 Knots

One other defect of considerable technical significance are the knots. A knot is that portion of a branch that has become incorporated in the bole of a tree. The influence of a knot on the mechanical properties of a wood member is due to the interruption of continuity and change in the direction of wood fibres. The influence of knots depends on their size, location, shape, and soundness, the

attendant local slope of grain, and type of stress to which the wood member is subjected. Most mechanical properties are lower in sections containing knots than in clear straight-grained wood because the clear wood is displaced by knot, the fibres around the knot are distorted, resulting in cross grain, the discontinuity of wood fibre leads to stress concentrations, and checking often occurs around the knot during drying. Hardness and strength in compression perpendicular to the grain are exceptions, where knots may be objectionable only in that they cause no uniform wear or non-uniform stress distributions at the contact surface. It is not surprising that the presence of knots in timber results also in a reduction of the stiffness. It is hard to quantify the relationship, since the effects of knots will depend on their number and size, on their distribution both along the length and across the faces of the sample.

2.3.3 Specific gravity

The substance of which wood is composed is heavier than water; its specific gravity is about 1.5 regardless of wood species. Despite this, dry wood of most species floats in water, and it is thus evident that cell cavities and pores occupy part of the volume of a piece of timber. Variations in the size of these openings and the thickness of the cell walls cause some species to have more wood substance per unit volume than other species and therefore higher specific gravity. Thus, specific gravity is an excellent index of the amount of wood substance contained in a piece of wood; it is a useful index of mechanical properties as long as the wood is clear, straight grained, and free from defects. However, specific gravity values also reflect the presence of gums, resins, and extractives, which contribute to mechanical properties.

2.3.4 Annual ring orientation

Stresses perpendicular to the grain direction may be at any angle from 0° (*T direction*) to 90° (*R direction*) to the growth rings, ***Figure 2.5***. Perpendicular-to-grain properties depend on somewhat upon the orientation of annual rings with respect to the direction of stress.

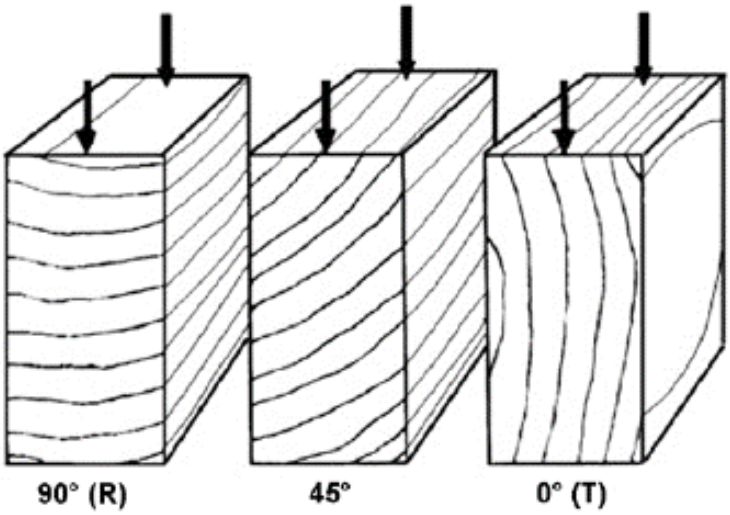

Figure 2.5: *the direction of load in relation to the direction of annual growth rings: 90° or perpendicular (R), 45°, 0° or parallel (T).* ***(Kretschmann 2010)***.

In some species, there is no difference in 0° and 90° orientation properties. Other species exhibit slightly higher shear parallel or tension perpendicular-to-grain properties for the 0° orientation than for 90° orientation, the converse is true for about an equal number of species.
The effects of intermediate annual ring orientations have been studied in a limit way. Modulus of elasticity, compressive perpendicular-to-grain stress at the proportional limit, and tensile strength perpendicular to the grain tend to be about the same at 45° and 0°, but for some species, these values are 40% to 60% lower at the 45° orientation. For those species with lower properties at 45° ring orientation, properties tend to be about equal at 0° and 90° orientations. For species with about equal properties at 0° and 45° orientations, properties tend to be higher at the 90° directions.

2.3.5 Pitch pockets

A pitch pocket is a well-defined opening that contains free resin. The pocket extended parallel to the annual rings, it almost flat on the pitching side and curved on the bark side. Pitch pockets are confined to such species as the pines, spruces, Douglas, tamarack, and western larch. The effect of pitch pockets on strength depends on upon their number, size, and location in the piece. A large number of pitch pockets indicates a lack of bond between annual growth layers, and a piece with pitch pockets should be inspected for shake or separation along the grain.

2.3.6 Temperature and moisture content

The very marked reduction in strength and serviceability are due to splits and crack. Timber in an unstressed state may undergo dimensional changes following variations in its moisture content and/or temperature. At moisture contents above 20% many timbers, especially their sapwood, are susceptible to attack by fungi besides the fact that the strength and stiffness of green wood are considerably lower than for the same timber when dry. There are two categories of the natural origin of splits and crack in timber: resource based and changing in moisture content based. Resource-based splits and cracks occur in a standing tree or a log as a result of environmental conditions, growth stresses or acting of microorganism. Ring shake which appears as longitudinal separation of wood fibres in the tangential direction can be ranged in this group. Cracks related to dimensional changes can be associated with a drier environment than the timber moisture contents, or with a wetter environment than the timber due to a seasonal or daily variations in the relative humidity of the surrounding atmosphere (Dinwoodie 1981). The former changes are called "*shrinkage*", whereas the latter is known as a "*movement*". The fundamental relationships between moisture content of timber and atmospheric conditions have been determined experimentally, the influence of moisture content on stiffness is similar as that for strength. Early experiments by (Carrington 1922), in which stiffness was measured on a specimen of Sitka spruce as it took up moisture from the dry state, clearly indicated a linear loss in stiffness as the moisture content increased to about 30%. Carrington also measured the rigidity moduli and Poisson's ratios. Although the former showed a similar trend to the elastic moduli, only one of the latter displayed the same trend, whereas the three other Poisson's ratios that were measured showed an inverted relationship.

2.4 Cross-laminated Timber Technology

As is stated by (Moody and Hernandez 1997) the glue laminated timber is the oldest engineered wood product in the world. It is commonly used in Europe, Japan and North America in a variety of application, ranging from wall panels and floor structures in residential buildings to major load bearing beams, trusses and pillars in multi-storey building developments.
As a result, European nations have started conducting extensive research on the optimisation of Cross-Laminated Timber design, investigating layer properties, resin type, wood species and layer orientations. The research and development of CLT products initially started in Switzerland in the early 1970's, and Europe became the world leader in CLT innovation and technologies. On the other hand, Australia has only recently discovered the potential of optimising its own CLT design, since it has been noted that these wood-based panels possess significant increases in structural performance over standard timber beams. These benefits include:

- *An increased fire resistance* – building with CLT components can increase a fire resistance by creating large solid sections, which the fire must travel through before the structure is significantly weakened. Also due to the very limited cavity space available to hold oxygen in the panel, combustion is inhibited.
- *Sound Proofing* – due to the solid nature of wood products, wood possesses natural sound absorbing mechanics. Solid CLT panels used in walls and floor plates are superior to standard construction practices at absorbing sound waves, as they do no possess hollow midsection cavities.
- *Thermal Insulation* – CLT wall components offer significant improvements to thermal insulation, providing an improved barrier between "inside" and "outside" energy transfer rates.

The investigation into the increase of strength due to lamination was conducted by (Falk, R. and Colling 1995). This research reached the conclusion that the lamination of timber reinforces the defects of the individual timber layers by redistributing the applied stress acting on the defective area to the relatively defect free wood of adjacent layers. (Falk, R. and Colling 1995) also concluded that the increase of strength could be attributed to the summation of separate, physical characteristics, depending on the lamination process used to bond the CLT component and the related testing procedures. However, CLT components fall into the category of composite materials. Based on composite material theories, the shear capacity of any cross-sectional area is reduced as the panel (or beam) size increases; this has been proven to be accurate in studies carried out by (Soltis and Rammer 1993).

The material properties of CLT are dependent upon the properties of the individual timbers used in the layered structures. Since one considers the CLT component as a composite material, it can then be thought of having to distinct components: the reinforcing fibres (timber grains) and a binding matrix (adhesive). The mechanical properties of timber are hard to calculate at the location of a major defect. In order to create a homogeneous material (out of) from the heterogeneous material, the larger defects in the timber are removed, and the remaining minor defects are distributed evenly throughout the volume of CLT. This homogenisation leaves the CLT panel with an overall combined strength, with no one point being any weaker than any other.

The stiffness properties of the panel can be accurately calculated by analysing the individual layer properties (Bodig and Jayne 1993), or by testing section cut from the panel using the current relevant standards, (*EN 13353:2008 Solid Wood Panels (SWP). Requirements, CEN* 2008), (*EN 13986+A1:2015 Wood-Based Panels for Use in Construction - Characteristics, Evaluation of Conformity and Marking, CEN* 2015), (*EN 789:2005 Determination of Mechanical Properties of Wood-Based Panels, CEN* 2005). The selection of an appropriate bonding resin is another important process in the optimisation of the CLT element. Due to the negligible thickness of the bonding resin layer, the surface area in contact with the timber

element becomes the critical factor. Due to the same reason, the axial compressive strength of the resin is not the major contributing factor; the timber will carry compression loads. Instead, the shear resistance of the resin and the axial strain due to deformation as a result of applied loading will factor more predominately.
The resin selected needs to fall into the category of a "*Prime structural adhesive*" as the resin will contribute to the strength and stiffness of the wood structure for the entire lifetime duration. The only significance of the resin properties is its ability to provide a strong, durable and reliable bond between the adjacent timber layers. The critical component in the selection of an appropriate resin is that the bond layer of the resin must not fail before the surrounding timber element. The deformation due to deflection under applied loading will not only create stress throughout the timber layers but also through the layers of bonding resin. Thus, a crucial requirement of the adhesive that can "flex" with the low timber modulus or possesses an allowable strain limit exceeds that of the wood. (Faherty and Williamson 1999) state that the use of joining timber members together through the use of an adhesive is the most efficient way to apply load transfers of shear forces between adjacent timber layers. In the same study, the authors state one of the most important reasons for using an adhesive is it allows the composite wood component to utilise different grades of timber, minimise the effects of defects on strength and stiffness and provide an avenue for efficient timber usage.
Two resin types are predominantly used in current industry construction; these are "*Melamine urea formaldehyde resins*" and "*Polyurethane resins*" (PUR). Many companies list the PUR adhesives as their preferred bonding agent, making this the most widely used resin.

2.4.1 Investigations on CLT: State of Art

This subchapter contains a brief summary of previous research that has carried out on the construction and optimisation of Cross-Laminated Timber products.
The majority of overseas research has been directed at using CLT components as a load bearing plates and shear wall panels. The composition of the CLT panels consists of 3, 5 or 7 layers of timber, with different thickness and (sometimes) grade, bonded together with an adhesive and alternated layers having perpendicular grain direction. Since the CLT element and its capacities depend on the manufacturer, there are many manufacturers as well as different CLT products. This is a direct consequence of the current lack of codes and regulations for the production and use of CLT elements in the framework of the European standards. The situation was similar in North America until December 2011, when a new standard for CLT was finally approved for publication by the American National Standards Institute (*ANSI/APA PRG 320-2012 Standard for Performance-Rated Cross-Laminated Timber. The Engineered Wood Association* 2012). Nevertheless, further guidelines and reliable testing methods are still needed for a rapid

evaluation of the complex mechanical performance of CLT. However, some of the main recognised manufacturers of CLT are mainly in the European area, such as KLH, Stora Enso and Holz100. Currently, the mechanical properties of CLT are specified in European Technical Assessment (ETA), which entered into force on 1st of July 2013 in all European Members States and the European Economic Area. The ETA is an alternative for construction products not covered by a harmonised standard. It is a document providing information on their performance assessment. The procedure is established in the Construction Products Regulation and offers a way for manufacturers to draw up the Declaration of Performance and affix the CE marking.

Concerning the CLT technology, several studies have been conducted both experimental and analytical methods. Concerning the mechanical behaviour, the research is focused on the static compression, flexural behaviour and the dynamic behaviour of such components.

Many research projects are developed in this direction. The authors in (Czaderski et al. 2007) examined the CLT panel subjected to different types of load and had made a comparison of results obtained by different theories and Finite Element Methods (FEM). In this way, they found a high variability of the output data that depends on the method used. It is worth nothing that the main parameters that influence the results were the geometric properties of the CLT panel (i. e., panel size) and properties of the material. (Gulzow, Gsell, and Steiger 2008) and (Steiger, Gulzow, and Gsell 2008) performed an experimental campaign and modal analysis of CLT panel in order to obtain homogenised stiffness parameters. This procedure allowed the determination of the five elastic parameters from a single test. (Stürzenbecher, Hofstetter, and Eberhardsteiner 2010) are instead developing the application of different theories on the behaviour of the CLT plate. The authors are focused on the accuracy of the theories about the behaviour both in terms of in-plane displacement and out-of-plane bending of the panel. They concluded that the accuracy of the theories applied on CLT panel depends on the thickness of the boards as much as the load conditions. Consequently, none of those theories may be applied to the CLT panel as a general rule; in any case, it must take into account the specific application of the panel. The FEM analysis of Cross-Laminates was presented by (Gereke and Niemz 2010), who studied the stresses induced by a moisture gradient within the boards. The authors concluded that the intensity and the direction of the developed stress depend on the growth rings angle within the boards. This effect could be reduced, to some extent, by a pre-stress compression. The FEM simulations in the analysis of composite and based-timber materials were used for more than 30 years because they can deal with the inherent complexity of its internal structure. A complete review was compiled by (Mackerle 2005), who summarised more than 260 research papers that used a FEM, from 1995 to 2004. As in the case of numerical methods, the reliability of FEM simulations must be verified through a comparison with experimental data that include the characteristics of the material.

A limitation of standard test methods is that the deformation of inherently non-homogeneous specimens is based on the physical measurement made in only a

few points, even if carefully selected. This limitation inspired the study done by (Sebera et al. 2015) which used the optical full-field techniques based on the principle of the Digital Image Correlation (DIC), able to measure without contact the displacement, the deformations, and the vibrations in materials subjected to applied forces. This accurate method, immediately compatible with data of numerical analysis, is a very convenient tool for the verification of FEM simulations (Muszynski and Launey 2010; Sharpe 2008; Sutton 2008). For these reasons, as pointed out by the authors, the DIC technique has become widely used in the wood study, due to the high complexity and variability of the material.

To date, some of these results are incorporated into a software package owned by Forschungs-Holzbau GmbH (Peter Mestek, Heinrich, and Winter 2008; Thiel and Schickhofer 2010), a packet to professional practice is addressed.

The restoration field was another important area in which the CLT panels were widely used. As reported by (Gubana 2009) about the research developed at the University of Udine, the intent to adopt the reversible technologies in the restoration of historic buildings suggests the possible use of the Cross-Laminated panels as floor slabs connected to the existing wooden beams, instead of the cooperating reinforced concrete slab. In the experimental program, the in-plane shear tests are developed that highlight interesting values of strength and elastic modulus. Moreover, their use in historic buildings, with wooden beam floors, implies a smaller seismic action due to the lower weight of CLT panels than the concrete slab.

One of the most important studies about the CLT as the structural system was developed by CNR-IVALSA (*Trees and Timber Institute of the National Research Council of Italy, San Michele all'Adige, Italy*). The research project, named SOFIE (Construction System Fiemme – IVALSA - CNR, 2008) (A. Ceccotti 2010; A Ceccotti, Sandhass, and Yasumura 2011), investigates all aspect of a full-size building (mechanical properties of the CLT, acoustics and seismic performance, fire resistance, thermal behaviour, and durability). The most important tests of the SOFIE project on a shaking table (Ario Ceccotti, Follesa, and Lauriola 2007) in Japan, were performed involving two multi-storey buildings made of Cross-Laminated wooden panels. The CLT construction system seems to have an excellent seismic behaviour and all dissipation and ductility are depending on the connection design.

From a summary of published works in this context, the complexity of the mechanical properties mainly due to the anisotropic behaviour of the material was evident. Moreover, should be considered the dominant role of the interaction between the layers of the panel and the connections system. Indeed, in the CLT construction system the behaviour of the wall, for low magnitudes of shear force, is mainly due to the connection elements, (i.e. steel angular bracket and holdowns) and not due to the performance of wooden panels.

In the research performed by (Rinaldin, Amadio, and Fragiacomo 2013) a numerical model to estimate the energy dissipation capacity is developed. Herein the cyclic response of buildings made of CLT panels shows the consequences of neglecting the stiffness of the connections between the elements, the same

results are showed in the works of (Iztok Sustersic, Fragiacomo, and Dujic 2012) and (Fragiacomo, Dujic, and Sustersic 2011).

The FEM presented by (I Sustersic and Dujic 2012) used a substitute diagonal (trusses) to simplified a possible CLT wall assembly. Starting from a FEM with shell elements and springs, the authors operate two-steps of simplifications. The first one considers the diagonal trusses instead of shell elements for each of the two walls, while the springs are joined at discrete points in the corners of the each truss. The second step is the full simplified FEM, where the vertical connections among the two CLT wall are joined in the substitution diagonal. Therefore, it must be stressed, that a truss simplification is particularly suitable for the linear elastic behavior while it is a too simplified method for the post-elastic behavior.

About the shear capacity of CLT panels, it is relevant the study carried out by (Dujic, Klobcar, and Zarnic 2007). The main goals of the research are to provide information to estimate the strength and the stiffness of CLT walls with openings and to identify how the shape and the area of the openings influence the shear strength and stiffness. The study concludes that the openings with a total area greater than 30% of the entire surface of the wall do not significantly affect the load capacity of the wall. However, the stiffness of about 50% was reduced.

More recent studies carried out at the University of Ljubljana by Sustersic and Dujic deal with the possible use of Cross-Laminated panels for the reinforcement of existing buildings subjected to the seismic actions (I. Sustersic and Dujic 2014; I Sustersic and Dujic 2014). The authors consider the masonry buildings, the reinforced concrete buildings and the reinforced concrete buildings with masonry infill. The tests on masonry walls show that the application of CLT panels involves an increase of about 40% in terms of resistance and of about 100% in terms of ductility. The experimental tests carried out on a shaking table at the IZIIS Institute of Skopje in two-storey buildings, with and without infill already damaged, highlight the ability of CLT panels to increase the stiffness of the structure and to bring it back to the not damaged state.

The analysis of the literature shows that the complex structure of the panels can be modelled using an orthotropic material, an orthotropic homogenised material or an isotropic material, depending on the possibilities offered by the software whereby the finite element analysis was carried out.

(Blass and Fellmoser 2004) proposed a Homogenised Orthotropic plane stress Blass reduced cross Section (HOBS) method, based on the transformation of the multi-layer behaviour in the single-layer behaviour through the use of the coefficients that affect the stiffness and strength values. Also, if a state of plane stress is assumed, it is enough to define two elastic moduli (E_0 and E_{90}), a shear modulus (G_{12}) and a Poisson's ratio. Despite its simplicity, this model provides accurate results for the seismic design. (Fragiacomo, Dujic, and Sustersic 2011) refer to this model, to create a four-storey building model made with CLT panels, on which perform nonlinear static analysis (Pushover). The influence of the connections in the modal response of the structure and its stiffness is stressed by the author to highlight the relevance of the accurate finite element modelling. Another important point stressed by the authors is that during an earthquake, the

energy is dissipated by means of all connections, and through the friction created between the wood panels. However, at present, this contribution to the dissipation is neglected, and further investigations should be developed.
A constitutive model for wood based on the hardening behaviour associated with large compression deformation with brittle fracture was developed by (Oudjene and Khelifa 2009). The model is implemented in ABAQUS code, and its validation is performed by means of uniaxial compression in the longitudinal and radial directions and through flexural tests.
The mechanical parameters of the material are determined using the experimental data (stress-strain curves) derived from the uniaxial compression tests. In the FEM, the isotropic behaviour in the transverse direction (radial and tangential) is assumed. The results show the ability of the model to simulate the behaviour of wood for large compressive deformation, and the plastic behaviour is clearly shown. The obtained results from the three-point bending test, show a good implementation of the brittle fracture criterion and demonstrate the suitability of the model to design and assess wooden structures.
Recently, an investigation about the determination of testing configurations and the related calculations of the strength and stiffness properties of CLT is performed by (Bauer and Schickhofer 2016). On the basis of numerous scientific works, the regulations in the existing standard (*EN 16351:2015 Timber, Timber Structure - Cross Laminated Timber - Requirements, CEN* 2015) and the given test setups for achieving an ETA, the authors propose test configurations which allow a stable determination of the material properties. The study discusses the test setups for bending, rolling shear and compression perpendicular to the grain for out-of-plane loads and in-plane shear.
With reference to the study of a constitutive model for timber product, it should be mentioned the investigation presented by (Oppel and Rautenstrauch 2016) which considers material discontinuities and the influences of a non-linear structural analysis of wooden shell system referring to the existing constitutive law of material.

2.4.2 European standardisation

So far, the technical standards allow for a reliable practice and provide the basis for certification, which is nowadays well established all over Europe, and for performance-based specifications.
Similar to CLT, glued laminated timber (glulam) is also constituted by several boards, but these are glued together parallel to each other. To date, glulam represents the most diffused solid-timber engineered material in the wood industry and has been widely employed in the buildings sector for several years. Therefore, it constitutes a reference product for the relatively new CLT panels. The evaluating of the bonding quality of glulam is carried out according to the standard ('EN 14080:2013 Timber Structures — Glued Laminated Timber and Glued Solid Timber — Requirements - British Standards Institute' 2013) that

provides both shear and delamination tests to verify the bonding strength and the glue line integrity of the product.

The situation for CLT panels is a little different. The standard (*EN 16351:2015 Timber, Timber Structure - Cross Laminated Timber - Requirements, CEN* 2015) concerning CLT products is recently published after a lengthy discussion, and only a few works are published so far with regards to the bonding quality evaluation of CLT panels (K. S. Sikora, McPolin, and Harte 2016; Vallée, Tannert, and Fecht 2015). Nevertheless, EN 16351 prescribes shear tests on both edge bonds and face bonds. In addition, it provides delamination tests for the evaluation of glue line integrity between layers. Also, this method is carried out according to procedures very similar to those described for glulam in EN 14080 (Method B in Annex C). However, the delamination test requirements are quite severe for CLT. For this reason, the same standard EN 16351 provides the splitting of the glue line where delamination limits are exceeded or in the case of poor surface quality, and the estimation of the wood failure percentage on the split surface.

In addition to technical standards concerning specifically glulam and CLT, a different methodology is provided by the European Standardisation Committee to assess the bonding quality od solid wood panels: (*EN 13353:2008 Solid Wood Panels (SWP). Requirements, CEN* 2008) aims at defining the requirements of solid wood panels both for non-structural and structural uses, whereas (*EN 13354:2008. Solid Wood Panels (SWP) – Bonding Quality – Test Method. CEN* 2008) describes the test procedure to evaluate the bonding quality of single layer and multilayer panels by means of a shear test. In this case, the specimens are F-shaped. Although this method is also specifically intended for structural multilayered wood panels with crossed grain (as in CLT), it is not considered in EN 16351.

Chapter 3
Fracture Mechanics and Damage Mechanics

The central difficulty in considering fracture in high-strength materials is that the presence of cracks can modify the local stresses. When a crack reaches a certain critical length, it can propagate catastrophically through the structure, even though the gross stress is much less than would normally cause yield or failure in a tensile specimen. The term "*fracture mechanics*" refers to a specialisation within solid mechanics in which the presence of a crack is assumed with the aim to find quantitative relations between the crack length, the material's inherent resistance to crack growth, and the stress at which the crack propagates. The fracture mechanics approach has three important variables: applied stress, flaw size, and fracture toughness while traditional approach to structural design has two main variables: applied stress and yield or tensile strength. In the latter case, a material is assumed to be adequate if its strength is greater than the expected applied stress. The additional structural variable in fracture mechanics approach is flaw size and fracture toughness. They replace strength as the relevant material property. Fracture mechanics quantifies the critical combinations of the three variables (Anderson 2005). In fracture mechanics, fracture toughness is essentially a measure of the extent of plastic deformation associated with the crack extension. Fracture toughness is measured by critical strain energy release rate according to energy-balance approach or by critical stress intensity factor (SIF) according to stress intensity approach (Dinwoodie 1981). The energy approach assumes that crack extension (i.e. fracture) occurs when the energy available for crack growth is sufficient to overcome the resistance of the material. The material resistance may include the surface energy, plastic work, or other types of energy dissipation associated with crack propagation. This approach is based on energy release rate that is defined as the rate of change in potential energy with the crack area for a linear elastic material. Stress intensity approach examines the stress state near the tip of a sharp crack and defines critical stress intensity factor that is a fracture toughness measured, and it can be used for normal opening crack modes I and shear sliding modes II and III (K_{IC}, K_{IIC}, K_{IIIC}).

When the plastic crack tip zone is too large, the stress and strain fields from Linear Elastic Fracture Mechanics (LEFM) are not valid anymore. This is also the case when the material behaviour is nonlinear elastic (e.g. in polymers and composites). Crack growth criteria can no longer be formulated with the stress intensity factor. For such cases, Non-Linear Fracture Mechanics (NLFM) or Elasto-Plastic Fracture Mechanics provides new theories and concepts to analyse the behaviour of cracks.
While the LEFM is a theory used for the analysis of brittle materials where all damage phenomena are assumed to be concentrated at the crack tip, the Damage Mechanics (DM) treats the problem of fracture in materials that exhibit softening behaviour (i.e. quasi-brittle materials) (Daudeville 1999). The damage of materials is the progressive physical process by which they break. The mechanics of damage is the study, through mechanical variables, of the mechanisms involved in this deterioration when the materials are subjected to loading.

3.1 Linear Elastic Fracture Mechanics

In case *Linear Elastic Fracture Mechanics* (LEFM) is involved, critical strain energy release rate is equal to fracture energy ($G_C = G_f$). Both variables are a material property that gives information about when a crack starts propagating (Bostrom 1992). In LEFM analysis, the deformations of the elements are limited to linear elastic behaviour and only the fracture interface (a surface) can fail. The surface between the adjoining materials constrains them together with zero ductility until it fails, at which point the failure surface dissipates a finite amount of energy (G_C) per unit growth of the crack.

3.1.1 Griffith's Work

This section provides a brief overview of the generalised Griffith energy criterion used to characterise crack propagation. This provides a foundation for a good understanding of the cohesive element approach.
Alan Arnold Griffith conceived the original concept of the fracture energy. The greatest contribution to the idea of the tensile strength of the materials was to realize that the weakening of the material, due to a fracture, could be treated as a problem of equilibrium in which the reduction of the deformation energy of the body containing fracture it could be compared to the increase in surface energy due to the growth of the same surface (Griffith 1920). The Griffith's equation describes the relationship between applied nominal stress (σ) and crack length at fracture (a), i.e. when it becomes energetically favourable for a crack to grow. The next step in the development of Griffith's argument was consideration of the rates of energy changes associated with the incremental crack extension. In Griffith's formulation the strain energy per unit volume (V) of stressed material is:

$$U^* = \frac{1}{V} \int f \, dx = \int \frac{f}{A} \frac{dx}{L} = \int \sigma \, d\epsilon \quad (1)$$

When a crack has grown into a solid to a depth *a*, a region of material adjacent to the free surfaces is unloaded, and its strain energy released.

3.1.2 Irwin's Work

Griffith's original work dealt with very brittle materials, specifically glass rods. When the material exhibits more ductility, consideration of the surface energy alone fails to provide an accurate model for fracture. This deficiency was later remedied, at least in part, independently by G.R. Irwin (Irwin 1948) and E. Orowan (Orowan 1949). They suggested that in a ductile material a good deal of the released strain energy was absorbed not by creating a new surface, but by energy dissipation due to the plastic flow in the material near the crack tip. They suggested that catastrophic fracture occurs when the strain energy is released at a rate sufficient to satisfy the needs of all these "sinks" of energy, and denoted this *critical strain energy release rate* by the parameter G_C; Griffith's equation can then be rewritten in the form:

$$\sigma_f = \sqrt{\frac{EG_c}{\pi a}} \quad (2)$$

This expression describes the connection between three important aspects of the fracture process: the material, as evidenced in the critical strain energy release rate G_C; the stress level σ_f; and the size, *a*, of the flaw. Irwin also demonstrated, through the Westergaard method, that the stress field in the area of the crack tip is completely determined by the crucial parameter *K*, known as the *stress intensity factor*. The factor *K* contains the dependence on applied stress σ, the crack length *a*, and the specimen geometry. The *K*-factor gives the overall intensity of the stress distribution, hence its name. The literature treats three types of cracks, termed mode I, II, and III as illustrated in ***Figure 3.1***, so the subscript is used to denote the crack opening mode (K_{IC}, K_{IIC}, K_{IIIC}). The literature contains expressions for *K* for a large number of crack and loading geometries, and both numerical and experimental procedures exist for determining the stress intensity factor is specific actual geometries.

Mode I

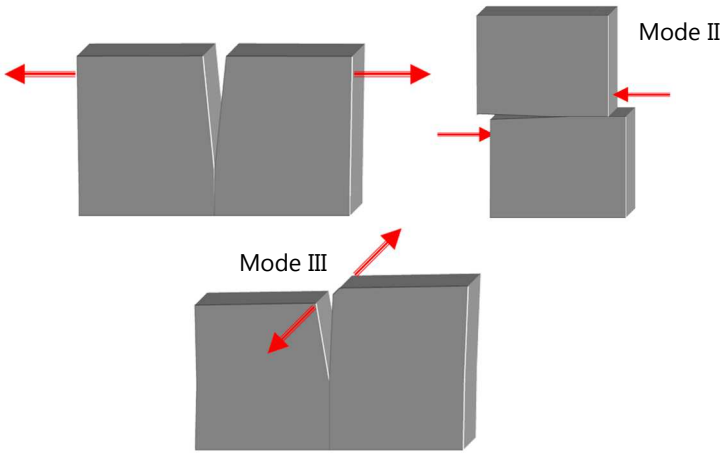

Figure 3.1: *fracture modes. Mode I is a normal opening mode, modes II and III are shear sliding modes* **(Broek 1986)**.

This critical stress intensity factor is then a measure of material toughness. The failure stress σ_f is then related to the crack length a and the fracture toughness (Mode I) by:

$$\sigma_f = \frac{K_{IC}}{\alpha\sqrt{\pi a}} \tag{3}$$

where α is a geometrical parameter equal to 1 for edge cracks and generally on the order of unity for other situations. Expressions for α are tabulated for a wide variety of specimen and crack geometries.

3.2 Nonlinear Fracture Mechanics

When the plastic crack tip zone is too large or when the material behaviour is intrinsically nonlinear, concepts from LEFM lose their meaning.
The *Elasto-Plastic Fracture Mechanics* (EPFM) or *Non-Linear Fracture Mechanics* (NLFM) criteria are derived, based on the *Crack Tip Opening Displacement (CTOD)*. In LEFM the CTOD can be related to the energy release rate G and the stress intensity factor K. In NLFM the CTOD is a measure for the deformation at the crack tip, which can be compared to a critical value in a crack growth criterion. The critical value, which may depend on strain rate and/or temperature, has to be measured. Its calculation is possible using models of Irwin or Dugdale-Barenblatt for the crack tip zone (Dugdale 1960; Barenblatt 1962).
Another crack growth parameter is the J-integral, which characterises the stress/deformation state in the crack tip zone. In LEFM, crack growth can be predicted by calculation of the energy release rate G or the stress intensity factor K. The behaviour of a crack can be described with the J-integral, which has been introduced by Rice in fracture mechanics in 1968 (Rice 1968).

The J-integral is a nonlinear elastic quantity, and it requires care in its application to elastic-plastic fracture toughness measurement and implementation. Extensive experimental and computational work has been devoted to demonstrating the applicability of the J-integral as a useful measure of fracture toughness. The value of the J-integral results from an integration along an arbitrary curve (Γ) around the tip of a crack. In each point of this trajectory, the specific elastic energy must be calculated from stresses and strains.

3.3 Continuum Damage Mechanics

Material damage is the gradual process of mechanical deterioration that ultimately results in component failure. The continuum damage mechanics is a constitutive theory that describes the progressive loss of material integrity due to the propagation and coalescence of micro-cracks, micro-voids, and similar defects. These changes in the microstructure lead to a degradation of material stiffness observed on the macro scale. The term "*continuum damage mechanics*" was first used by Hult in 1972 but the concept of damage had been introduced by Kachanov already in 1958 in the context of creep rupture (Kachanov 1958) and further developed in (Rabotnov 1968; Leckie and Hayhurst 1974; Hayhurst 1972). Mechanical damage occurs as soon as the material is exposed to external loading. Under relatively small loads, these defects may be too small to be detected by conventional means. Fracture, fatigue and creep rupture are all instances of substantial material damage typically associated with exposure to more extreme loading conditions.
Damage mechanics is the study of material damage based on the introduction of damage variables and their evolution under the applied loading conditions. Damage mechanics aims to quantitatively represent the accrual of mechanical deterioration of a material component subjected to certain loading. This is done by introducing a damage variable defined as follows. Consider a representative volume element (RVE) of material surrounding a point in the material and an area element dS through it. Let dS_D be the amount of area inside dS occupied by material discontinuities characterising damage such as cracks or voids of various types. The damage at the point is then determined by the numerical value of the damage variable D defined as:

$$D = \frac{dS_D}{dS} \tag{4}$$

Obviously, the damage variable D is a number $\in [0,1]$. The value D = 0 describes the undamaged material and D= 1 represents the ruptured component. Since discontinuities such as cracks and voids are unable to bear any load, the effective stress related to the surface resisting the load (i.e. $S - S_D$) resulting from an applied force F is:

$$\bar{\sigma} = \frac{F}{S-S_D} = \frac{F}{S(1-{}^{S_D}/_{S})} = \frac{\sigma}{1-D} \quad (5)$$

In fracture processes, the critical value of the damage variable associated with fracture crack initiation under applied stress σ is given approximately by:

$$D_C \approx 1 - \frac{\sigma}{\sigma_u} \quad (6)$$

where here the σ_u is the ultimate tensile strength of the material.
At the microscale level, this is the accumulation of micro stresses in the neighbourhood of defects or interfaces and the breaking of bonds, which both damage the material. At the mesoscale[1] level of the representative volume element, this is the growth and the coalescence of micro-cracks or micro-voids which together initiate one crack. At the macroscale level, this is the growth of that crack. Even if the damage at the microscale is governed by one general mechanism of debonding, at the mesoscale it can manifest itself in various ways depending upon the nature of the materials, the type of loading, and the temperature. The following description is limited to only two types, brittle damage and ductile damage. The damage is called brittle when a crack is initiated at the mesoscale without a significant amount of plastic strain. Just to give an order of magnitude, one says that the ratio of plastic strain to elastic strain is below unity:

$$\frac{\varepsilon_p}{\varepsilon_e} < 1 \quad (7)$$

This means that the fracture forces are below the forces that could produce slips but are higher than the debonding forces. On another hand, the damage is called ductile when it occurs simultaneously with the plastic deformations larger than a certain threshold.

3.4 Smeared crack approach

The smeared crack approach can be seen as an intermediate between fracture mechanics and continuum damage mechanics. Attention is not focused on one large crack, but the material damage is modelled with small cracks in element integration points. These cracks may initiate and lengthen according to certain loading criteria. The cracks are not really modelled but simulated with anisotropic material behaviour, where in one direction the material stiffness is reduced. Smeared crack models decompose the total strain in two parts: one corresponds to the deformation of the uncracked material, and the other is the

[1] *Mesoscale is to represent the micro structure of the material using structural elements. It is more sophisticated than just using very small mesh size.*

contribution of cracking. The response of the uncracked material can be governed by a general nonlinear material law but usually, is assumed to be linear elastic. In one-dimensional setting, the strain decomposition is written as: $\varepsilon=\varepsilon_e + \varepsilon_c$ (***Figure 3.2***) and the elastic strain ε_e is related to stress by Hooke's law.

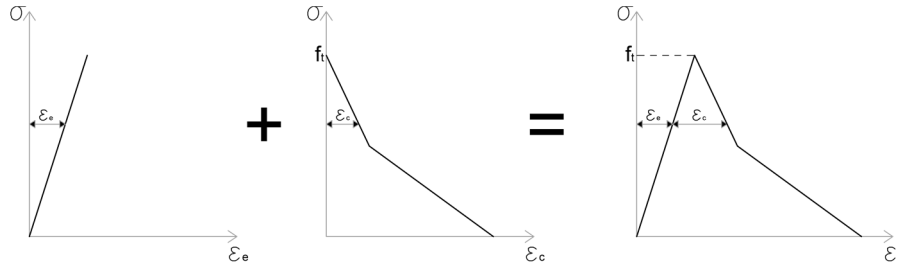

Figure 3.2: total stress-strain curve (σ-ε) obtained by the sum of elastic strain ε_e and crack strain ε_c (**Jirásek 2016**).

The crack strain, ε_c, represents in a smeared manner the additional deformation due to the opening of cracks. The additive stain decomposition corresponds to a rheological model in which an elastic spring is coupled in series with a unit representing the contribution of the crack. Since the coupling is serial, both units transmit the same stress σ.

Chapter 4
Shear failure mechanism of Cross Laminated Timber

The mechanical behaviour with particular reference to stiffness and limit loads of a single CLT element has often been the subject of the scientific research that has provided significant results on the performance of the material. In general, investigations on the in-plane shear strength of CLT by testing can be classified in (i) investigations performed on whole CLT elements (Bogensperger, Moosbrugger, and Schickhofer 2007; Andreolli, Rigamonti, and Tomasi 2014), and (ii) investigations carried out on single nodes (Wallner 2004; Jobstl, Bogensperger, and Schickhofer 2008).

However, a significant number of aspects still have to be investigated. In (Bosl 2002) the author reports on tests conducted on five-layer CLT elements with dimension 1200 x 1200 x 85 (5x17mm) mm^3. The elements are freely placed in a squared, diagonally in tension loaded four-hinged steel-frame. Consequently, the CLT is stressed in shear and compression. In all four specimens with orthogonal layers, the ultimate load is limited by buckling of single boards in the top layers as consequence of delaminated layers. The mean ultimate load was $F_{max,mean}$ = 325 kN, which corresponds to shear stresses of $\tau_{gross,mean} = \tau_{0,mean}$ = 2.3 N/mm^2 and $\tau_{net,mean}$ = 5.6 N/mm^2.

From this, the study of (Bogensperger, Moosbrugger, and Schickhofer 2007) was inspired, aims to develop a new test configuration for CLT elements. The authors define a representative element, namely "*sub-representative element of the volume* (RVSE)", as a fundamental element for a better understanding of the mechanical behavior. As described in the study, when the CLT wall acts under in-plane shear loads, two basic mechanisms, namely shear bearing mechanism I (in the boards) and torsion-like mechanism II (in the glued interfaces) were activated (***Figure 4.1***). With reference to (Bogensperger, Moosbrugger, and Schickhofer 2007), in (Jobstl, Bogensperger, and Schickhofer 2008; Jobstl et al. 2004) the theoretical considerations about mechanism I and mechanism II are reported.

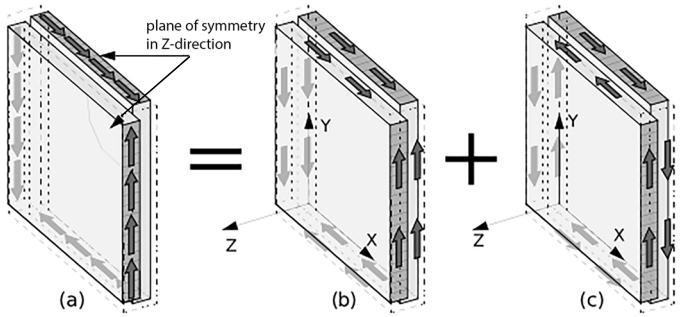

Figure 4.1: *superposition of load carrying mechanisms, (a) real shear stress τ_{net} (superposing b and c), (b) nominal shear stress τ_0 and (c) torsional stress τ_{tor} on the glueing interface.* (***Bogensperger, Moosbrugger, and Schickhofer 2007***)

The mechanism I consider the transfer of shear forces via the cross-section of boards within the RVSE. Shear strain in the RVSE, in the case of faulty or missing connection between the board edges, also causes torsional strain in the surface bond layer, namely mechanism II.
A similar method based on translational equilibrium considerations were adopted by authors in (Andreolli, Tomasi, and Polastri 2012; Andreolli, Rigamonti, and Tomasi 2014) to determine the internal stress pattern. The expressions to evaluate the shear stress and the torsional stress in the external and inner layers were presented in the case of a three and five layers CLT elements. The earlier mentioned papers, through different expressions, permit one to characterise the internal shear stress knowing the geometry of the CLT element and its shear failure load. The authors provided a maximum value of shear stress ($\tau_{net,mean}$) of about 12.7 N/mm^2.
In (Flaig and Blass 2013) the authors explain that in the CLT element, the shear stress distribution can be assumed constant over the element thickness. In the section that coincides with unglued joints between neighboured boards, within the individual layer, shear force can hence only be transferred by the boards arranged perpendicular to the joints. The shear stresses in these net cross sections will consequently be greater than in the gross cross sections among the unglued joints. The transfer of shear forces between longitudinal and transversal layers also causes shear stresses in the crossing areas of orthogonally bonded lamellae. Thus, considering both shear stresses in the lamellae and the crossing areas three different failure modes can be distinguished in CLT elements subjected to shear stresses as shown in ***Figure 4.2***.

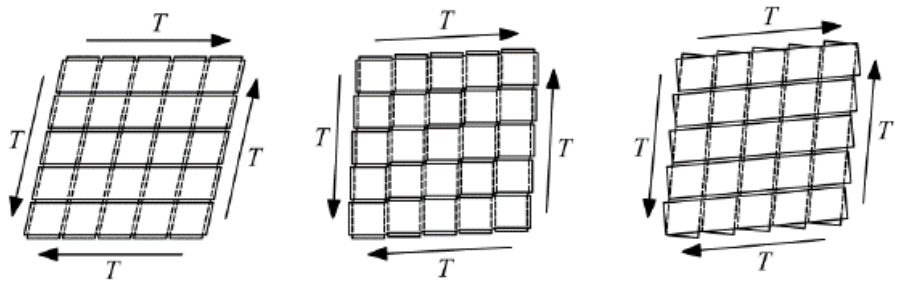

Figure 4.2: *failure modes I, II and III (from left to right) in CLT element subjected to transversal forces in the plane direction* ***(Flaig and Blass 2013)***.

The first failure mode is characterised by shear failure parallel to the grain within the boards. The failure occurs between the unglued surface in a longitudinal direction and transversal layers. In general, the cross section of the individual lamellae are rather small, and transversal layers prevent the development of crack. The second mode of failure is characterised by shear failure perpendicular to the grain, in the net cross section within the unglued joints of boards (Wallner 2004; Jobstl, Bogensperger, and Schickhofer 2008). The failure occurs in section coinciding with unglued joints with shear stresses only in lamellae perpendicular to the joints. The third failure mode is characterised by a shear failure within the gluing-interfaces between the orthogonal layers (Blass and Goerlacher 2002; Jeitler 2004; Jobstl et al. 2004). The failure is caused by torsional shear stresses resulting from the transfer of shear forces between adjacent layers. In fact, in CLT element subjected to transversal forces in plane direction failure in the crossing areas is caused by the interaction of at least two shear stress components, since both torsional shear stresses and shear stresses in the direction of the element axis always occur simultaneously. In failure mode III, the interaction of the different shear stress components has to be considered.

About investigations on nodes, in recent years the shear strength of crossing areas against both shear forces and torsional moments has been determined in several test series.

From the different test series that were performed with small specimens reported in ***Table 1***, it can be concluded that the shear strength of crossing areas against unidirectional shear stresses is equal to the rolling shear strength of the timber. The torsional shear, in contrast, exceeds this value considerably, although the failure is also governed by rolling shear stresses. The torsional shear strength found by (Blass and Goerlacher 2002) and (Jobstl et al. 2004), respectively are very similar, both mean and characteristic values. The results within either test series also showed no significant influence of the crossing area size on the shear strength.

Author	Description of test setup	$f_{v,tor,mean}$	$f_{v,tor,k}$	$f_{R,mean}$	$f_{R,k}$
(Blass and Goerlacher 2002)	Single crossing areas	3.59	2.82	-	-
(Jobstl et al. 2004)	Single crossing areas	3.46	2.71	-	-
(Wallner 2004)	Two symmetric crossing areas	-	-	1.51	1.18
(Flaig and Blass 2013)	Two symmetric crossing areas	-	-	1.43	1.18
(P. Mestek and Dietsch 2014)	7-layers CLT inclined by 10°	-	-	1.42	-

Table 1: *torsional shear strength and rolling shear strength of crossing areas determined by tests with small specimens, expressed in N/mm².*

(Wallner 2004) investigated the rolling shear strength and stiffness nodes, in particular of the glueing interface, on three layers CLT. The set-up is the symmetrical three-point bending test with a loading in compression. Besides primary failures in rolling shear at the glueing interface, also shear failures parallel to the grain in the horizontal board are observed. In that cases, the mean shear stresses $\tau_{net,mean}$ at the failure of several test series are in the range of 5.9 to 7.0 N/mm^2. The rolling shear strength is substantially influenced by the dimension of the single lamella, the lay-up and the production. Due to the system effect of the parallel boards within a layer, an increase of the rolling shear strength of the basic material (1.0 N/mm^2 according to DIN 1052:2004) can be expected. Based on the existing approvals, the rolling shear strength ranges from 0.7 N/mm^2 to 1.5 N/mm^2 (Unterwieser and Schickhofer 2014). One reason for this band can be seen in the production process of CLT. In compliance with the ratio between the width and the thickness of the lamella, $b/t \geq 4$ and for edge bonded CLT, the rolling shear strength is determined as 1.25 N/mm^2. In the context of CLT without edge bonding and the ratio $b/t \geq 4$ is ignored, it is highly advisable to consider the rolling shear strength as 0.7 N/mm^2.
Based on (Wallner 2004) an adapted test configuration was developed for determining the bearing capacity of a single node (Jobstl, Bogensperger, and Schickhofer 2008). The set-up provides two possible failure planes of the cross section at the vertical gaps. The authors did 20 tests with flat grain board material which all successfully failed at the cross sections. They determined a mean value of the corresponding shear strength perpendicular to the grain of 12.8 MPa and a characteristic value of 10.3 MPa by tests.

4.1 The Cohesive Zone Model

Damage in a material can be tracked through the material separation by the introduction of a Cohesive Zone Model (CZM).
The CZM represents the mechanical processes ahead of the crack tip in the fracture process zone (W. Li and Siegmund 2002), and is the simplest method that

allows describing in full a failure process from initiation to propagation of the crack. This approach has been used to treat several materials such as fibre-reinforced materials, delamination in double metal cantilever beams or the composite material, polymers, ceramics, concrete, glass, wood and others.

To our knowledge, the first application of the cohesive model to fracture behaviour of material was performed by Hillerborg as early as in 1976 (Hillerborg, Modeer, and Petersson 1976) who used this model to describe the damage behaviour of concrete.

The CZM is controlled through the definition of the cohesive traction-separation law; also known as cohesive law, between two surfaces. The cohesive traction-separation law is defined primarily by two main parameters: maximum surface traction, known as the cohesive strength, and the corresponding displacement, known as the critical separation (Volokh 2004; Scheider 2001). These quantities define the "height" and the "width" of the curve and give (together with the function of the curve) the dissipated energy per cohesive element as a result. The damage, in the following denoted as *D*, is defined as the ratio of the actual to the maximum separation (δ/δ_0).

The constitutive behaviour of the cohesive model describing the loss of load-bearing capacity of the material as a function of a separation. The separation of the cohesive interfaces is calculated from the displacement jump [u], i.e. the difference of the displacements of the adjacent continuum elements, ($\delta = [u] = u^+ - u^-$).

More common than the definition of the separation vector in global coordinates is the description in a local coordinate system, namely the distinction between normal separation, δ^N, and tangential separation, δ^T. The separation depends on the normal and the shear stress, respectively, acting on the surface of the interface. When the normal or tangential component of the separation reaches a critical value δ^N or δ^T, respectively, the continuum elements initially connected by this cohesive interface, are disconnected, which means that the material at this point has failed.

There are several traction-separation models in the literature that can represent the fracture processes. These models differ in the functional form used to define the curve of the Traction-Separation Law (TSL).

Some of the commons forms, or shapes, that are published in the literature are: the bilinear (Maiti and Geubelle 2005), trilinear (Scheider and Brocks 2003), polynomial (Siegmund and Brocks 1999), parabolic (Scheider 2001), exponential (Volokh 2004), and trapezoidal (Siegmund and Brocks 1999).

The most frequently and widely used form of the traction-separation law is the exponential, employed with minor variations. Some of the shapes of the cohesive law used in cohesive zone modelling are provided in **Figure 4.3.**

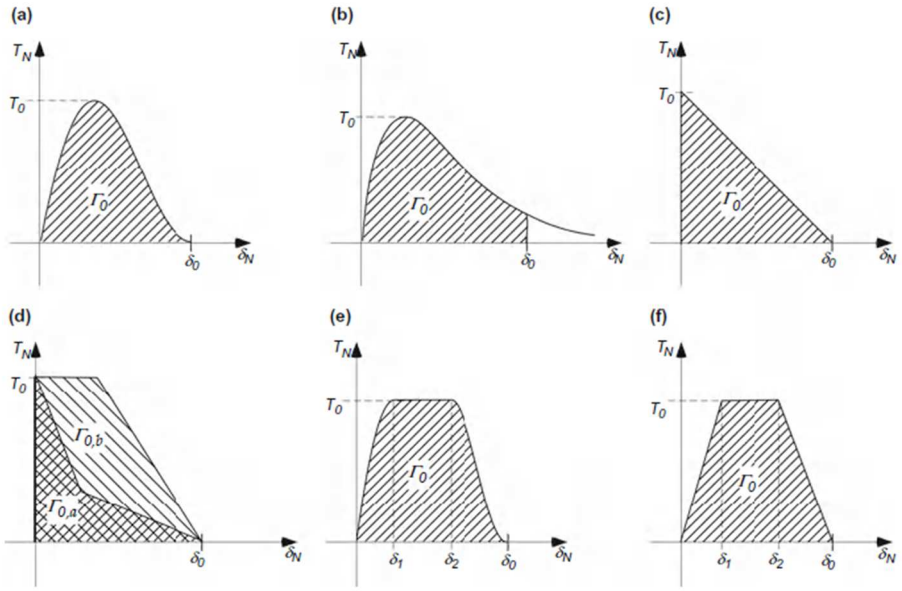

Figure 4.3: *various forms of the traction-separation law used to define the cohesive zone models: a* **(Needleman 1987)**, *b* **(Needleman 1990)**, *c* **(Hillerborg, Modeer, and Petersson 1976)**, *d* **(Bažant 2001)**, *e* **(Scheider and Brocks 2003)**, *f* **(Tvergaard and Hutchinson 1992)**.

As mentioned before, for a given shape of the TSL, the two parameters, δ_0 and T_0, are sufficient for modelling the complete separation process. In practice, it has been proven useful to use the cohesive energy, Γ_0, instead of a critical separation. The cohesive energy is the work needed to create a unit area of fracture surface, and is given by:

$$\Gamma_0 = \int_0^{\delta_0} T\,(\delta)\, d\delta \qquad (8)$$

In a FEM using the CZM approach, the complete material description is separated into fracture properties captured by the constitutive model of the cohesive surface and the properties of the bulk material, captured by the continuum region. The material degradation and separation are concentrated in a discrete plane, represented by a "*cohesive element*" that is embedded in the continuum elements representing the surrounding material. The cohesive element generically defined as adhesive joint, fracture surface, interface or similar, fails when the separation attains a specific critical value, corresponding to δ^N or δ^T.
In this method, the continuum elements remain undamaged and are defined by arbitrary material properties (Scheider 2001). Meanwhile, the cohesive interface elements are used to define and track the damage state of the material. These interface elements can separate at the onset of damage and upon failure, the stiffness of the element is lost, leading to the disconnection of the continuum elements, known as a material failure (Scheider 2001). The selection of the shape

of the CZM is an essential part of being able to describe the fracture process accurately and it can affect the numerical simulations (Volokh 2004). All of the CZMs have the ability to capture the increasing traction on the separation of the crack surface until the peak traction is achieved. Once the peak traction has been reached, the traction approaches zero with a continued increase in the separation. Under single-mode loading, interface damage initiates when the traction reaches the maximum nominal interfacial strength (τ_0). For mixed-mode loading, damage onset is predicted by a criterion established in terms of the normal and shear tractions. Crack propagation occurs when the energy release rate reaches a critical value G_C. The CZM approach prescribes the interfacial normal and shear tractions that resist separation and relative sliding at an interface.

While most of the models in the literature were developed and implemented for mode I of fracture, (Park, Paulino, and Roesler 2009) presented the Park-Paulino-Roesler potential based Cohesive Zone Model that is derived from physical field equations for mixed-mode fracture. This approach can represent a wide variety of failure responses. This is achieved by describing different cohesive strength, fracture energies, and material softening behaviours.

A model for fatigue crack growth via damage evolution capable of modelling mixed-mode fracture has been developed by (Ural, Krishnan, and Papoulia 2009). This model utilises the bilinear shape of the traction-separation law incorporating a degrading peak traction and stiffness behaviour due to the damage evolution under fatigue loading. The cohesive zone degradation model uses a scalar damage variable, which has values between 0 and 1. The damage variable gives the degradation model a phenomenological framework, in which the nonlinear processes that occur if the fracture zone are captured.

A penalty methodology is presented by (Diehl 2008a; Diehl 2008b), who suggests the use of CZM within the finite element analysis when the bond is characterised only by the critical energy release rate, G_c. The author observes that the strength of the interface is a physically measurable quantity, although often it may be difficult to measure it experimentally. Thus, Diehl provides an alternative approach to estimate the elastic stiffness of the cohesive element based on classical fracture mechanics. He considers that the fracture toughness was known from literature or experiments while the strength of the interface was assumed to be either know or unknown. The concept of the penalty method was to convert the CZM into a similar classical Griffith's energy criterion, only dependent by G_c, which assume that the bond or cohesive material was infinitely stiff in its bonding directions until failure, upon which a finite amount of fracture energy was dissipated. This penalty approach consists of taking the cohesive ductility (failure separation parameter) δ_f close to zero while keeping the area under the traction-separation curve (G_c) constant.

It was important to note that in using the energy-based approach to analyse the fracture and its evolution, one implicitly considers a smeared approach to the problem. It was also important to highlights that this penalty approach was in loss of physical significance for the critical limiting maximum stress, which was not really the critical limit stress of the bond material.

In the following *section 7*, one provides the parameters to the cohesive element, defined in terms of traction-separation behaviour, in the case of strength of interface layer of CLT is known and in the case is unknown, based on the Dihel's penalty approach.

Chapter 5
Experimental program

In order to investigate the behaviour of CLT elements subjected to in-plane loads, twenty-four panels are tested under shear stress. The panel is built of five layers, the dimensions are 640 x 640 mm, with a total thickness of 140 mm. The bottom, the top and the middle layers have the same fibre directions (e_1), whereas the intermediate layers are oriented perpendicularly (e_2). The external face has a thickness of 40 mm, while the middle three layers have 20 mm thick (***Figure 5.1***). About the thickness of the solid wood slab element, thicknesses and orientations of individual layers are symmetrically assembled. In the case of serious deviations from symmetry, potential effects should be investigated.
Each layer consists of smaller wooden elements with a rectangular cross-section, with a width of about 150 mm, these elements are made of coniferous timber (*Spruce Timber*). The five layer are adhesively bonded by thin PolyURethane (PUR) bond lines. In ***Table 2*** are summarised the main characteristic of specimens.

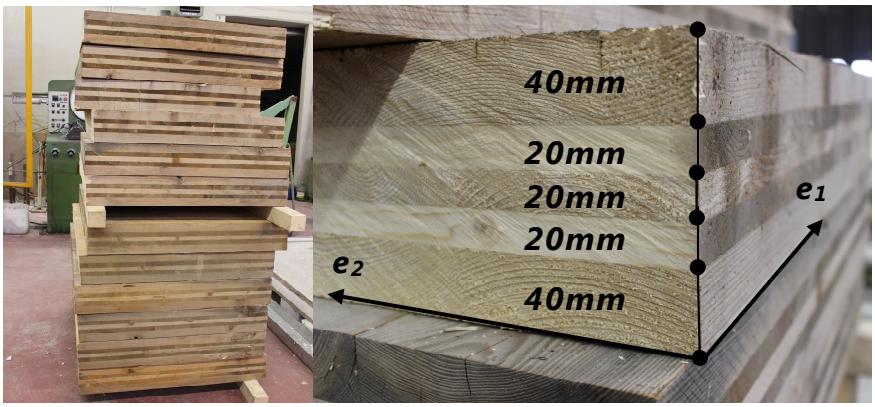

Figure 5.1: *specimens.*

Total Thickness [mm]	Layer Thickness [mm]	Lateral width of boards [mm]	Edge bonded	Number of specimens
140	40 20 20 20 40	150	No	24

Table 2: *tested CLT elements*

The solid wood slab elements are manufactured by the provisions of the European Technical Assessment ('EOTA-ETA-14/0349: Cross Laminated Timber - Solid Wood Slab Elements to Be Used as Structural Elements in Buildings.' 2014) using the manufacturing process as identified in the inspection of the manufacturing plant.

Layers of planed boards are bonded together to the required thickness of the Cross-Laminated Timber. The individual boards are joined in a longitudinal direction according to ('EN 14080:2013 Timber Structures — Glued Laminated Timber and Glued Solid Timber — Requirements - British Standards Institute' 2013). Adhesive is applied on one face of each board, and the edges of the boards are not bonded. The adhesive for bonding the Cross-Laminated Timber is conform to ('EN 301: Adhesives, Phenolic and Aminoplastic, for Load-Bearing Timber Structures - Classification and Performance Requirements' 2013) and (*EN 15425: Adhesives – One Component Polyurethane for Load Bearing Timber Structures – Classification and Performance Requirements* 2008).

The panels are produced using European spruce or equivalent softwood, thus, referring to the technical certificates provided by the manufacturers, it is possible to establish the strength classes of the panel boards: for all panels at least 90% of the boards are C24 strength class and up to 10% of C16 strength class boards. Boards are graded with proper visual and/or machine procedures to be able to assign them to a strength class according to (*EN 338: Structural Timber — Strength Classes - British Standards Institute* 2009).

Before the test, an accurate view of all specimens permits one to identify the existence of shrinkage cracks, knots or other defects in the surfaces. The specimens A1, B10 and B23, present a knots and shrinkage cracks on the external side. Specimen A1 presents, also, a vacuum between the individual boards as shown in ***Figure 5.2***. Specimen B12, B14, B18, B19 and B24 are characterised by the presence of many shrinkage cracks and cuts in both internal and external layers (***Figures 5.3 – 5.9***).

Figure 5.2: *specimen S-1 has the shrinkage cracks (black lines) and presents knots in the external board (black arrows).Also, the red lines highlight the vacuum between the individual boards.*

Figure 5.3: *specimen S-10 has the shrinkage cracks (black lines) and presents knots in the external board (black arrows).*

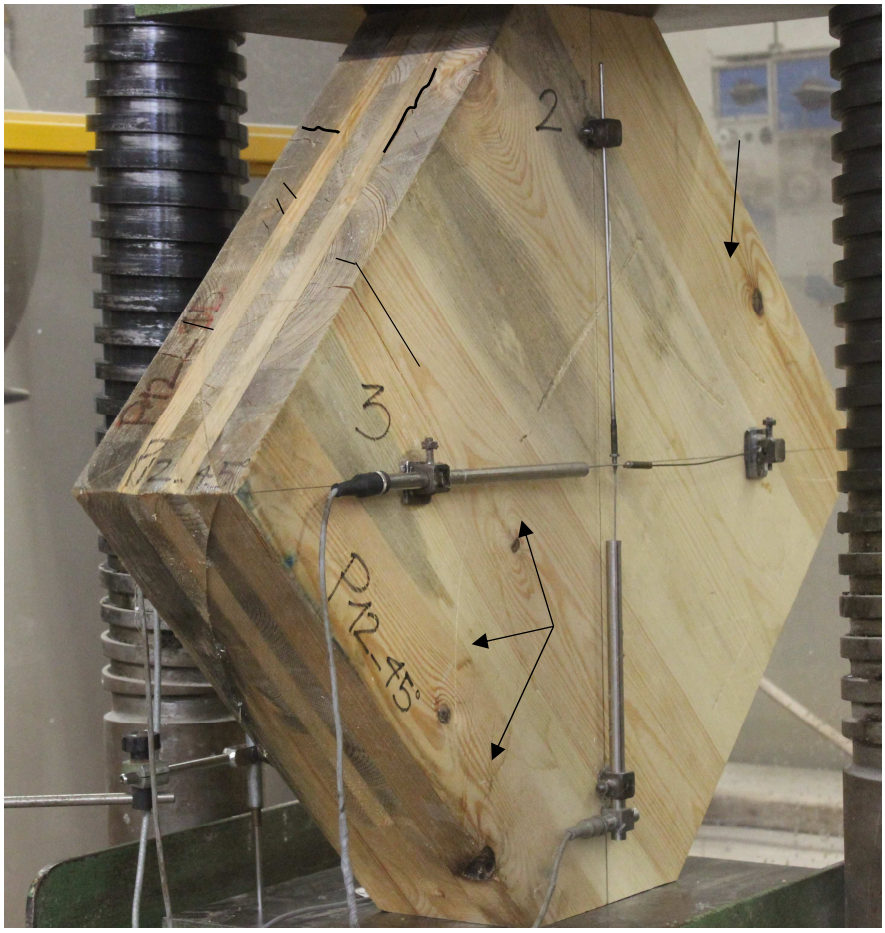

Figure 5.4: *specimen B12 has a cut (black lines) which interests half of the cross section of the external board and presents knots in the external board (black arrows).*

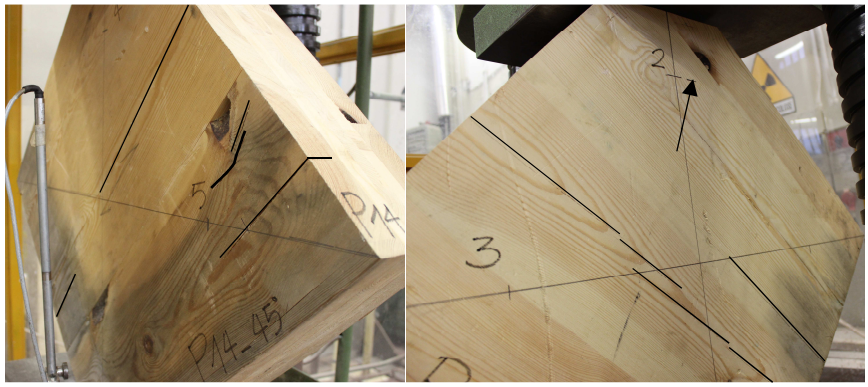

Figure 5.5: *specimen B14 has the shrinkage cracks (black lines) which interest the cross section of the external board.*

Figure 5.6: *specimen S-18 has the shrinkage cracks (black lines) which interest the cross section of the external board and presents knots in the external board (black arrows).*

Figure 5.7: *specimen S-19 has the shrinkage cracks (black lines) which interest the cross section of the external board.*

***Figure 5.8**: specimen S-23 has the shrinkage cracks (black lines) which interest the cross section of the external board and presents knots in the external board (black arrows).*

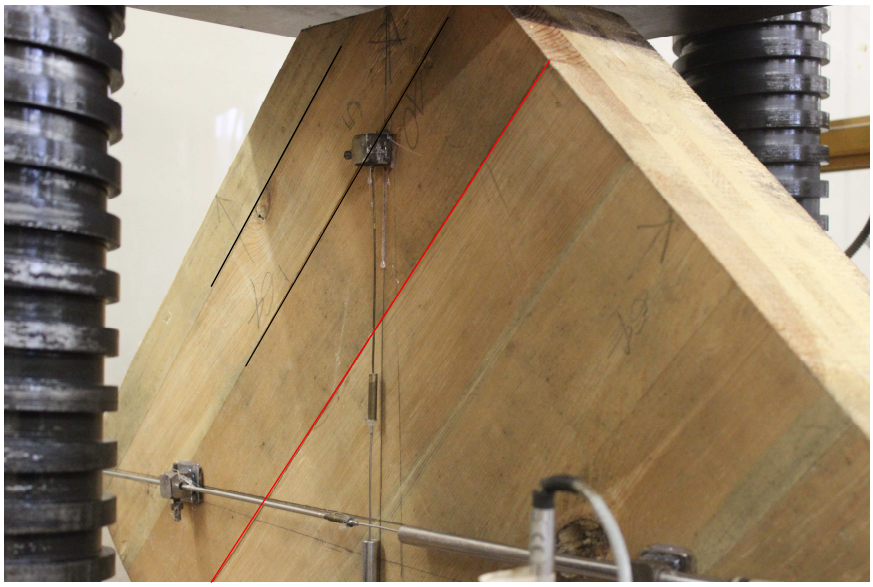

***Figure 5.9:** specimen S-24 has the shrinkage cracks (black lines) in the external board and the red lines highlight the vacuum between the individual boards.*

5.1 Test setup

In the recent years, many research works have been produced with the aim to define a proper test to the determination of mechanical properties of CLT panels. The assessment of the strength of CLT elements subjected to the in-plane

load is more complex, because it involves different failure modes (the main important are the shear failure perpendicular to the grain and the torsion failure in the glue lines between the layers).
At present, the (*EN 16351:2015 Timber, Timber Structure - Cross Laminated Timber - Requirements, CEN* 2015) reports different methods for determining the in-plane characteristics of the material. The regulations define three main test set-up. The first one is the four-point bending test, which is not always useful to determine the shear strength of the CLT elements because it has been demonstrated that often the bending failure is prevalent. The second one is the shear test on the net cross section with an "*ad hoc*" set-up, and the latest one is the torsional test on the glue line between the layers. These latest two methods, which must be performed with the small standard specimens, allow determining the shear strength separately of the net cross sections and the torsional shear strength in the glued surfaces.
As already mentioned in *section 4.1*, the failure in CLT is strongly related to the geometry of the panel (i.e. the width of the boards). Hence, the actual estimation of shear strength perpendicular to the grain and the torsional shear, are possible only with a specific experimental set-up. As reported by (Dujic, Klobcar, and Zarnic 2007; Andreolli, Tomasi, and Polastri 2012) the diagonal compression or tension tests could represent an alternative set-up to define the strength characteristics of CLT elements under in-plane load. In particular, the diagonal compression can show the actual type of shear failure, torsional and perpendicular to the grain.
At the Laboratory of Material and Structure of the Polytechnic University of Marche, in-plane shear tests on the twenty-four CLT specimens are carried out. The test set-up used a universal machine for the compressive test (***Figure 5.10***). The panel is positioned vertically in the bottom flat surface of the machine and is excited by the upper plate of the compressive machine. In this configuration, the square specimens, which are cut out in the two opposite corner and of 45° rotated respect to the main grain orientation of CLT element, are tested in compression (see ***Figure 5.11***).
During the tests, the displacement is measured on both side faces of the specimen, a total amount of four instruments are positioned on the panel as shown in ***Figure 5.11***. Two Linear Displacement Transducers (LDT) measured the horizontal displacement (Δ_x), and two measured the vertical displacement (Δ_y), another one LDT is positioned on the upper side of the compressive machine to measure the absolute vertical displacement (Δ_{TOT}). A load cell measured the applied load during the tests.

Figure 5.10: *diagonal compression tests setup.*

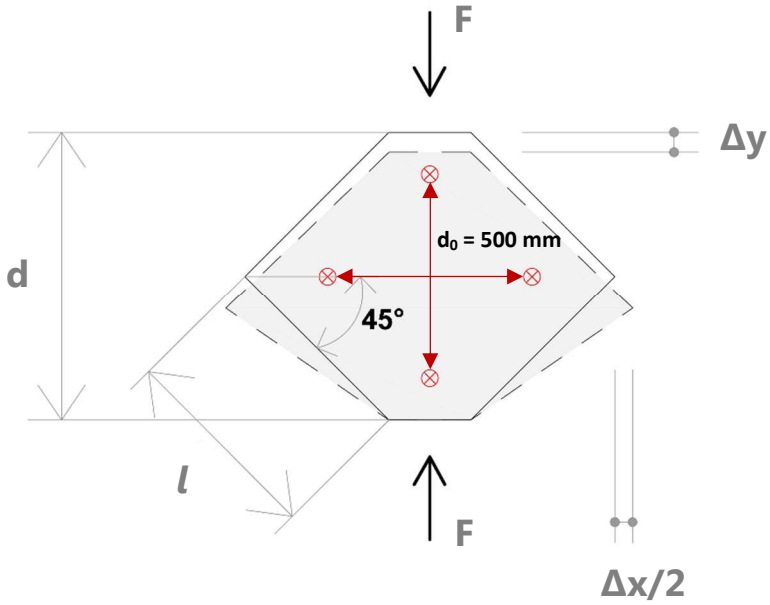

Figure 5.11: *configuration for testing shear by loading in compression, including measurement of horizontal and vertical displacement.*

The monotonic load is applied to all specimens.
In all cases, the deformation is determined on both side faces of the specimens using centrally placed measurement crosses featuring a measuring distance (d_0) equal to 500 mm. In all cases, the LDTs are removed after the decreasing at approximately 50% of F_{max}.

Chapter 6
Experimental results

In this section, the relationship between the applied load and the recorded displacements are given in terms of load-displacement curves and discussed in details. The results are reported in terms of maximum load reached failure for each specimen. They are summarised in ***Table 3***, which also reported the mean values of the maximum load referred. The average peak value for loading in compression are 414.67 kN.

All load-displacement curves show similar characteristic behaviour in all specimens. The load-displacement curve can be divided into two main parts: the first part consist of an almost linear elastic course up to an ultimate load (F_{max}). The subsequent second part consists of load drop, which either exhibits a parabolic or straight shape until collapse is reached. The latest part is a clear softening property, where failure due to a shear mechanism can be observed (***Figure 6.1***). In the first part, a linear elastic material behaviour within approximately $0.2 < F_{max} < 0.8$ is given, followed by a non-linear relationship until F_{max}. At this point, combined mechanisms of "net shear" (type I) and "torsion" (type II) takes place, initiated by a locally exceeded resistance where the shear and tension perpendicular to the grain interacted. In the second part, after the peak load, the softening law is characterised by a load drop until a steady state at about 50% of F_{max}, reaching significant deformation (***Figure 6.1***). The softening law and the followed steady state denote a dissolution of the material due to separation in correspondence of annual rings and the failure of bond interfaces. The load-displacement curves are shown in ***Figure 6.1.*** In all cases, the tested specimens reached the collapse showing a combined failure of shear mechanisms, ***Figure 6.2***.

Specimen ID	Maximum Load [kN]
S-1	385.72
S-2	415.69
S-3	404.24
S-4	456.98
S-5	388.68
S-6	410.29
S-7	397.04
S-8	401.93
S-9	383.27
S-10	413.10
S-11	461.70
S-12	452.70
S-13	473.14
S-14	374.27
S-15	420.81
S-16	413.87
S-17	397.03
S-18	427.24
S-19	401.66
S-20	416.06
S-21	421.90
S-22	433.29
S-23	454.89
S-24	353.57
Mean Value [kN]	**414.67**
Standard Dev.	**28.85**

Table 3: *results of the destructive tests: maximum load achieved during the tests.*

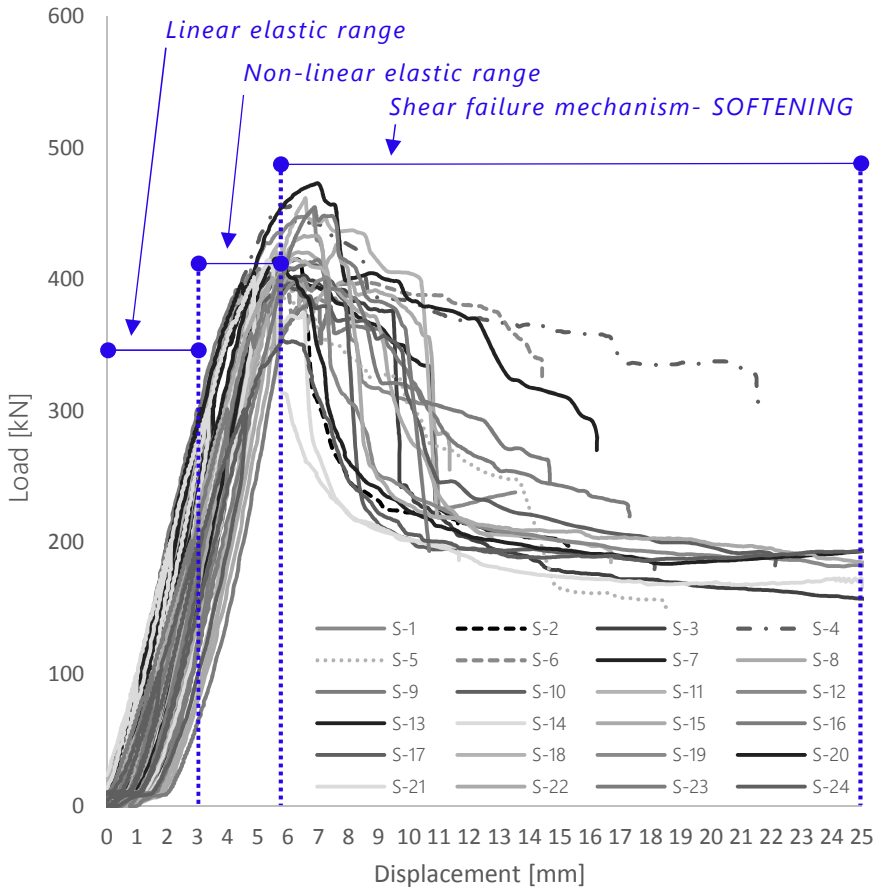

Figure 6.1 *representative load-displacement curves.*

Figure 6.2: *failure paths at the end of the shear test, lateral view of specimen S-5.*

Observing the tests performed in the laboratory can be defined a specific type of failure that characterised all samples. This mechanism, as well as explained and defined by (Brandner, Bogensperger, and Schickhofer 2013), leads cracking of the CLT panel through a combination of pure shear mode and "rolling shear" mode. In each tested specimen, the combination of these actions, which constitute the typical failure mechanism of the panels, is well recognised. We can identify cracks which propagate transversely through the fibre within the board (pure shear mode) and at the same time cracks that propagate following the growth rings orientation (rolling shear mode). ***Figures 6.3*** and ***6.4*** clearly show an example of the different types of cracking that affect the panel and how these simultaneously propagated through the material. Of course, in CLT elements composed of layers without bonded edge, the shear force can only be transferred through the cross sections of boards and through the glue lines of the bonded face. Thus, is reasonable to consider that, in first, the transfer of shear forces via the cross sections of boards is possible as long as a sufficient connection between the edge of boards is present, the mechanism I. Then, an insufficient or missing connection causes also the torsional strain in the glue lines takes place. This may cause failure in the glued interfaces, namely mechanism II or "torsion", (***Figures 6.5-6.6-6.7***). The interface becomes the preferential plane for the shear strain, and this feature will extensively study in the next sections, where the focus is the modelling of the panel.

Figure 6.3: *failure paths at the end of the shear test, frontal view (left) and bottom side (right) of specimen S-4.*

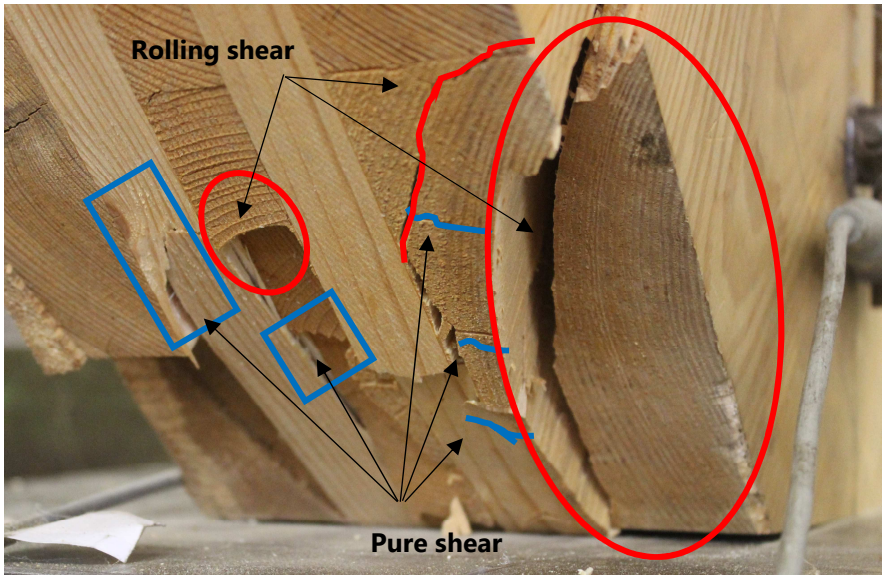

Figure 6.4: *failure paths at the end of the shear test, the bottom side of specimen S-15.*

Figure 6.5: *damaged configuration at the end of the shear test of specimen S-20.*

Figure 6.6: *failure paths at the end of the shear test, lateral view (left) and a frontal view (right) of specimen S-20.*

Figure 6.7: *failure paths at the end of the shear test, lateral view (left) and a frontal view (right) of specimen S-24.*

The experimental maximum loads achieved in each diagonal compressive test groups (***Table 3***) are used to calculate the shear stress values according to the mechanical model proposed in (Andreolli, Rigamonti, and Tomasi 2014) using the following formulas:

$$\tau_{zy} = \frac{F_{max}}{a \cdot (t_1 + t_3 + t_5)} \tag{9}$$

$$\tau_{yz} = \frac{F_{max}}{a \cdot (t_2 + t_4)} \tag{10}$$

Where t is the thickness of the boards and a is the width of the CLT panel. With the same mechanical model is possible also calculate the torsional stress in the layers, assuming the polar torsion, as following:

$$\tau_{tor} = \frac{M_{tor}}{I_p} \cdot \frac{a}{2} = 3 \cdot \tau \cdot \frac{t_l}{w_l} \tag{11}$$

where M_{tor} is the torsional moment, I_p is the polar moment of inertia, τ is the shear stress value, t_l is the thickness of the boards and w_l is the width of the boards. From *equation (11)* is clear that in a CLT element with varying layer thicknesses

the thickest layer governs the behaviour of the panel and consequently τ_{tor} depends on the geometric ratio t_l/w_l. In general, CLT is constructed out of boards of prismatic cross section and has a thickness t_l of 12-45 mm (*EN 16351:2015 Timber, Timber Structure - Cross Laminated Timber - Requirements, CEN* 2015). Due to rolling shear stresses in layers of CLT, a minimum width of $w_l \geq 4\ t_l$ is proposed, otherwise a reduced resistance in rolling shear has to be considered. The reason for this is the increasing amount of tension perpendicular to grain stresses which, together with rolling shear stresses in transverse layers, lead to a remarkable decrease in resistace. EN 16351 (2015) gives the range for the board width w_l as 40-300 mm.

Concerning the resistance of a CLT against torsion, several investigations are made, (Bogensperger, Moosbrugger, and Silly 2010; Blass and Goerlacher 2002; Jobstl et al. 2004; Brandner et al. 2016). A possible redistribution of torsional stresses from zones exposed to rolling shear to zones exposed to shear is mentioned and the authors indicate a mean torsional shear strength of about 3.60 N/mm^2, while a mean rolling shear strength of about 1.50 N/mm^2.

The main idea of the internal stress pattern is reported in ***Figure 6.8***. This model is based on the research proposed by the researchers of the University of Graz, who define an efficient mechanical model for determination of the internal stress pattern in CLT elements subjected to in-plane loads. The expressions allow evaluating the shear stress in the external and inner layers, τ_{zy} and τ_{yz} respectively. One of the main hypothesis on which the above-mentioned mechanical models are based refers to the edge bonding (Jobstl, Bogensperger, and Schickhofer 2008). It is assumed that the boards are not glued together on their narrow sides.

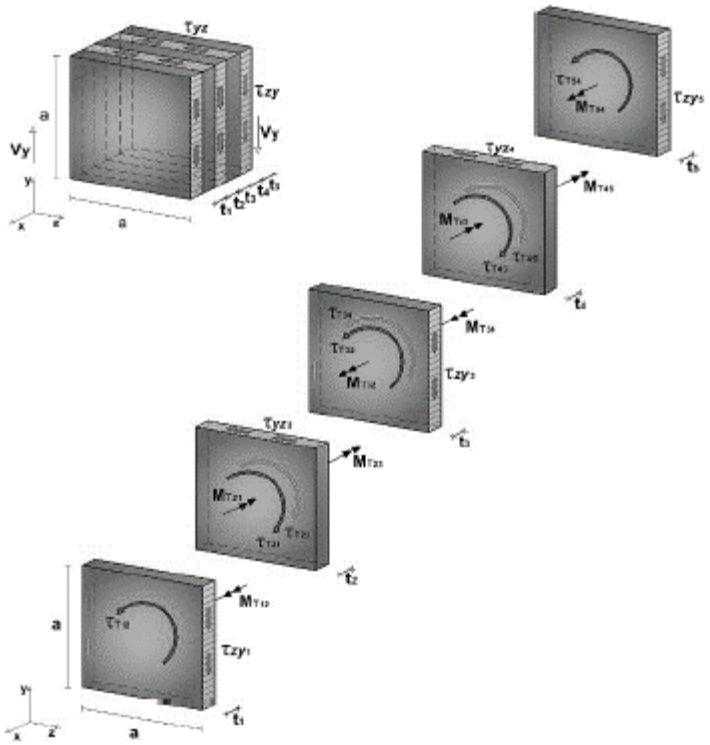

Figure 6.8**: internal stress pattern in a 5-layers CLT element* ***(Andreolli, Rigamonti, and Tomasi 2014).

Also, based on the maximum load achieved in each diagonal compression tests, the pure shear stress value, strain and the shear modulus are determined using the following equations by (Dujic, Klobcar, and Zarnic 2007). The average of the results is summarised in ***Table 4***, which reports also the mean values of the shear stress in the external and internal layers.

$$\tau = \frac{F_{max}}{\sqrt{2} \cdot l \cdot t} \tag{12}$$

$$\gamma = \frac{\Delta_x + \Delta_y}{2d} \left(\tan \alpha + \frac{1}{\tan \alpha}\right) \tag{13}$$

$$G = \frac{\tau}{\gamma} \tag{14}$$

	Mean Value	Stand. Dev.
τ [MPa]	4.21	0.30
τ_{zy} [MPa]	6.48	0.45
τ_{yz} [MPa]	16.20	1.13
τ_{tor} [MPa]	3.89	0.27
$\tau_{rolling}$ [MPa]	1.50	-
G [MPa]	549.32	167.06
γ	8.84×10^{-3}	4.42×10^{-3}

Table 4: *calculated pure shear stress, strain and shear modulus (**Dujic, Klobcar, and Zarnic 2007**) and calculated shear stress in the layers (**Andreolli, Rigamonti, and Tomasi 2014**).*

The experimental results appear to confirm the range of values reported in the literature. The diagrams below (***Figure 6.9*** and ***6.10***), allow an easy comparison between the experimental strength values of the tested specimens for internal shear stress perpendicular to the grain and the strength value reported in the literature by (Jobstl, Bogensperger, and Schickhofer 2008) and according to (Brandner et al. 2016; Wallner 2004; Blass and Goerlacher 2002) for rolling shear strength, respectively. Also the shear stiffness modulus reported in ***Table 4***, which refers to the average of the values assessed in the tests for a single panel, correspond with the mean value of the characteristic shear modulus $G_{CLT,\ mean}$ defined by ('EN 14080:2013 Timber Structures — Glued Laminated Timber and Glued Solid Timber — Requirements - British Standards Institute' 2013) as 650 N/mm^2.

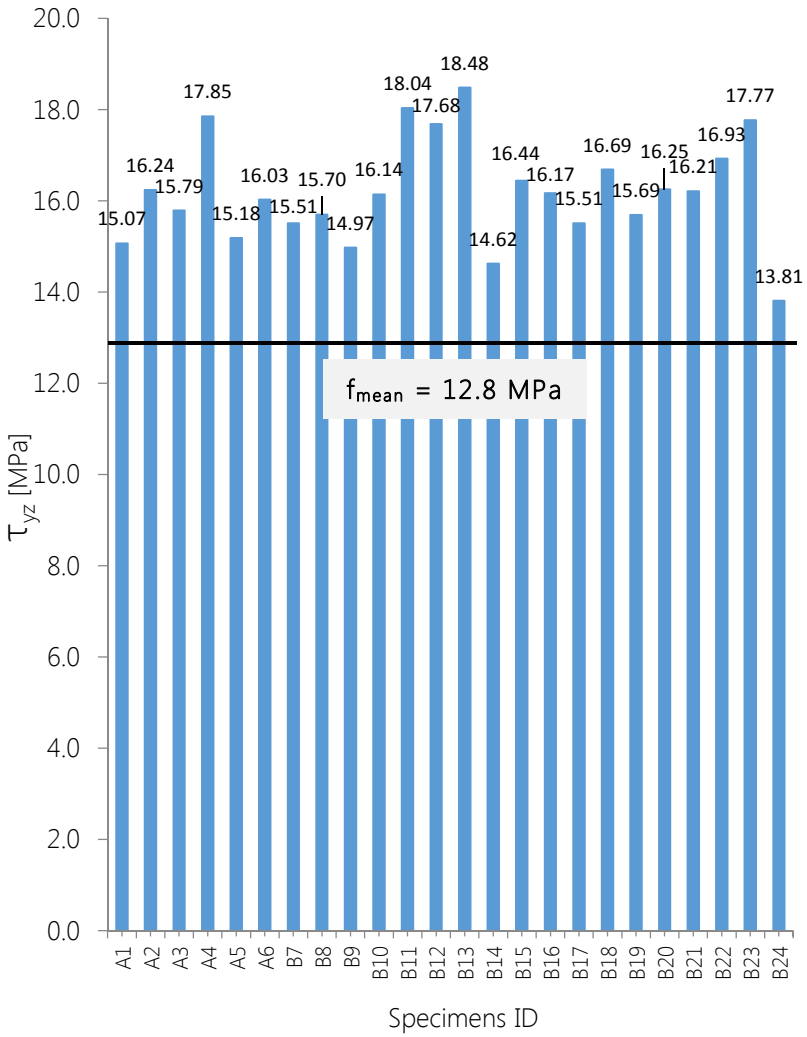

Figure 6.9: *calculated strength values for the specimens tested for shear stress perpendicular to the grain (τ_{yz}) compared to the strength value (12.8 MPa) reported in* ***(Jobstl, Bogensperger, and Schickhofer 2008)****, horizontal line.*

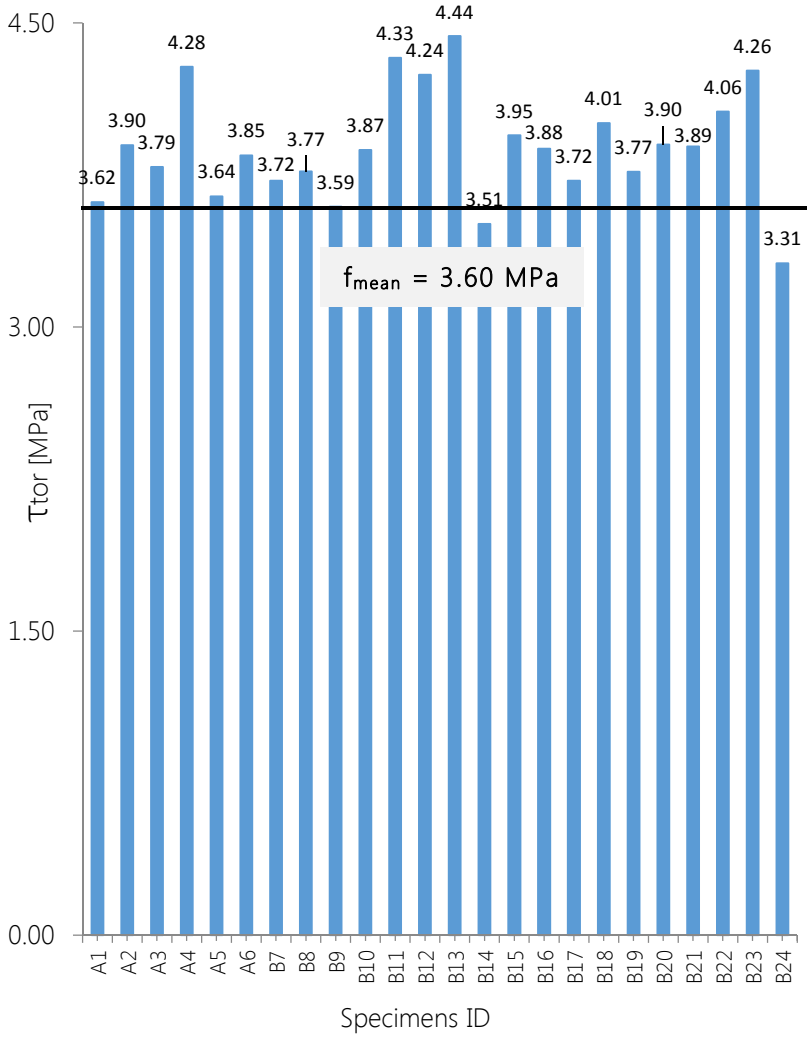

Figure 6.10: *calculated strength values for the specimens tested for torsional stress (τ_{tor}) compared to the strength value (3.60 MPa) reported in* ***(Blass and Goerlacher 2002)****, horizontal line.*

Of course, the effective shear strength of CLT elements depends on the width of lamellae, on the thickness and arrangement of longitudinal and transversal layers within the element. In addition, depending on the composition of the CLT element the shear resistance is governed by either of the three failure modes. By experimental data is possible to determine the strength properties and shear stresses corresponding to the different failure modes.
About the effective shear modulus, it is frequently defined in combination with the strength class of the basic material. As a consequence, the shear modulus ranges between 650 and 690 N/mm^2.

Chapter 7
Numerical Modelling

This chapter will focus on the accurate finite element modelling of the CLT material in the software package. Wood is a cellular material possessing a high degree of anisotropy, which often exhibits a highly nonlinear load-displacement behaviour. Due to the complexity of wood mechanics, of the failure mechanism of timber materials, and new wood-based products, intensive research is inspired over the last few years. Particular attention is given to the CLT elements using homogenization-based multi-scale modelling techniques (E. I. Saavedra Flores et al. 2015; E. I. Saavedra Flores et al. 2016; Ardalany, Fragiacomo, and Moss 2015; Dourado et al. 2008).

The mechanical behaviour of wood is studied from a micro up to a macro level. Dedicated mechanical laws aimed at reproducing the actual wood behaviour over the linear range are not directly available in general purpose commercial code, due to the complex mechanical behaviour of timber. Many approaches have been proposed and employed, but still, there is no general agreement as to the best approach to be adopted. In general terms, there are main two classes of mathematical models used to analyse the wood behaviour: (i) linear elastic (isotropic or orthotropic) material models, usually sufficient to the conventional design of wood elements and members; (ii) material models that take into account failure criteria.

In the present study, the mechanical properties of the CLT are characterised and modelled. First, the linear analysis is performed to calibrate the parameters of the models through the study of the first steps of the mechanical response of the specimens, when the specimen is still in the linear range. Subsequently, a nonlinear analysis is carried out. The discontinuities due to the glue lines and the anisotropic layered structure of the panel taken into account. The continuum properties are derived from literature, and a FEM is performed. Strength and stiffness properties determined by CZM are presented and are compared with experimental data. Simulations of the deformation and fracture of CLT specimens loaded in shear conditions are shown.

The experimental program and results motivated a numerical model with the aim to mirror the load-displacement curves in a satisfying manner. Therefore, a FEM with the cohesive elements is implemented in ABAQUS software package. A three-dimensional (3D) model of the square specimen is realised, boundary

conditions, assigned as fixed restraints, are applied in order to reproduce the experimental set-up (schematized in Figure 5.11 and described in Section 5.2), while the load is imposed as increasing monotonic displacements applied on the surface pushed during the experimental tests.
In the follow the main considerations to realise the model are reported.

7.1 Initial modelling assumptions

Infinitely thin layers of bonding resin exist between the timber layers. Modelling these layers within the wood matrix is hard because the interaction between the resin and the wood is highly dependent upon the individual properties used in each layer of each product. The model used to analyse the behaviour of a CLT product are formed on the main assumption.
The sets of model assume that the timber layers are not affected by the bonding resin used. Subsequently, the resin properties are not used in the calculation of the stiffness matrix of wood. This assumption is made because is neither possible nor viable to accurately ascertain how far the resin absorption will penetrate into the timber elements, nor the effect that this will have on the wood strength properties.
One considers the CZM to study the interface zone. Cohesive interface elements are defined between the continuum elements instead, which open when damage occurs and lose their stiffness at failure so that the continuum elements are disconnected; no continuum elements are damaged in the cohesive model. Using this technique, the behaviour of the material is split into two parts, the damage-free continuum with an arbitrary material law, and the cohesive interfaces between the continuum elements, which specify only the damage of the material. To simulate the problem, four layers of cohesive elements are used to reproduce the 5-layers CLT panel (***Figure 7.1.a***).
In addition, another discontinuous surface is considered to describe the slip surface within the wooden layer to simulate the transverse failure shown by the experimental tests (***Figure 7.1.b***). The hypothesis is that each smaller boards which compose the layer of wood has not edge bonded, thus the interface was idealised using a contact interaction, with the input parameters for the friction formulation. The basic concept of the friction model is to relate the maximum allowable frictional (shear) stress across an interface to the contact pressure between the contacting bodies. In the basic form of the friction model, two contacting surfaces can carry shear stresses up to a certain magnitude across their interface before they start sliding relative to one another. The Coulomb friction model defines the critical shear stress, at which sliding of the surfaces starts. The advantage of using this contact interaction for modelling the slip surface without bond is that it allows an additional simplification of the model. This imposes friction constraint in the normal and shear direction.
In conclusion, the overall model of CLT specimen is described by continuum material to simulate the wood in the linear elastic behaviour, by four cohesive

elements to simulate the bonded interfaces and by five friction surfaces within the wooden layer to simulate the slip between the boards, ***Figure 7.1***.
In *section 7.3*, the mechanical behaviour of the cohesive interfaces is explained.

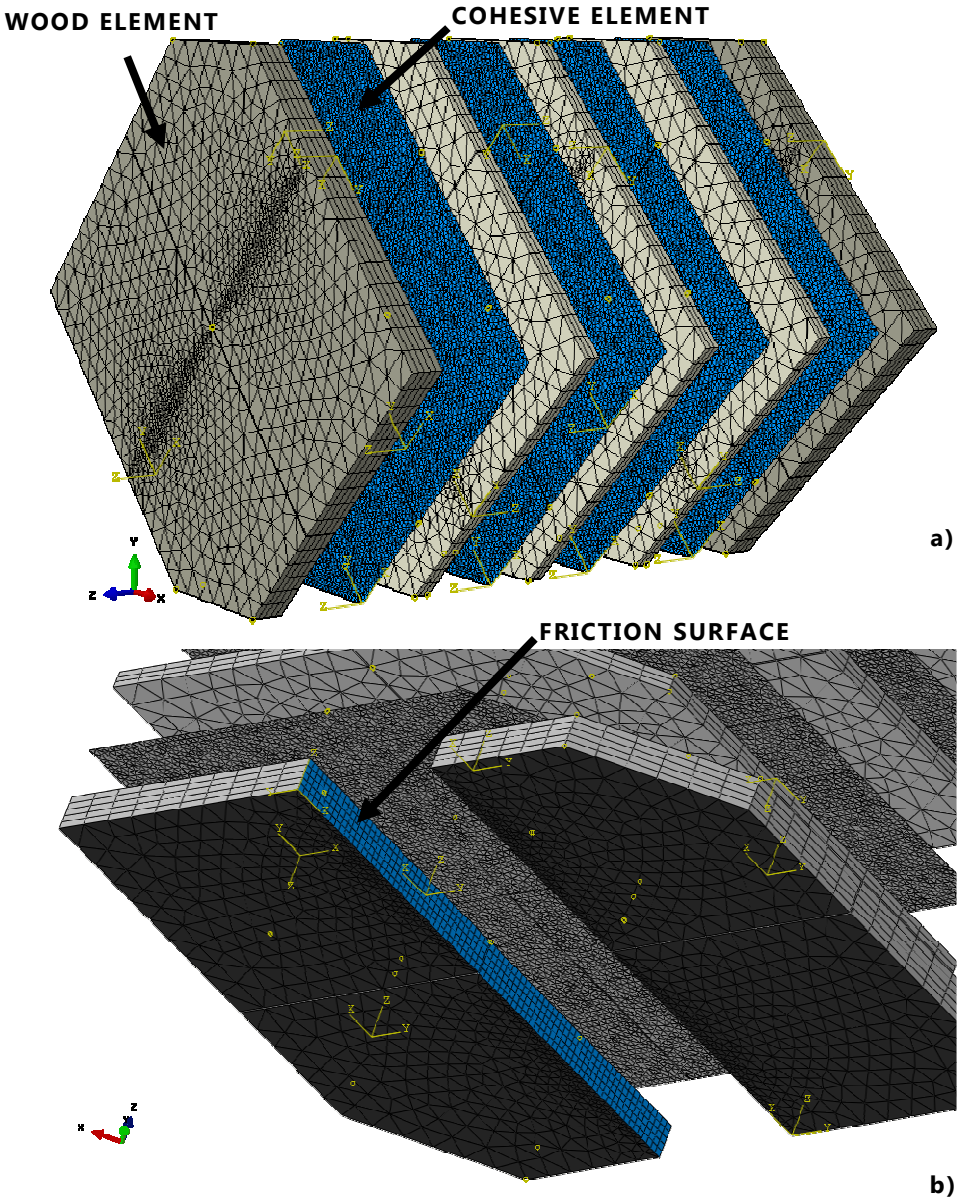

Figure 7.1: *3D FEM, partitioning of CLT specimens: a) five wooden layers and four cohesive elements and their finite element meshes; b) friction surface and its mesh.*

7.2 Constitutive model for timber

Elastic 3D orthotropic modelling of the CLT element is implemented. The elastic analysis is first performed to indicate the point of maximum resistance and the initial stiffness at the specimens. The timber elements to be used in the FEM of the CLT members are to reflect the material properties of the Spruce Timber and the matrix properties of the CLT component will be calculated using the mechanical properties of the Picea Abies. It will be assumed that the resin only supplies a physical bond between the two adjacent timber layers and the resin properties supply no significant increase in strength, nor does the resin affect the mechanical properties of wood. Linear elastic orthotropic material properties are used for the timber boards; the material properties are summarised in ***Table 5***. Linear elasticity in an orthotropic material is defined by nine independent elastic stiffness parameters; the stress-strain relation is of the form reported below, which is the fundamental Hooke's equation:

$$\sigma_{ij} = D_{ijkl}\, \varepsilon_{kl} \tag{15}$$

where σ_{ij} is the second order effective stress tensor, D_{ijkl} is the material stiffness matrix and ε_{kl} represents the second order tensor of elastic strain. The extended form of (15) is reported in (16).

$$\begin{Bmatrix} \sigma_{11} \\ \sigma_{22} \\ \sigma_{33} \\ \sigma_{12} \\ \sigma_{13} \\ \sigma_{23} \end{Bmatrix} = \begin{bmatrix} D_{1111} & D_{1122} & D_{1133} & 0 & 0 & 0 \\ 0 & D_{2222} & D_{2233} & 0 & 0 & 0 \\ 0 & 0 & D_{3333} & 0 & 0 & 0 \\ 0 & 0 & 0 & D_{1212} & 0 & 0 \\ 0 & 0 & 0 & 0 & D_{1313} & 0 \\ 0 & 0 & 0 & 0 & 0 & D_{2323} \end{bmatrix} \begin{Bmatrix} \varepsilon_{11} \\ \varepsilon_{22} \\ \varepsilon_{33} \\ \gamma_{12} \\ \gamma_{13} \\ \gamma_{23} \end{Bmatrix} \tag{16}$$

For an orthotropic material, the nine engineering constants (17) define the D matrix and obey to the following relations with respect to the symmetry requirements (Sandhaas, Van de Kuilen, and Blass 2012):

$D_{1111} = E_1 (1- \nu_{23} \nu_{32}) Y$;

$D_{2222} = E_2 (1- \nu_{13} \nu_{31}) Y$;

$D_{3333} = E_3 (1- \nu_{12} \nu_{21}) Y$;

$D_{1122} = E_1 (\nu_{21} + \nu_{31} \nu_{23}) Y = E_2 (\nu_{12} + \nu_{32} \nu_{13}) Y$;

$D_{1133} = E_1 (\nu_{31} + \nu_{21} \nu_{32}) Y = E_3 (\nu_{13} + \nu_{12} \nu_{23}) Y$;

$$D_{1122} = E_2 (\nu_{32} + \nu_{12}\,\nu_{31})\, Y = E_3 (\nu_{23} + \nu_{21}\,\nu_{13})\, Y ; \quad (17)$$

$$D_{1212} = G_{12} ;$$

$$D_{1313} = G_{13} ;$$

$$D_{2323} = G_{23} ;$$

$$Y = \frac{1}{1 - \nu_{12}\nu_{21} - \nu_{23}\nu_{32} - \nu_{31}\nu_{13} - 2\,\nu_{21}\nu_{32}\nu_{13}}$$

where E_i represents Young's moduli in the three orthotropic directions, ν_{ij} and G_{ij} represent the Poisson's ratio and the shear moduli, respectively.

Material property		
$\mathbf{E_L}$	11000	MPa
$\mathbf{E_R}$	440	MPa
$\mathbf{E_T}$	440	MPa
$\mathbf{G_{TL}}$	450	MPa
$\mathbf{G_{RT}}$	50	MPa
$\mathbf{G_{RL}}$	450	MPa
$\boldsymbol{\nu_{LT}}$	0.015	
$\boldsymbol{\nu_{RL}}$	0.038	
$\boldsymbol{\nu_{TR}}$	0.558	

Table 5: *material properties of timber boards.*

By a thorough literature review, one decides to determine the material parameters from published works on wood species. Thus, the initial values of the mechanical properties are determined from (Dourado et al. 2008; Sandhaas, Van de Kuilen, and Blass 2012; Betti et al. 2016; Brandner et al. 2016) for Spruce timber (*Picea Abies*). Nevertheless, the original values are adjusted to obtain a similar response to that found during the experiments.

7.3 Cohesive element

The basic concept in the CZM approach is that the cohesive element carries loads to hold the CLT layer together until loads and deformations on the cohesive interfaces cause damage and failure. When the element has fully failed, it will have accounted for an amount of energy equal to the critical fracture energy defined for the real failure interface. In the FEM, the cohesive element must have a finite definition of stress and separation over which the fracture energy can be released. In a typical application, the cohesive elements represent a "bond", where the term

bond is generically defined to potentially represent an adhesive joint, fracture surface interface, or similar construct. The bond can be thick, or it can be of zero thickness. The cohesive elements are connected, top and bottom, to the adjoining bodies either by sharing common nodes or through an interface constraint.
During the analysis, the cohesive elements carry loads to connect the two parts together until such a point in the solution exists for which conditions mandate the initiation of damage and potentially complete failure within any given cohesive elements. These criterions are assessed on an element-by-element basis continually throughout the solution.
For the calculations in this work, the FE code utilised is ABAQUS Version 6.12. In ABAQUS, a broad set of cohesive elements features and options are provided so that the user can specify a criterion for each phase of deformation within the cohesive element (undamaged elastic response, damage initiation, and failure). The typical cohesive parameters used to characterise the behaviour of the bond interface in the CZM are: the critical fracture energy (G_C), effective nominal stress (T_{ult}), the damage initiation ratio (δ_{ratio}) and the initial material stiffness per unit area (K_{eff}), ***Figure 7.2***.

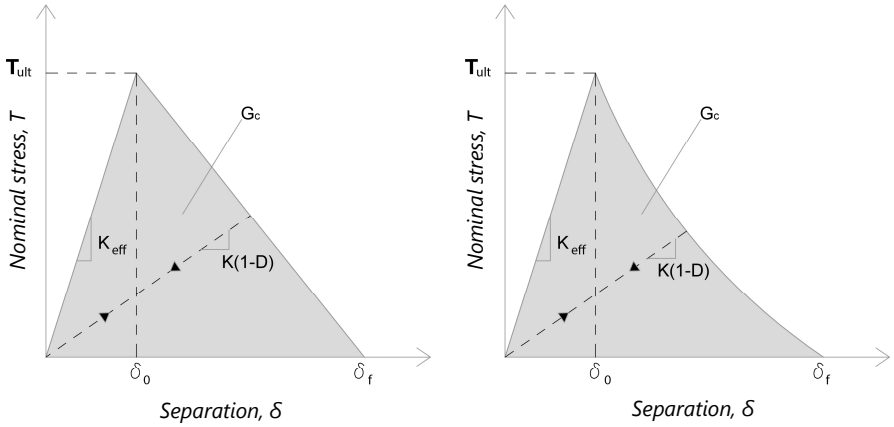

Figure 7.2: *response of cohesive element, linear softening (left) and exponential softening (right)*

Of the four parameters, the most important parameter that would influence the behaviour of the cohesive element is the critical fracture energy, which is equal to the total area under the bilinear traction-separation model. The relationships between each of the parameters are given as:

$$G_c = \frac{T_{ult}}{2\delta_f} \tag{18}$$

$$\delta_{ratio} = \frac{\delta_f}{\delta_0} \tag{19}$$

$$K_{eff} = \frac{T_{ult}}{\delta_0} \quad (20)$$

The above four parameters are specific to the corresponding Mode I and Mode II critical fracture energy values and do not necessarily need to be the same for both failure modes.

The cohesive law exhibits a linear elastic behaviour until the separation δ_0 after that damage occurs and ultimately the element failure was reached for the failure separation value δ_f. This parameter δ_f, in (Diehl 2004; Diehl 2008a; Diehl 2008b) is defined as a characterising value of ductility to the failure of the cohesive layer, thus a small failure separation parameter characterised a very brittle bond while a larger value implies a more ductile bond.

The peak traction in the cohesive relation for a particular mode of fracture corresponds to the interfacial strength in that mode. The interface strength determines the damage initiation point, beyond this point the damage develops in the cohesive zone leading to a reduction in the traction. Experiments for determining interfacial strength is well developed for CLT system, despite this in the followed one reported two different way to estimate the parameters is needed to define the cohesive law. If the interface strength is knowing for the adhesive layer, it can be used to fix the mesh size as discussed below in *section 7.3.2*. However, if the experimental data is lacking, one provides a reasonable estimate of the interfacial strength. The last one strategy treats the interfacial strength as a penalty parameter and determines its value by numerical experiments (Diehl 2008a; Diehl 2008b), this second approach is discussed below in *section 7.3.3*.

However, for an accurate overall explanation of fracture initiation and propagation, the most important property is the fracture toughness defining the damage evolution followed by the interface strength defining the damage initiation and finally the elastic stiffness. Hence the discussion below is presented in this order.

7.3.1 Fracture toughness: damage evolution

Fracture toughness as measured by the critical energy released rate is the single most important parameter that defines the cohesive traction-separation behaviour. The critical energy release rate is commonly referred to as critical release energy or critical fracture energy. It is a material parameter that characterises the amount of energy a bond or fracture surface dissipates per change in unit crack growth per unit depth. For many materials system, the fracture toughness has been or can be measured experimentally. However, the value of separation at the final failure as well as the shape of the softening portion of the traction-separation relation may be difficult to determine. Thus, it is easier to use energy-based damage evolution with linear softening behaviour, and the effect of the shape of the softening response on the overall results may be studied subsequently.

The area under the traction-separation curves for various modes represents the corresponding fracture energies (G_{IC}, G_{IIC}, G_{IIIC}). In problems where the different fracture modes are likely to interact, the mixed mode behaviour must be specified as well. More commonly the fracture energies in pure modes are measured experimentally, and the mixed mode behaviour is specified via certain analytical forms that fit limited mixed-mode experimental data. Whereas the elastic stiffness and damage initiation parameters of the cohesive traction-separation relation can be treated as penalty parameters that can be adjusted, the fracture energies are physical quantities that must be specified accurately.
The damage evolution is the phase after cracking when the stiffness of the elements is gradually decreased and could be energy or displacement based. Different mixed mode fracture criteria could be used for the damage evolution (Jernkvist 2001a; Jernkvist 2001b). The general form of the mixed mode fracture criterion is:

$$\left(\frac{G_I}{G_{IC}}\right)^m + \left(\frac{G_{II}}{G_{IIC}}\right)^n = 1 \tag{21}$$

where G_I and G_{II} are the fracture energies for mode I and II, respectively, G_{IC} and G_{IIC} are their critical energy release rate values, m and n are an empirical parameter derived from mixed-mode tests and denote the power of equation. However, (Camanho, Dávila, and Moura 2003) have shown that the expression proposed by (Benzeggagh and Kenane 1996) for the critical energy release rate for a mixed-mode behaviour is more accurate. The expression proposed by Benzeggagh and Kenane for the critical energy release rate G_C is:

$$G_C = G_{IC} + (G_{IIC} - G_{IC})\left(\frac{G_{shear}}{G_T}\right)^\eta \tag{22}$$

The energy release rate under mixed-mode loading is $G = G_I + G_{shear}$ where $G_{shear} = G_{II} + G_{III}$ (assuming $G_{II} = G_{III}$) is the energy release rate for shear loading proposed by (J. Li and Sen 2000) and by (J. Li 2000). The propagation surface in the displacement jump space is defined through the final displacements, which are obtained from the pure mode fracture toughness (G_{IC}, G_{IIC}, G_{IIIC}) considering that the area under the traction-separation jump curves is equal to the corresponding fracture toughness, i.e.

$$G_C = \frac{1}{2} K \Delta^0 \Delta^f \tag{23}$$

defined by a penalty parameter K, by the mixed-mode damage initiation, Δ^0, and by the total decohesion parameter, Δ^f. The penalty parameter K assures a stiff connection between two adjacent layers before decohesion initiation. The penalty parameter should be large enough to provide a reasonable stiffness but small enough to avoid numerical problems.

7.3.1.1 *Consideration of normal and shear fracture*

Under consideration of simultaneously acting normal and shear fracture one has to define a quantity of damage and failure. As mentioned before, failure occurs in a pure normal fracture when the separation exceeds the maximum value. At combined normal and shear fracture (local in the cohesive element), the quantity that defines failure contains a normal and a shear component, i.e. the shear damage will reduce the ductility in the normal direction and vice versa. This influence of competing for normal and tangential separation is to define an interaction formula of the shear and normal separation:

$$D = \sqrt[m]{\left(\frac{\delta^N}{\delta_0^N}\right)^m + \left(\frac{\delta^T}{\delta_0^T}\right)^m} \tag{24}$$

Equation (24) contains a model parameter *m*, which is a connection parameter. One determines two limiting cases from *equation (24)*, namely $m = 1$, that means a linear connection between normal and tangential damage, and $m \to \infty$, which leads to a vanishing influence of one fracture mode to another. The damage and final failure of a cohesive element are plotted in ***Figure 7.3*** for m=1 and m=2. It should be mentioned that most references (Jernkvist 2001a; Jernkvist 2001b) use $m = 2$ as the damage indicator, for which the damage is equal to the absolute value of separation.

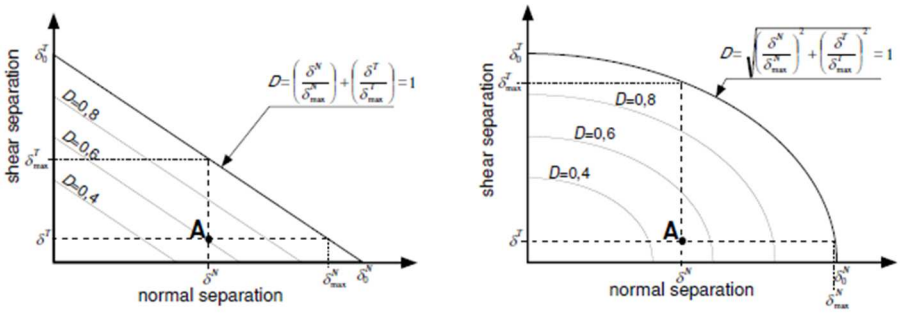

Figure 7.3: *interaction between normal and shear separation.*

As can be seen in ***Figure 7.3***, the maximum normal separation decreases with increasing shear separation. The separation function does not only depend on δ^N, but also on δ^T and the damage D.

7.3.2 *Interface strength was known*

A general rule, in according to ABAQUS guidelines for choosing the cohesive element size, is to use 3-5 cohesive elements per adjacent continuum element in the mesh (see ABAQUS documentation for additional details). However, if the interfacial strength is known from the literature or direct experimentation, it may

be used to assess and/or estimate the size of the cohesive element in the mesh. This estimate is based on embedding a sufficient number of cohesive elements within the Fracture Process Zone (FPZ) that develops in front of a crack tip. For this reason, it is important to define the length of the cohesive element zone (l_{cz}), the distance from the crack tip to the point where the maximum cohesive traction is attained.

Several models have been proposed in the literature to estimate the length of the cohesive zone. Irwin (Irwin 1960) estimated the size of the plastic zone ahead of a crack in a ductile solid by considering the crack tip zone where the von Mises equivalent stress exceeds the tensile yield stress. Dugdale (Dugdale 1960) estimated the size of the yield zone ahead of a mode I crack in a thin plate of an elastic-perfectly plastic solid by idealising the plastic region as a narrow strip extending ahead of the crack tip that is loaded by the yield traction. Barenblatt (Barenblatt 1962) provided an analogue for ideally brittle materials of the Dugdale plastic zone analysis. (Hui et al. 2003) estimated the length of the cohesive zone for soft elastic solids; (Falk, Needleman, and Rice 2001) and Rice (Rice 1980) estimated the length of the cohesive zone as a function of the crack growth velocity.

All of these models described above to predict the cohesive zone length l_{cz} have the form:

$$l_{cz} = ME\ \frac{G_C}{(\tau^0)^2} \tag{25}$$

where E is the modulus of elasticity of the material through which crack propagation is being simulated (CLT "*composite*"), G_C is the interface fracture toughness, τ^0 is the maximum interfacial strength, and M is a parameter that depends on each cohesive zone model.

The most commonly used models in the literature are Hillerborg's (Hillerborg, Modeer, and Petersson 1976) and Rice's model (Rice 1980). In these models, the parameter M is either close or exactly equal to unity.

In the below section *8.2*, one reports the results about cohesive zone length and relative cohesive mesh size at varying of parameter M.

To obtain accurate FEM results using CZM, the cohesive zone must be represented properly by the finite element spatial discretization. Thus, the mesh size (l_e) in the direction of crack propagation can be estimated as:

$$l_e = \frac{l_{cz}}{N_e} \tag{26}$$

where N_e is the number of elements in the cohesive zone. However, the minimum number of elements needed in the cohesive zone is not well established: Falk in (Falk, Needleman, and Rice 2001) used between 2 and 5 elements in their simulations. In the parametric study by (Diehl 2008a), the cohesive over-meshing factor was equal to 5.

7.3.3 Interface strength was not known

In all conditions that the interfacial strength is hard to determine experimentally, it can be treated as a penalty parameter, as illustrated in (Diehl 2008a). For a triangular traction-separation law, the interface strength can be written as a function of fracture toughness (G_c) and the separation failure (δ_f):

$$T_{ult} = \frac{2G_c}{\delta_f} \tag{27}$$

With the fracture energy known, the separation failure may be varied parametrically to obtain values of interface strength to be used in the simulation. Based on the classical fracture mechanics, one recommends that δ_f should be made as small as possible, so the traction-separation law approaches a delta function. This parameter is meshed dependent, and it must be determined by a parametric study for every particular problem, with the initial value set as some fraction of the cohesive element mesh size.
One remembers that the principal role of the cohesive element is to simulate fracture initiation and propagation. The main idea is that the cohesive elements should have infinite stiffness so that they do not affect the overall compliance of the system before the damage initiation criterion is met. However, in the FEM, these elements must have a finite initial stiffness and a sufficiently high value should be chosen such that the overall initial stiffness of the model is not significantly affected by their presence.

7.3.4 Stiffness of the cohesive zone model

Different guidelines have been proposed for selecting the stiffness of the interface. Several researchers have proposed values of the elastic stiffness of interfaces in a composite material system based on experience.
Daudeville in (Daudeville 1999) calculated the stiffness in terms of the thickness and elastic modulus of the interface (about 1e5 N/mm^3). Zou in (Zou et al. 2001), based on their experience, proposed value for the interface stiffness between 10^4 and 10^7 times the value of the interfacial strength per unit length. Camanho (Camanho, Dávila, and Moura 2003) obtained accurate predictions using a value of 10^6 N/mm^3.
Turon et al. (Turon et al. 2007) have proposed the elastic stiffness of the traction-separation law in terms of elastic modulus and the thickness of the region surrounding the interface. Based on Turon formulas, the interface stiffness for mode I can be chosen as:

$$K_n = \frac{\alpha E}{h} \tag{28}$$

where *E* is Young's modulus of the material (CLT), *h* is the thickness of the layer, and the parameter α should be much larger than 1, (Turon et al. 2007) recommend the value of α to be 50. A similar expression can be derived for shear modes (mode II and III):

$$K_s = \frac{\alpha\, G}{h} \tag{29}$$

where *G* is the shear modulus of the material.
Diehl proposed an alternative approach to estimate the elastic stiffness of the cohesive element based on the classical fracture mechanics and numerically stability considerations (Diehl 2008a; Diehl 2008b). He adopted a mimic of the classical Griffith's criterion to define the traction-separation relationship. Thus for a triangular shape the stiffness is defined in terms of fracture energy (G_C), separation at final failure (δ_f) and the damage initiation ratio, defined as δ_0 / δ_f where the δ_0 is the separation at the damage initiation and T_0 is the user-specified initial constitutive thickness of the cohesive element (specified as 1.0), as reported below:

$$K = \frac{2G_C}{\delta_{ratio}\delta_f^2}\, T_0 \tag{30}$$

With both the *equations (27)* and *(30)*, is possible to define the traction-separation relationship based on Diehl formulation, and obtain the initial elastic stiffness of the cohesive element on varying the value of δ_f and δ_{ratio}. Also notes that the *equation (27)* is valid for all three fracture modes, with the appropriate value of fracture energy and separation at failure values.
In the subsequent paragraphs, one uses the Diehl formulation, *equations (27)* and *(30)*, in case that the cohesive strength is unknown. Then, the results will be compared with the outcome of the cases in which the cohesive strength is known. In the last approach will be used the formulations proposed by Turon and other authors, to estimate the stiffness of the cohesive element.

7.4 Viscous regularisation

The viscosity parameter, analogously to (Ardalany, Fragiacomo, and Moss 2015; Sandhaas, Van de Kuilen, and Blass 2012) is introduced for modelling purposes, to improve the convergence characteristics of the model.
It should be noted that was a fictitious viscous parameter which leads to a more stable numerical analysis with fewer convergence problems. The viscous regularisation was a function of the rate of damage variables:

$$d = \frac{(d - d_v)}{\eta} \tag{31}$$

where d is the degradation value, d_v is the stiffness degradation, and η is the viscosity parameter. This parameter is problem dependent, thus the analysis issue is determined an appropriate value of η and brings results closer to the experimental ones. The rule-of-thumb is to choose a smaller value than a larger value because it provides a good match with the experimental data. As observed in (Ardalany, Fragiacomo, and Moss 2015) was needed to perform a study for our specific problem to establish the best magnitude of the viscosity parameter. To this aim, the compression test of CLT panel was modelled changing the value of η from 8e-5 to 1e-3.

Chapter 8
Results

The complete model consists of 91884 elements, with 8-node three-dimensional (C3D8R) timber solid elements. The interface is modelled via a COH3D8, which is an 8-node three-dimensional cohesive element with one stack direction corresponding to the thickness direction of the interface. For the analytical methods discussed in *section 7*, in a FEM with cohesive elements, the value of G_C is a model *input*, and the peak force and relative displacement are a model *output*. As mentioned above, two main different modelling approaches will be presented in the below sections.

8.1 Model performance without interface strength data

In this case, one assumes that only the fracture toughness is known by (Dourado et al. 2008; E. I. Saavedra Flores et al. 2016), equal to 0.1 N/mm.
As suggested by Diehl (Diehl 2008a) one has to choose δ_{ratio} (in the first step equal to 0.1) and parameterize both the interface strength and the stiffness by a single parameter δ_f, namely the separation at ultimate failure.
Then, one systematically has to choose the value of δ_f as a fraction of the cohesive element size and obtain the interface strength and stiffness using *equations (27)* and *(30)* respectively. One considers five cases by taking different fractions of cohesive element length for the parameter δ_f. In each case, viscous regularisation parameter equal to 1e-3 is used to aid in the convergence process, ***Table 6***.

Case ID	***Cohesive element length, (l_e)***	***Fraction, f***	***$\delta_f = f\ l_e$***	***Interface strength, t [MPa]***	***Interface stiffness, K [N/mm^3]***
I	8	0.1%	0.008	25	31250
II	8	0.2%	0.016	12.5	7812.5
III	8	0.3%	0.024	8.4	1157
IV	8	0.4%	0.032	9.3	976
V	8	1%	0.08	2.5	312.5

Table 6: cases considered for simulation for cohesive elements.

The results are presented in ***Figure 8.1***, where load-displacement curves from the simulations are compared against the experimental solution. For cases III (0.3%), IV (0.4%) and V (1%) the nonlinear procedure failed to converge at the initiation of the fracture process and the peak force predicted was very low. These cases are unlikely to yield accurate results when compared with the experimental data. Case II (0.2%) gives good results when compared with the experimental data, with a better match. For the case I (0.1%) the peak force reached was about of 31% higher than the average value of pick force in the experiments. Note from ***Table 6*** that the interface strength used for all cases, except the Case V, differs from the true interface strength (equal to 2.71 MPa, used for the case in which the interface strength is known, in *section 8.2*), yet good results are obtained in case II. It should also be noted by the case II, that the significant increase in the interface strength (12.5 MPa vs. 2.71 MPa), leads to a peak load related to the initial failure of material quite accurately. This implies that the interface strength as penalty parameter leads to a good approximation of the behaviour of the material.

However, it worth to noting that the penalty value of interface strength is very close to the estimated value from the experimental data about the shear strength of the internal layers of CLT element, equal to 16.20 MPa (***Table 4***) and to the strength value reported in literature, equal to 12.80 MPa. The first comparison between experimental data and numerical results highlights the advantages of the penalty CZM approach, which allows identifying of the overall mechanism of failure.

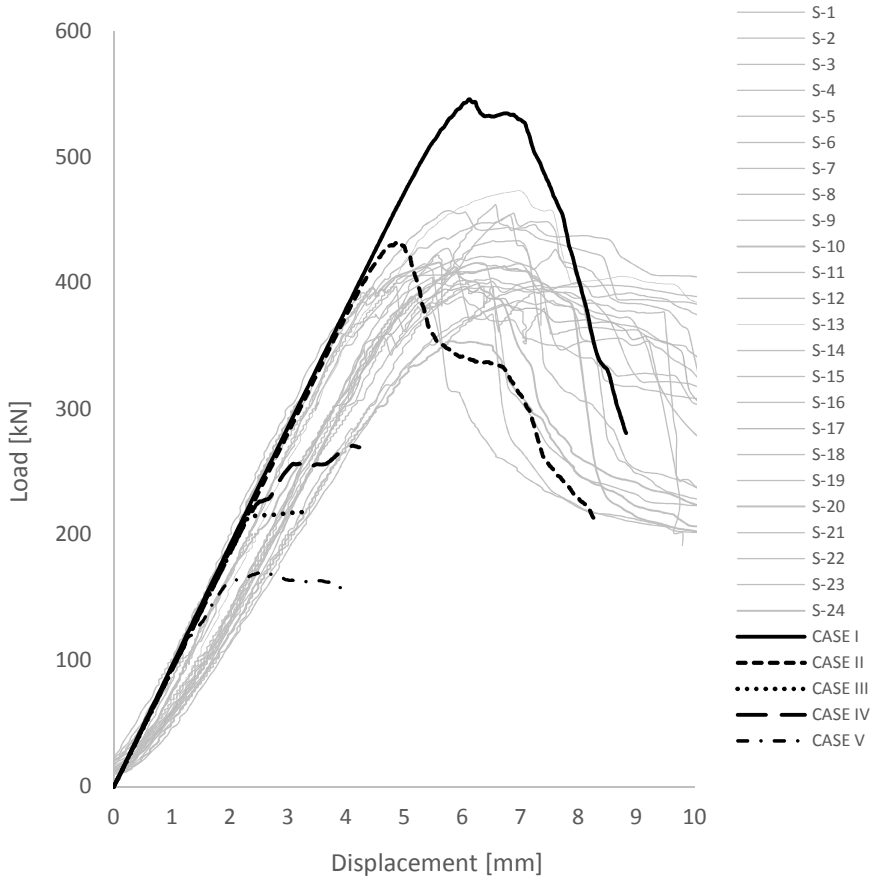

Figure 8.1: load-displacement curves on varying of the ductility in the cohesive element.

Below, ***Figure 8.2*** shows the failure of wooden specimens at the end of the test, to a maximum displacement reached. It should be noted that the result of the simulation is very close to the specimen failure. Thus confirms that the Diehl's formulation, and then the penalty framework for cohesive elements, can capture and describe the failure of the CLT panel.
In ***Figure 8.3*** the numerical model is shown for the case II, in correspondence to different load from the peak load, about of 431 kN to the final load about of 210 kN.

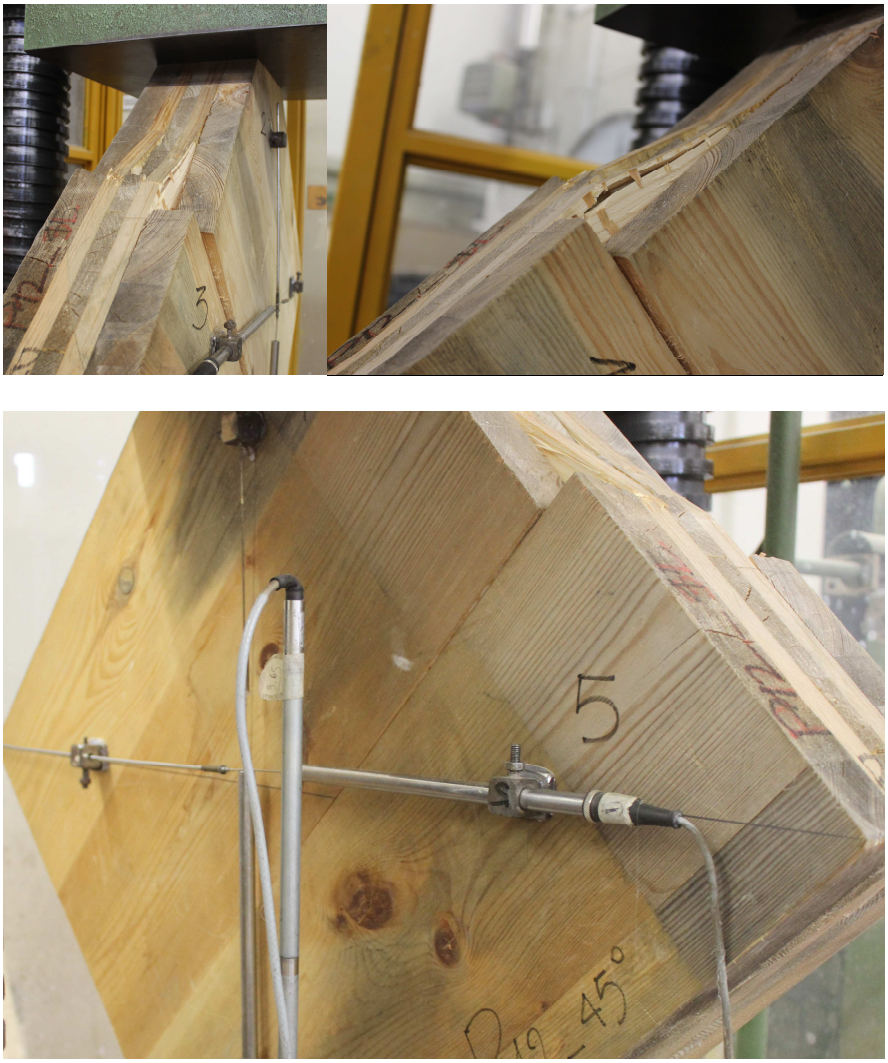

Figure 8.2: *specimens S-12, failure at the end of the test, failure load equal to 452.70 kN.*

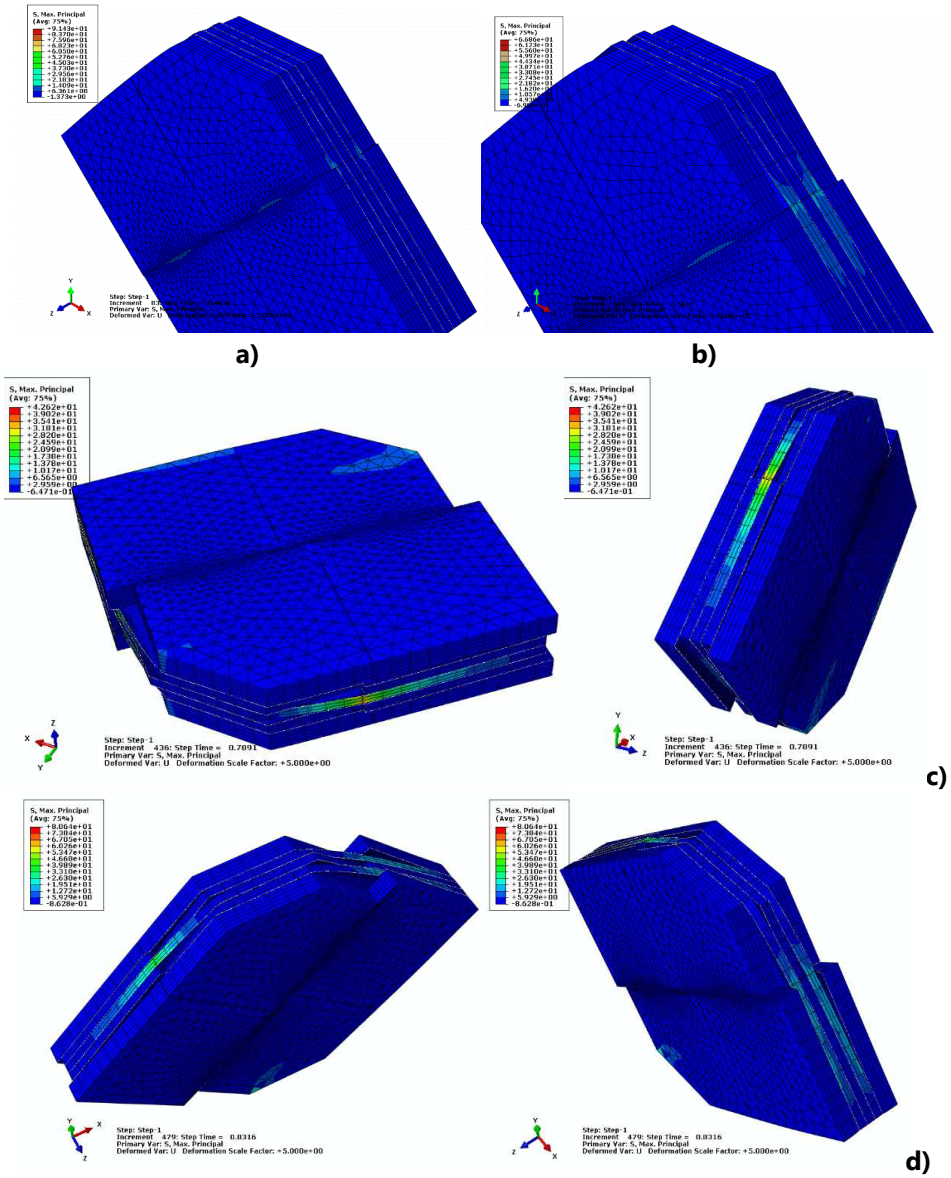

Figure 8.3: finite element model for case II from maximum load reached in the simulation equal to 431 kN (a); at load equal to 363 kN (b); at load 234 kN (c) and at final load equal to 210 kN (d).Legend: MPa.

Of course is very important to study and assess the effect at varying of each parameter, which is considered in the *equations (27)* and *(30)*.

In order to illustrate how the components may affect the value of the overall failure behaviour of the specimen, in the following section, one considers different values of δ_{ratio}, defined as the damage initiation ratio, the viscous regularisation, and different cases to describe the friction surface.

In ***Figure 8.4***, are reported the force-displacement curves with the different hypothesis of the viscous regularisation, considering the same parameters for

both strength and stiffness of case II reported in ***Table 6***, that shown the better match with the experimental curves.

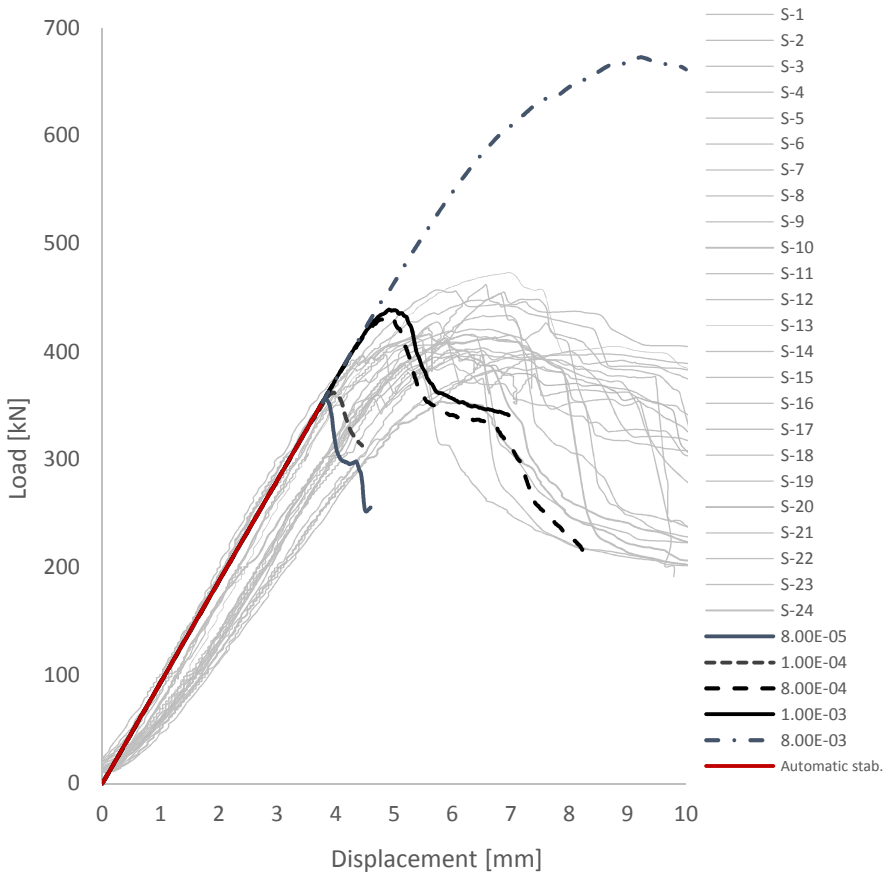

Figure 8.4: load-displacement curves on varying of the viscous parameters.

The previously discussed viscous parameters (*section 7.4*) are applied with the aim to evaluate the interaction of this parameter in the solution of the numerical simulation. Several orders of magnitude of η are considered in the modelling, and the load-displacement curves for different η values are derived and are compared with the experimental results.

The comparison shows that for η = 0.008 the predicted load is considerably higher than the experimental value (+62%), whereas for η = 0.0008 and 0.001 the prediction of the final load is closer to the experimental results. In particular, the value of 0.001 brought the best results in the analytical solution, with a small difference in the case η = 0.0008. In the cases where η = 0.00008 and 0.0001, the curves shown lower peak than the experimental value, about of -14% and -12%, respectively. As can be seen in, ***Figure 8.4***, once the viscous regularisation factor is sufficiently small (0.0008 or 0.001) it improves convergence of the FEM, and

provide results that are closer to the experimental data. From a certain order of magnitude (> 0.008) it leads to inaccurate results.
Abaqus™ also provides a different mechanism for the stabilisation of the analysis, namely the automatic stabilisation method. One big difference between the viscous regularisation of the cohesive zone and the automatic stabilisation is that the first technique is applied on an element set, whereas the second one is being implemented to the whole model. By using an automatic stabilisation factors, the software ensures that the ratio of the stabilisation energy over the total strain energy does not exceed a user chosen accuracy tolerance; ***Figure 8.4*** also shows the load-displacement curve for the automatic stabilisation method. The highest value for the calculation times is obtained for the automatic stabilisation method, because, as expected, the factor is applied to the entire model whereas by using the viscous regularisation method, the stabilisation factor is only applied to the select element set. Furthermore, for this given model using the automatic stabilisation, the simulation is not able to predict the softening behaviour and fails to converge before the peak load was reached.
Another important variable under evaluation concerns the behaviour of the friction surface. Below, ***Table 7*** reports four different cases used in the simulation for the friction coefficient. Also, in this case, one considers the values of strength and stiffness reported in ***Table 6***, which refer to case II, to define the cohesive element behaviour.

Case ID	***Friction coeff.***
I	0.2
II	0.3
III	0.4
IV	0.5

Table 7: cases considered for simulation for the friction surface.

The range of the frictional coefficient was choose on the basis of the literature review (Blau 2001). With reference to ***Table 7***, one uses the different value of friction from 0.2 to 0.5. Below, in ***Figure 8.5***, the four cases are compared and shows that the friction coefficient does not significantly influence the behavior of the panel. Thus for each analysis the friction coefficient is choose equal to the average value of 0.4.

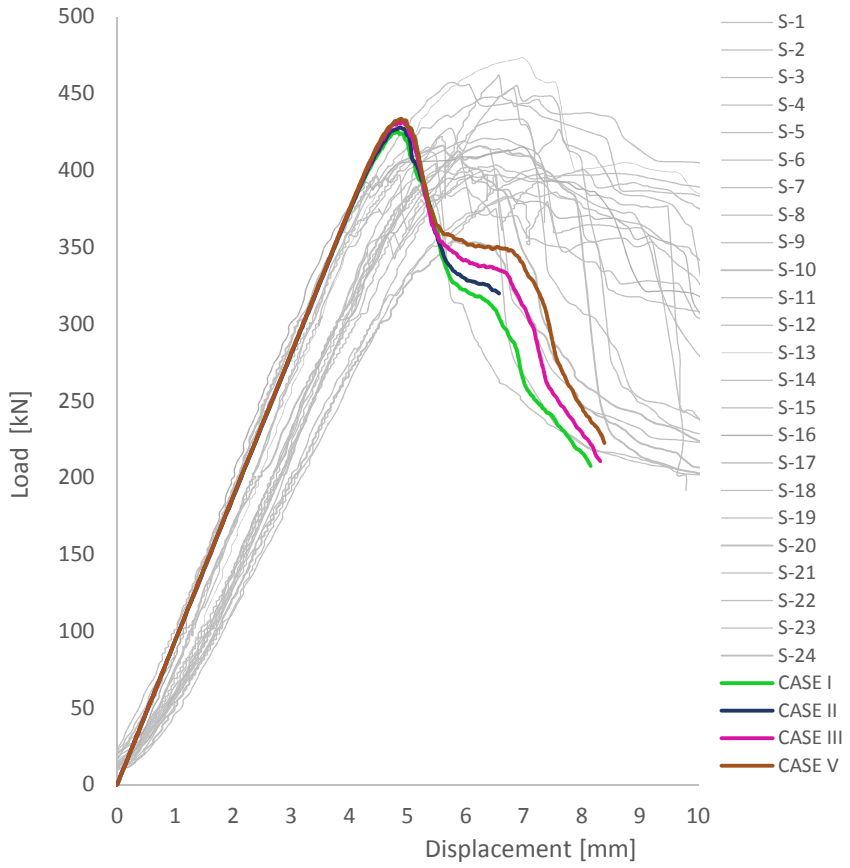

***Figure 8.5*:** load-displacement curves on varying of the friction coefficient.

When the friction coefficient and the viscous stabilisation are defined, one considers the impact of the meshing in the numerical model. Two main cases are considered: the first one coupling the meshes of solid elements of 20 mm with the mesh size of 6 mm to cohesive elements and the second one coupling the solid meshes of 34 mm with cohesive meshes of 8 mm cases. The cases are reported in ***Table 8***. For each case the ratio 4:1 is respected. The third is used to compare the previous cases, with the aim to demonstrate that finer meshes applied also to the friction surface are able to provide with more accuracy the panel behaviour.

Case ID	***Solid element (Timber boards)***	***Cohesive element (adhesive interfaces)***	***Friction surface***
I	20	6	20
II	32	8	32
III	32	8	8

Table 8: different meshing considered in the simulation.

In Case I and II, reported in ***Table 8***, one selects the coarser meshes, 20 mm and 32mm respectively, to apply at the friction surface. In the third case a finer meshes, equal to 8 mm, are applied also in the friction surface.
For a better estimation of the influence of mesh size both in the convergence of the finite element model and also in the Diehl's formulation, which are strongly related to mesh size, one characterise each case with different value of δ_f (fraction of the cohesive element size) and obtain the interface strength and stiffness using *equations (27)* and *(30)* respectively. In ***Figure 8.6***, is possible to see the different law of each case reported in ***Table 8***, with different value of δ_f used.

The associated load-displacement curves show a high value of resistance both in the Case I and II, which are not faithful to the experimental behaviour of the panels. In the third case, where the finer meshes are used also on the frictional surface, in particular, the same length of the cohesive element, equal to 6 and 8 mm, the better fitting is showed. The result of using a lower mesh size (6 or 8 mm than 24 or 32 mm) is that the number of elements in the friction surface increase. Therefore, as in the cohesive element, the representation of the softening response of the fracture process is more accurate. When the cohesive and the friction zones are discretized by too few elements, the distribution of stress in not represented accurately. Thus, a minimum number of elements is needed to get successful FEM results.

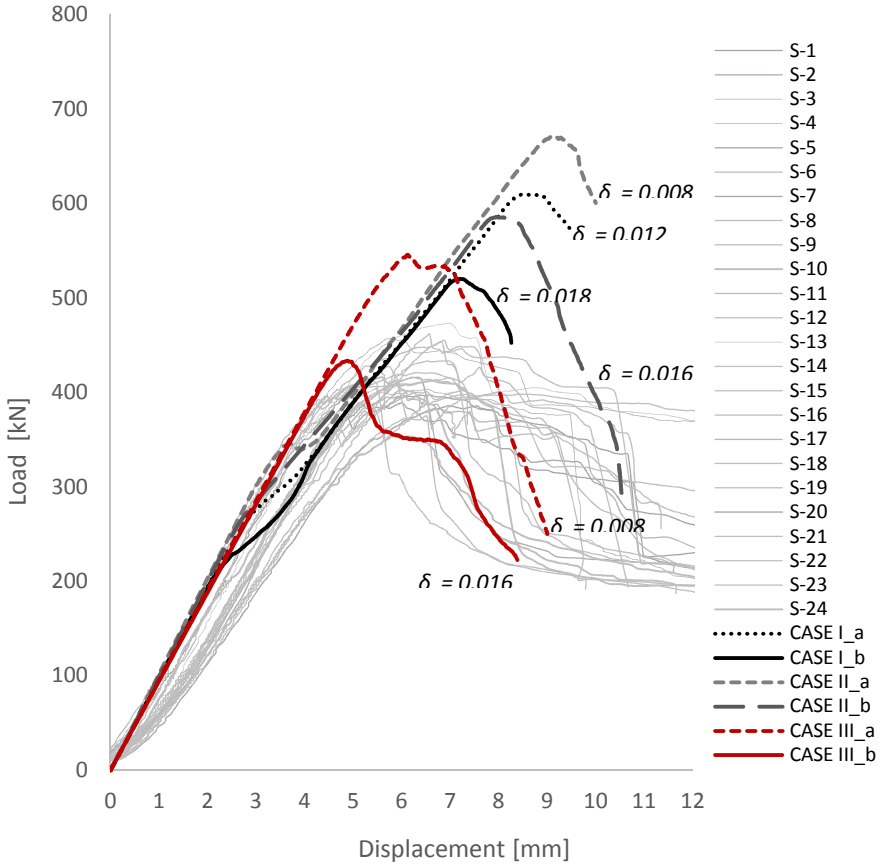

Figure 8.6: load-displacement curves on varying of the ductility in the cohesive elements to different mesh size.

The following figures show the damage evolution for the case I and II at a different load increment of the simulation. The Figures from 8.7 to 8.11, related to the cases I_a and II_a, show how the first cracks between the layers take place for a very low load step (about of 276 kN and about of 335 kN, respectively). A higher equivalent displacement than the recorded value in the experimental tests (***Figure 8.6***), with a decrease in stiffness and a subsequent increase of carrying capacity, is shown in both curves. In general, the load-displacement curves show an inaccurate failure evolution, which is not well comparable with the experimental data. The load-displacement curve evolution is the same if one considers the cases I_b and II_b.

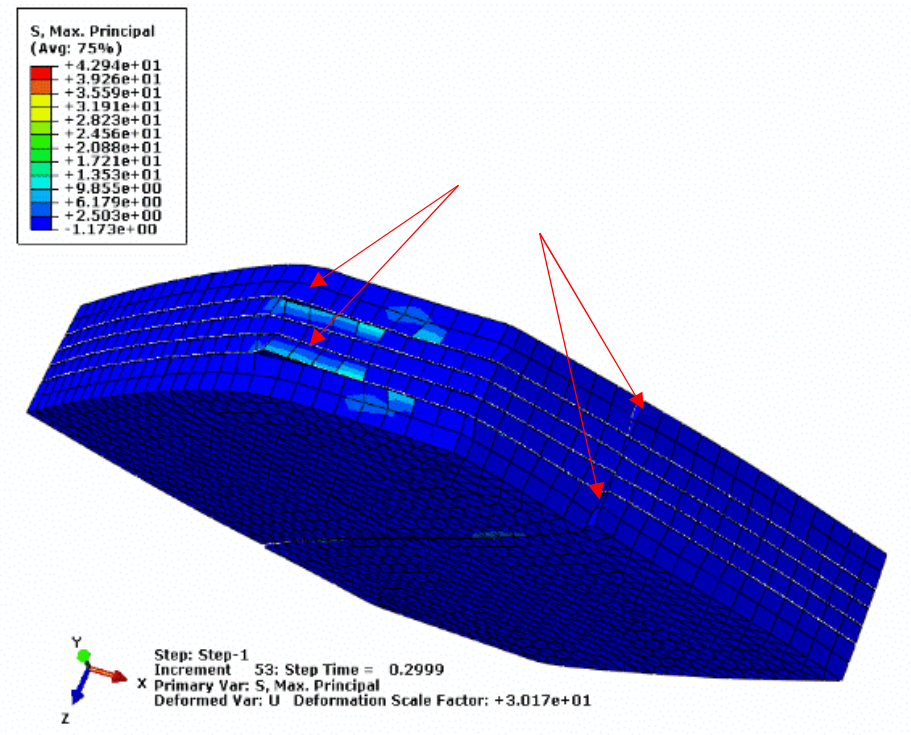

Figure 8.7*:* finite element model for the *CASE I_a* at the first sliding of the layers at the displacement increment about of 3mm (276 kN). Legend: MPa.

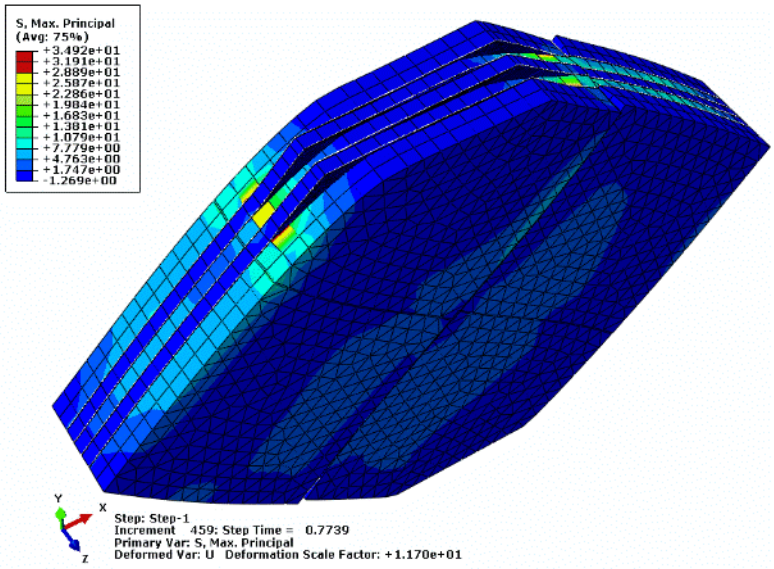

Figure 8.8**:** finite element model for the *CASE I_a* at the load reached about of 569 kN and applied displacement equal to 7.7 mm. Legend: MPa.

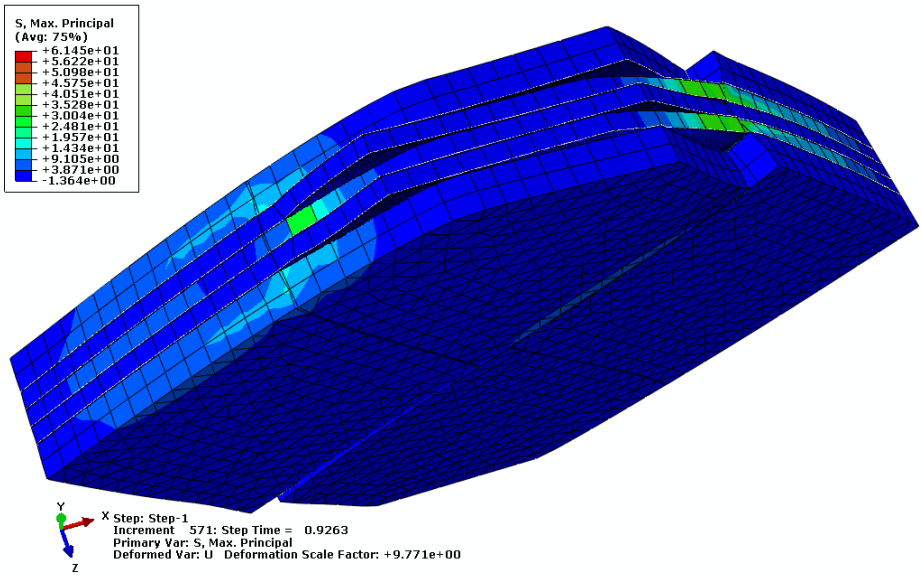

Figure 8.9: finite element model for the *CASE I_a* at the reached load about of 587 kN and applied displacement equal to 9.2 mm. Legend: MPa.

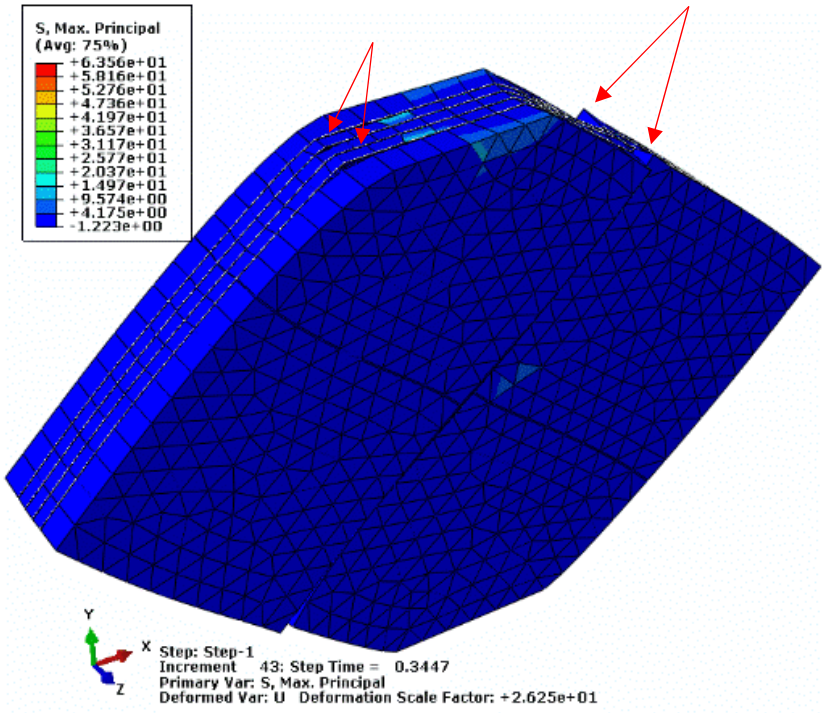

Figure 8.10: finite element model for the *CASE II_a* at the first sliding of the layers at the reached load about of 335 kN and applied displacement equal to 3.4 mm. Legend: MPa.

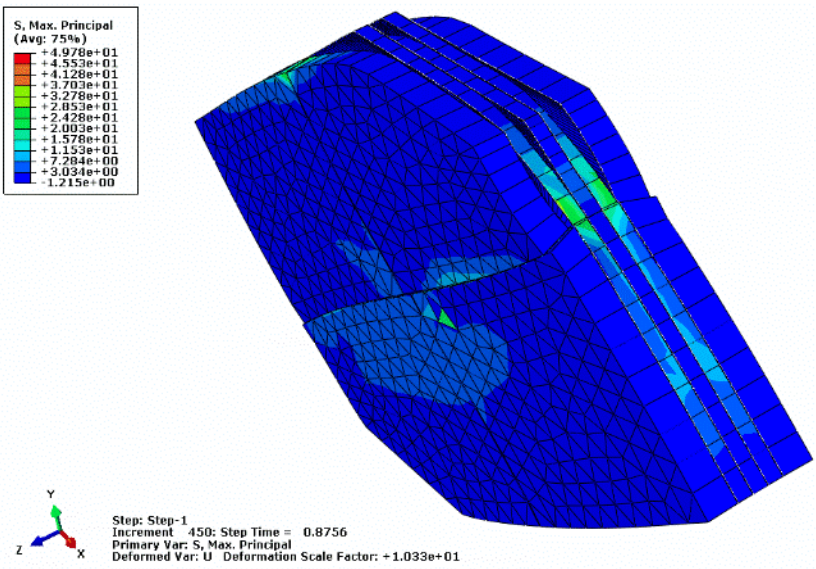

Figure 8.11: finite element model for the *CASE II_a* at the maximum load reached about of 657 kN and applied displacement equal to 8.7 mm. Legend: MPa.

Contrary to the previous cases, the simulation corresponding to cases III exhibits a linear law until 545 kN (case III_a) and 430 kN (case III_b), in which the peak load is reached, and the damage begins, as shown in ***Figure 8.12***. The subsequent damage evolution is well depicted by the softening law, which characterises the load-displacement curve in the case III and illustrated in ***Figure 8.10*** at increment number 282.

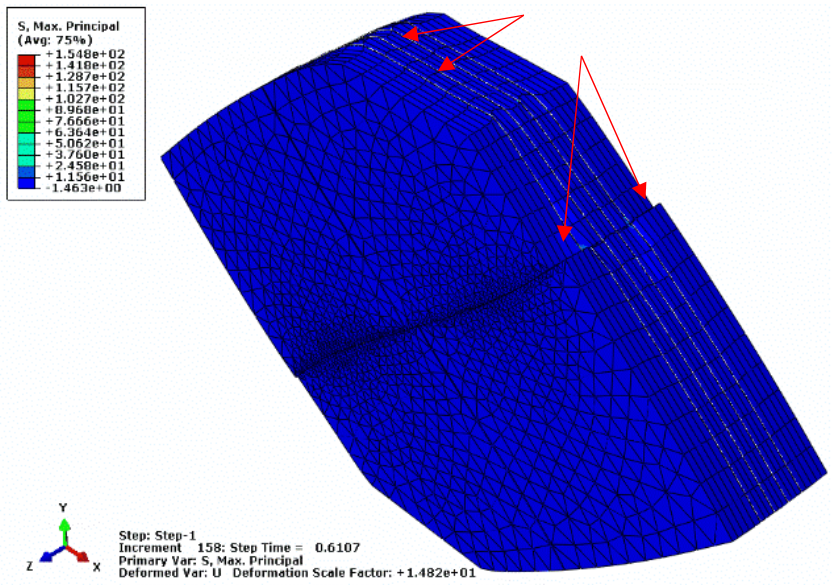

Figure 8.12: finite element model for *CASE III_a* at the maximum load reached about of 545 kN and applied displacement equal to 6.1 mm. Legend: MPa.

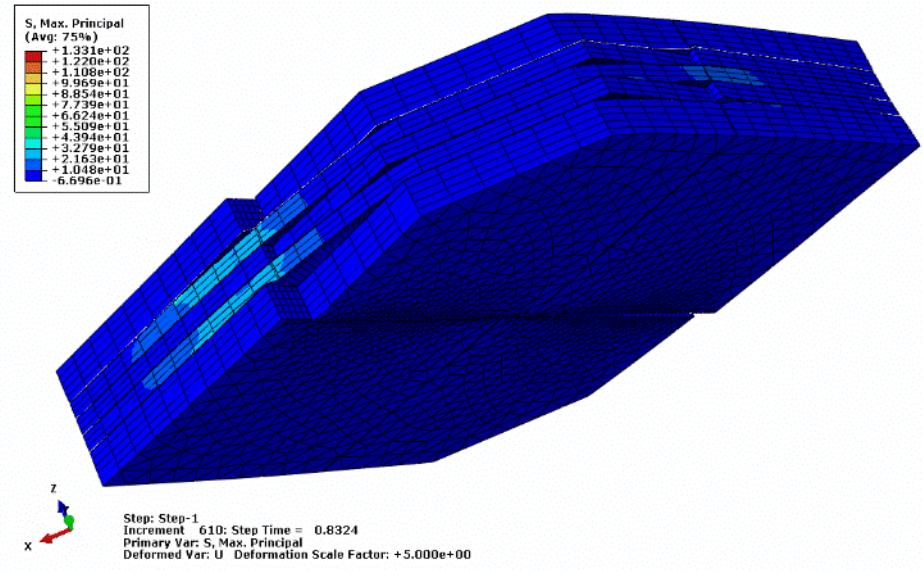

***Figure 8.13*:** finite element model for *CASE III_a* at the reached load about of 343 kN and applied displacement equal to 8.3 mm. Legend: MPa.

In general, accurate results are obtained over a range of meshes and penalty parameters. The mesh-relative cohesive ductility ratio is the best measure of assessing the apparent level of the cohesive ductility penalty. When this ratio is too low, the relative ductility of the bond becomes too low, and the solution

quality will degrade significantly because the mesh cannot resolve the compliance gradients sufficiently. Increasing this ratio improves the solution.
The last observations are about the damage initiation ratio, which plays a significant role in the determination of the cohesive stiffness, see *equation (30)*. The different values of δ_{ratio} used in the simulations can be found in ***Table 9***.

Case ID	δ_{ratio}	δ_f	***Cohesive element stiffness, K [N/mm³]***	***Cohesive element strength [MPa]***
I	0.1	0.1%	31250	25
II	0.3		10500	
III	0.4		7812.5	
IV	0.1	0.2%	7812.5	12
V	0.3		2600	

Table 9: *values of δ_{ratio} considered in the simulation for the cohesive element.*

For case with δ_f equal to 0.1% of the mesh size, the strength value is kept equal to 25 MPa; while for δ_f equal to 0.2% of the mesh size, the strength value is kept equal to 12.5 MPa (see ***Table 6***). The numerical predictions and the experimental data for all test cases simulated are shown in ***Figure 8.14***. A comparison of the results indicates a good correlation between the experimental results and the predicted maximum load in the case III and IV with an interface stiffness equal to 7812.5 N7mm^3. Also, the post-peak behaviour is well simulated in accordance with the damage evolution of the specimens and with the decreasing of the load than the increase of displacement, especially in case IV. The load-displacement curves demonstrated that the model accuracy is relatively insensitive to the selection of the damage initiation ratio. Close inspection of ***Figure 8.14*** shows that as δ_{ratio} is decreased, making *K* stiffer, the model initially behaves stiffer but ultimately curves back, before crack growth, to the same result regardless of the value of δ_{ratio}.

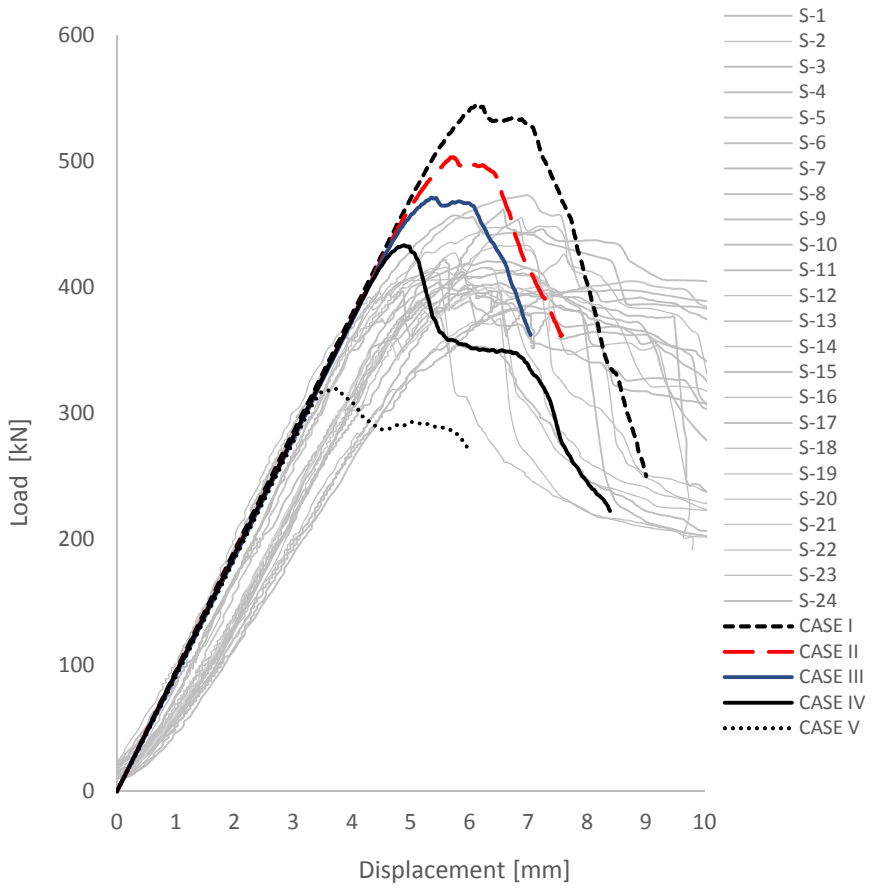

Figure 8.14: load-displacement curves on varying of the *damage initiation ratio*.

The largest difference than the maximum load obtained with the experimental data, +32%, corresponds to the cases I. This difference is due to the higher values of the cohesive stiffness (31500 N/mm^3) that keeps the layers together, and the detachment arises too late with consequent overestimation of the peak load. However, all cases can capture the shape of the softening law. In particular, the cases I and IV have a good law compared with the experimental data, until the maximum displacement of about 9 mm that corresponds to a full failure of the cohesive layers. Values of the damage initiation ratio greater than the value used in case IV (equal if compared with the *case II*), coupled with a lower cohesive resistance (12 MPa), implies that the stiffness of the cohesive layers decreases significantly (2600 N/mm^3) and the peak load in *case V* differs from the experimental data of about -23%. In this case, the load-displacement curve is not proper to a description of the CLT failure mechanism.

8.2 Model performance with adhesive strength data

One assumes that the interfacial strength is known from the literature or from direct experimentation (*section 8.2.1*). To simulate the problem, one has to choose a suitable mesh for the wood components as well as the interface. The size of the wooden layers can be estimated based on compressive consideration only, without considering fracture initiation or propagation. Thus, a mesh with 10589 solid elements was found to give a suitable compressive response. To estimate the size of the cohesive elements, one adopts two strategies. In the first step, a rule-of-thumb approach is used to define a finer mesh, which suggests from 3 to 5 cohesive elements for each adjoining structural element. One has to choose an over-meshing ratio of 4:1 giving the length of the cohesive element as 8 mm. The alternative approach for choosing the size of the cohesive element was used in the second step, to confirm and assess the size of the cohesive elements in the mesh. From the *equations (25)* and *(26)*, one calculates the length of the cohesive zone and the equivalent mesh size. A summary of different models commonly used in literature and the equivalent parameter *M* for plane stress are shown in ***Table 9***.

	l_{cz} ***(Eq.25)***	***M***	l_e ***(Eq.26)***
Hui et al.	27.16	0.21	6.8
Irwin	40.10	0.31	10.0
Dugdale and Barenblatt	51.74	0.40	13.0
Rice, Falk et al.	113.83	0.88	28.5
Hillerborg et al.	129.36	1.00	32.3

Table 10: length of the cohesive zone (l_{cz}) and equivalent mesh size (l_e) at varying of the parameter M.

Hui and Irwin's models give the closer values than the mesh size used in the analysis described in this work, equal to 8 mm for a cohesive element. Dugdale and Barenblatt, Rice and Falk, and Hillerborg give the higher mesh size, which is closer to the mesh size of the adjoining element. Therefore, the rule-of-thumb and the process zone-based considerations, lead to the same range of cohesive element length and equivalent mesh size. The higher value corresponds to Hillerborg's model, supports the dimension of mesh chosen to describe the wooden layers, equal to 32 mm.

The initial stiffness of the cohesive element is estimated using the Turon's equations, and those used by other authors. The results are shown in ***Table 10***. In each case, the CLT material's elastic modulus is equal to 11000 MPa, the CLT shear modulus ranges from 100 MPa equal to rolling shear modulus to 450 MPa equal to shear modulus for CLT without narrow face bonding or with cracks or checks (Brandner et al. 2016; Bogensperger, Moosbrugger, and Silly 2010). The

nominal interfacial strength is equal to 2.71 MPa in the normal direction (*section 8.2.1*), and equal to 16.2 MPa and 6.5 MPa in the tangential direction (***Table 6***). Finally, α is taken as 50.

t [mm]	***Daudeville et al.***	***Zou et al.***	***Turon et al.***		
			ID	***K_n***	***K_s***
20	-	$2.7x10^4$	I	27500	875
			II	27500	250
			III	27500	1125
			IV	27500	1e4
0.2	$8.4x10^4$	-		-	

Table 11: interface stiffness *K* proposed by different authors (N/mm^3).

Turon's formulation gives the normal interface stiffness (K_n) equal to 27500 N/mm^3 for a layer thickness of 20 mm, and a range of the tangential interface stiffness (K_s) between 250 N/mm^3 and 1125 N/mm^3. These values are close to the normal interface stiffness values obtained from Zou's guidelines (between 10^4 and 10^7 times the value of the interfacial strength) if the lower value is considered. The interface stiffness obtained from the Daudeville et al. is very high, since they consider a lower thickness equal to the adhesive layer, of about 0.2 mm. The simulations were performed by specifying the various values of interface stiffness, ***Table 11***, in order to investigate the effect of the stiffness on the numerical results. The results are presented in ***Figure 8.15***, against the experimental solutions. The load-displacement response curves obtained from simulations using a high interface stiffness (Daudeville et al. and Zou et al.), are greater than experimental curves. However, smaller values of the interface stiffness have a strong influence on the load-displacement curves, since a stiff connection between the neighbouring layers is not assured. The normal and tangential stiffness that results from Turon's equations with E equal to 11000 MPa, and G equal to 350 MPa (case I) and to 100 MPa (case II) are the reasons to a lower stiffness and load showed by the curves. The same behaviour characterise both case III_a and III_b, calculated with the shear modulus equal to 450 MPa and with different strength of interface, based on ***Table 6***. The case IV shows the best match with the experimental curves since the tangential stiffness of interface is increased to 1e4 MPa.

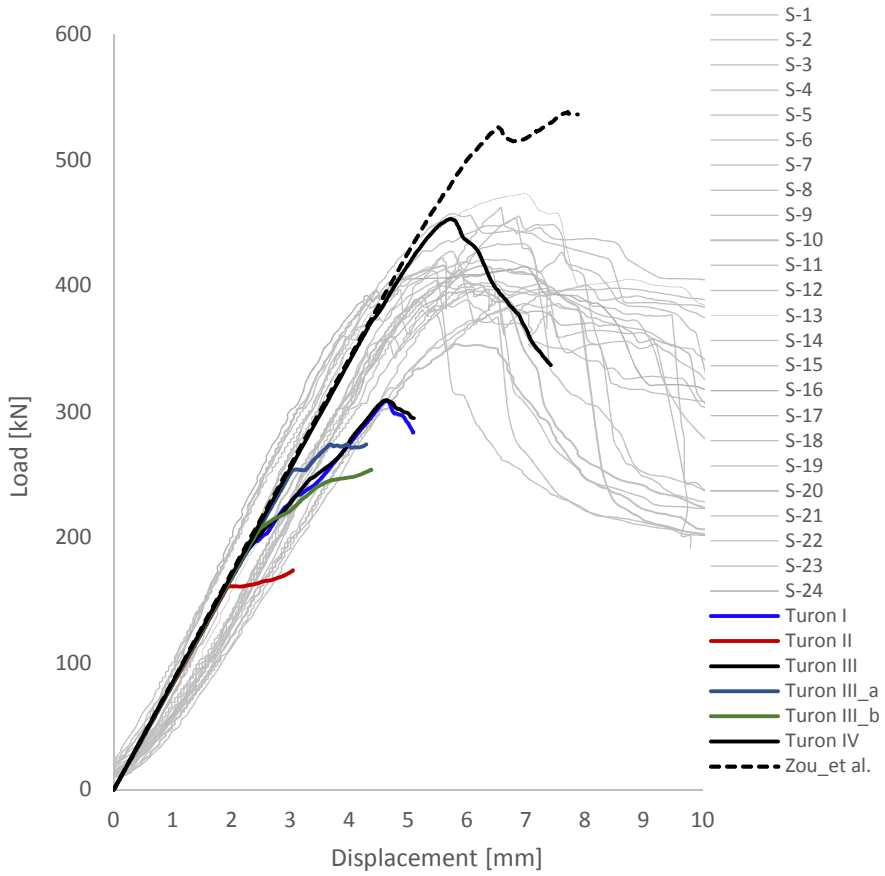

***Figure 8.15*:** load-displacement curves obtained with different interface stiffness.

It is worth noting that the most influential role in the overall behaviour of the panel is played by the tangential stiffness (k_s). Furthermore, the comparison of Turon's formulation with results obtained from Diehl's equations shows that the best fit of the experimental curves is for the same magnitude of interface stiffness. ***Figure 8.16*** shows the damage evolution with stiffness value proposed by Zou et al. This model clearly show the influence of the higher stiffness in the damage evolution of the cohesive element. The friction surface start to fail to applied load equal to 461 kN, while the cohesive elements between the wooden layers keep them together without damage (**Figure 8.16**).

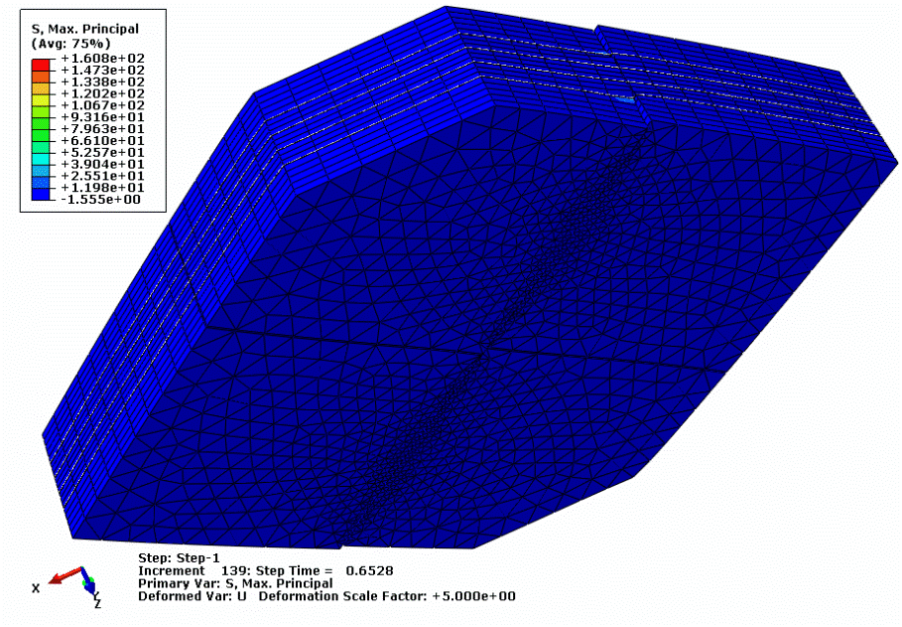
S, Max. Principal
(Avg: 75%)
+1.608e+02
+1.473e+02
+1.338e+02
+1.202e+02
+1.067e+02
+9.316e+01
+7.963e+01
+6.610e+01
+5.257e+01
+3.904e+01
+2.551e+01
+1.198e+01
-1.555e+00
Step: Step-1
Increment 139: Step Time = 0.6528
Primary Var: S, Max. Principal
Deformed Var: U Deformation Scale Factor: +5.000e+00

a)

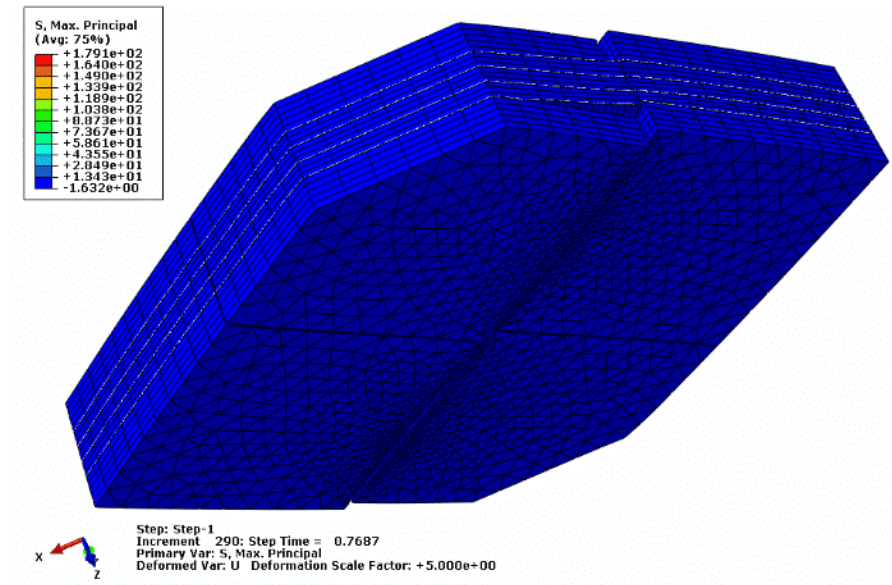
S, Max. Principal
(Avg: 75%)
+1.791e+02
+1.640e+02
+1.490e+02
+1.339e+02
+1.189e+02
+1.038e+02
+8.873e+01
+7.367e+01
+5.861e+01
+4.355e+01
+2.849e+01
+1.343e+01
-1.632e+00
Step: Step-1
Increment 290: Step Time = 0.7687
Primary Var: S, Max. Principal
Deformed Var: U Deformation Scale Factor: +5.000e+00

b)

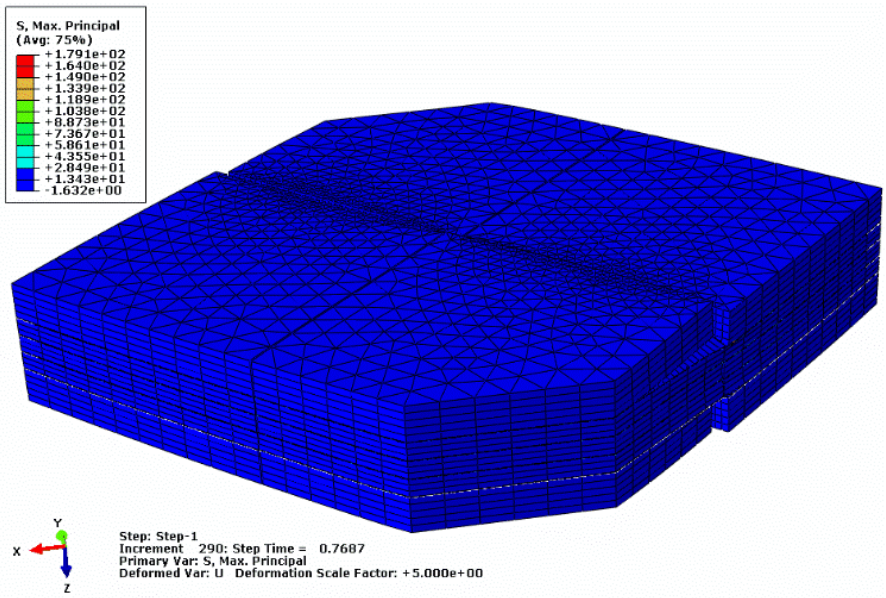

c)

Figure 8.16: *progressive damage evolution in Zou et al. model: a) reached load equal to 526 kN corresponds to the failure of the friction surface at displacement 6.5 mm; b)and c)reached load 537 kN (maximum load reached in the simulation)* and applied displacement equal to 7.7 mm. Legend: MPa.

By comparison of the above ***Figure 8.16*** with the below from ***Figures 8.17*** *to* ***8.20*** which show the simulation with stiffness value from Diehl's formulation and Turon's simulation respectively, is evident how the damage evolution in the CLT panel is perfectly reproduced .

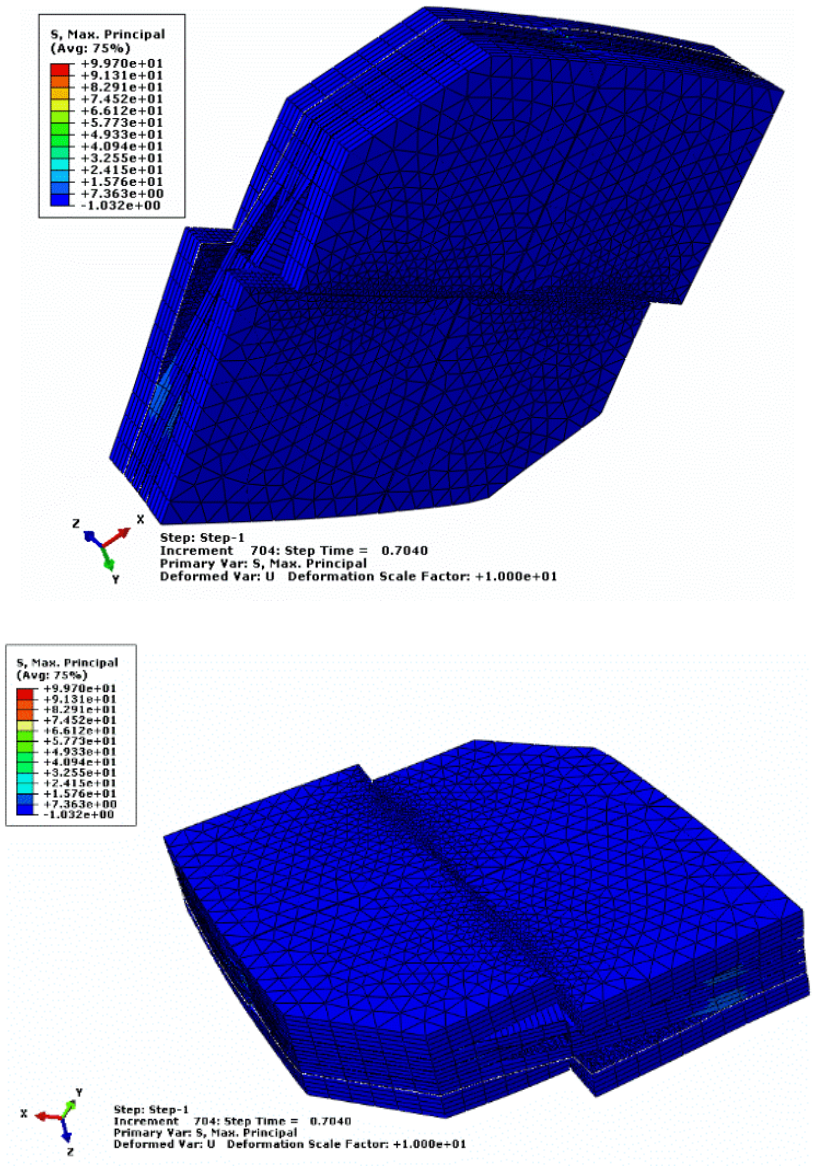

Figure 8.17: *failure of the CLT element with stiffness value from Diehl's formulation: case I at maximum displacement equal to 7 mm that corresponds at load 362 kN.* Legend: MPa.

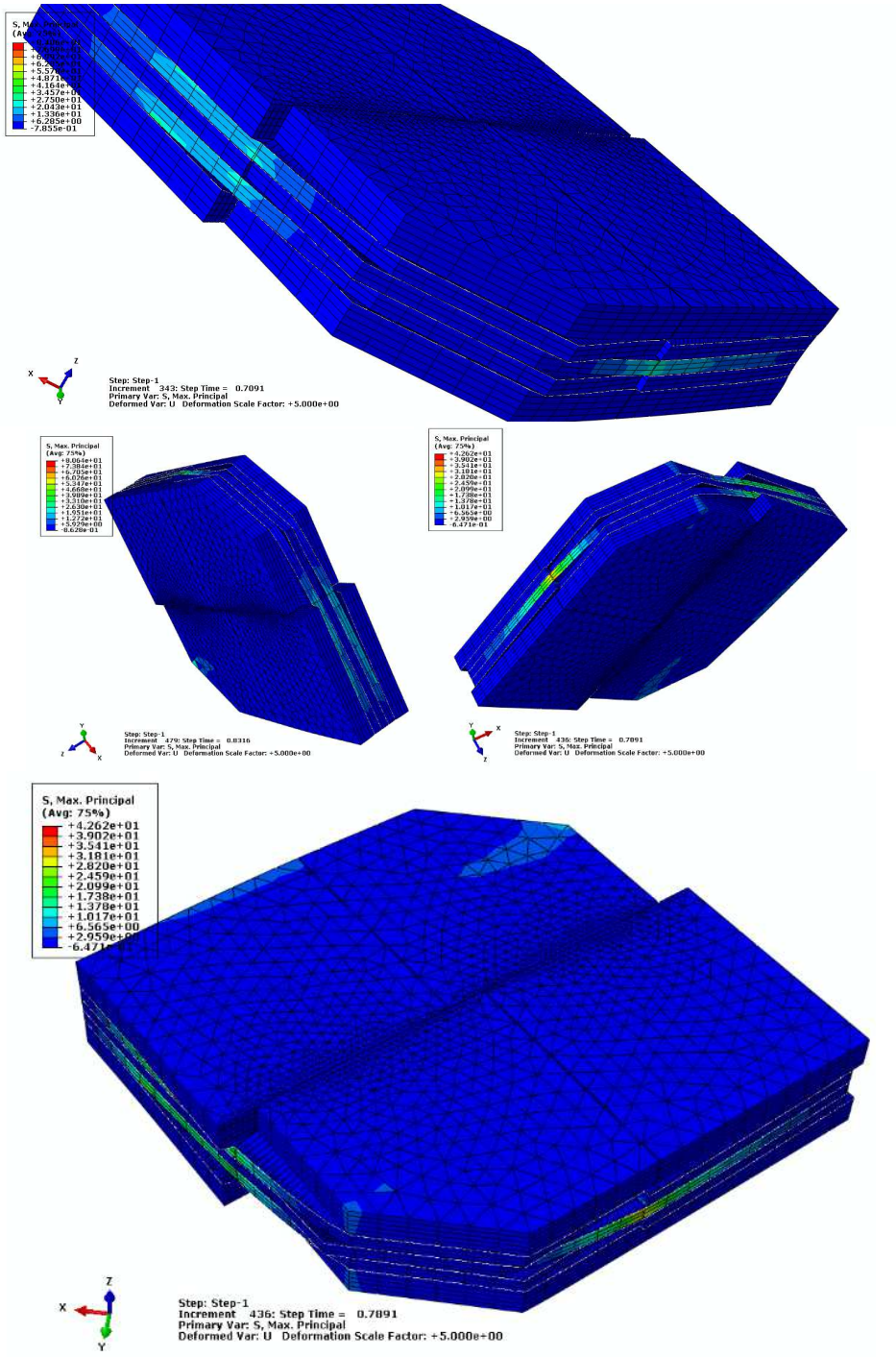

Figure 8.18: *failure of the CLT element with stiffness value from Diehl's formulation: case II at maximum displacement about 8 mm that corresponds at load 234 kN*. Legend: MPa.

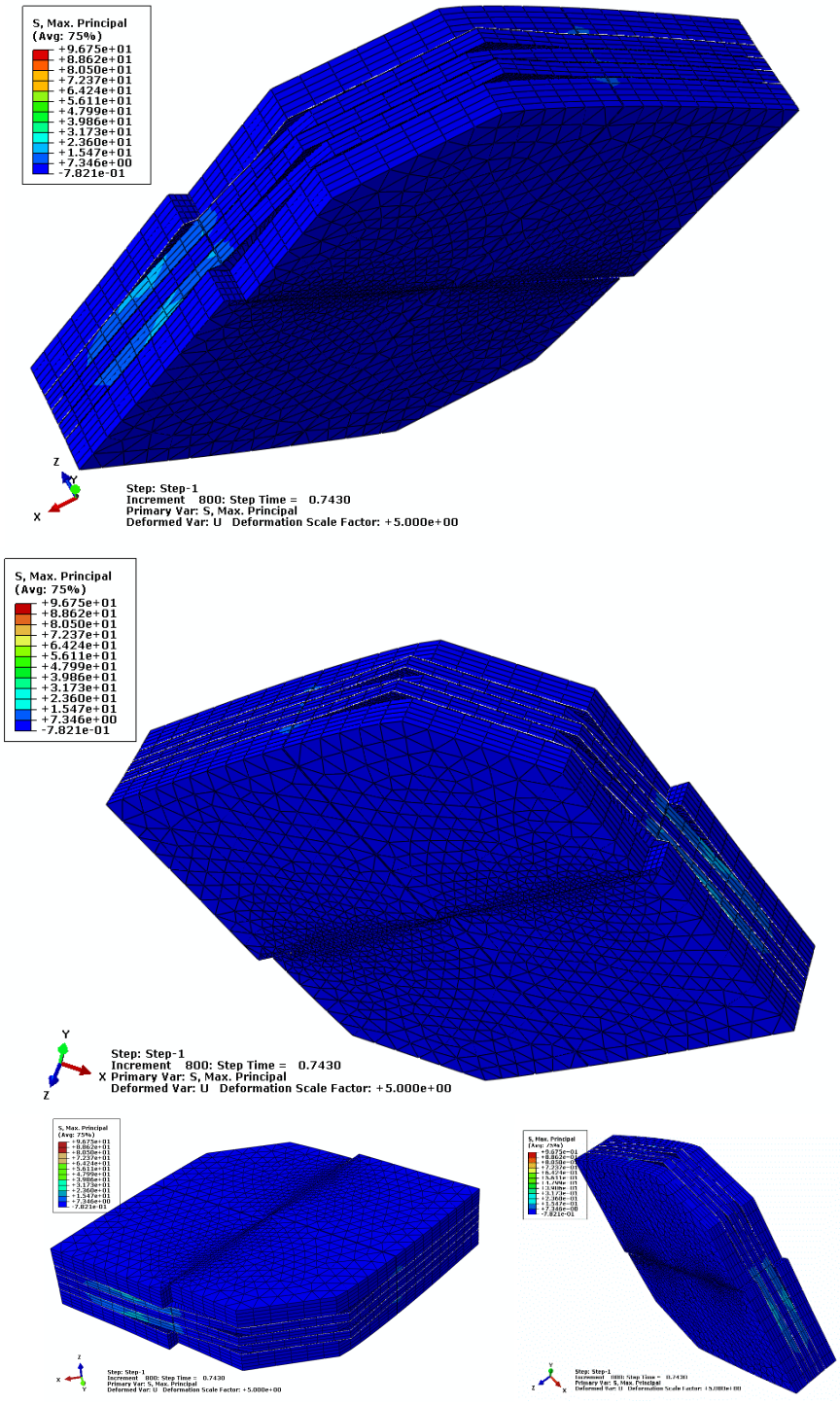

***Figure 8.19**: failure of the CLT element with stiffness value from Turon's formulation, case IV, at maximum displacement about 7.4 that corresponds at load 336 kN.* Legend: MPa.

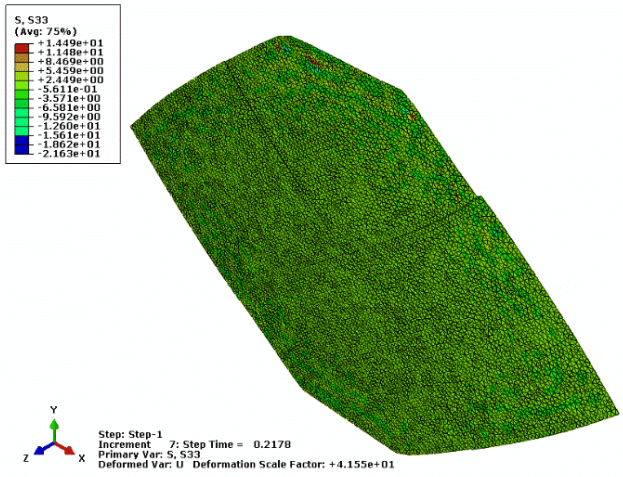
S, S33
(Avg: 75%)
+1.449e+01
+1.148e+01
+8.469e+00
+5.459e+00
+2.449e+00
-5.611e-01
-3.571e+00
-6.581e+00
-9.592e+00
-1.260e+01
-1.561e+01
-1.862e+01
-2.163e+01
Y
Z
X
Step: Step-1
Increment 7: Step Time = 0.2178
Primary Var: S, S33
Deformed Var: U Deformation Scale Factor: +4.155e+01

a)

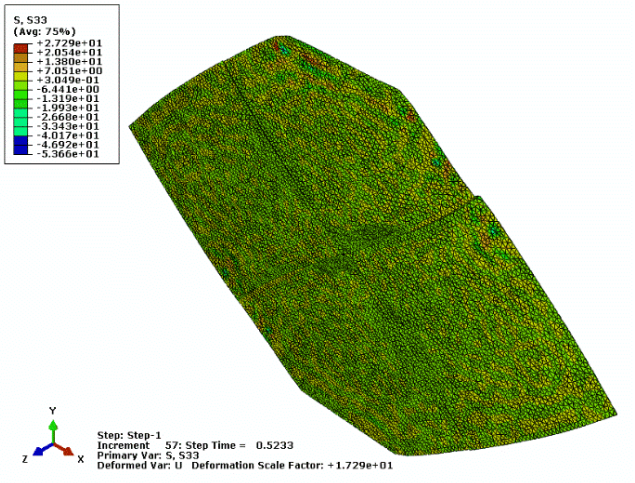
S, S33
(Avg: 75%)
+2.729e+01
+2.054e+01
+1.380e+01
+7.051e+00
+3.049e-01
-6.441e+00
-1.319e+01
-1.993e+01
-2.668e+01
-3.343e+01
-4.017e+01
-4.692e+01
-5.366e+01
Y
Z
X
Step: Step-1
Increment 57: Step Time = 0.5233
Primary Var: S, S33
Deformed Var: U Deformation Scale Factor: +1.729e+01

b)

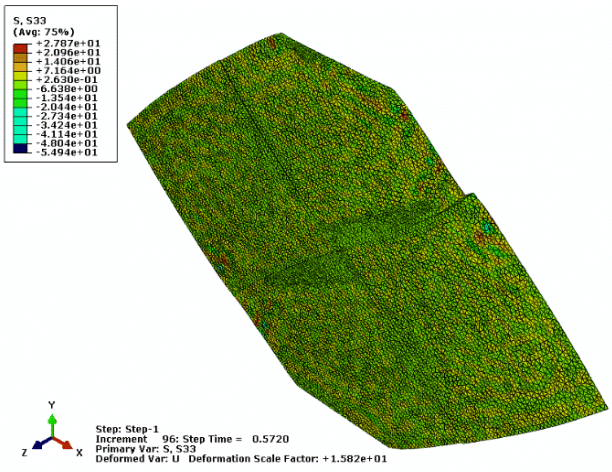
S, S33
(Avg: 75%)
+2.787e+01
+2.096e+01
+1.406e+01
+7.164e+00
+2.630e-01
-6.638e+00
-1.354e+01
-2.044e+01
-2.734e+01
-3.424e+01
-4.114e+01
-4.804e+01
-5.494e+01
Y
Z
X
Step: Step-1
Increment 96: Step Time = 0.5720
Primary Var: S, S33
Deformed Var: U Deformation Scale Factor: +1.582e+01

c)

d)

Figure 8.20: *contours of tensile stresses in the cohesive layer between external and internal layers from reached load equal to 185 kN (about 2mm) (a) to final step increment that corresponds to reached load equal to 342 kN (about 7 mm) (d) by Turon's formulation, case IV.* Legend: MPa.

a)

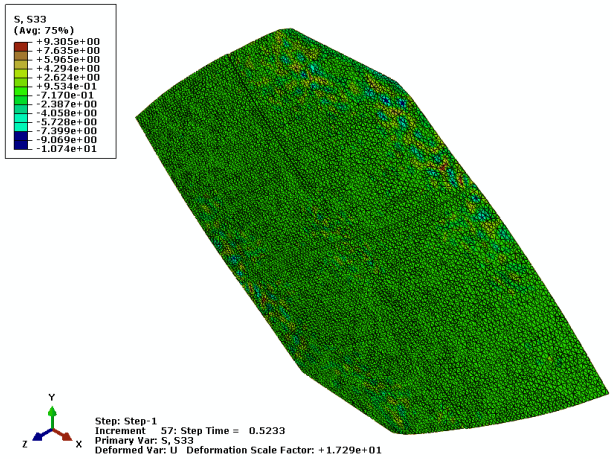

b)

c)

Figure 8.21: contours of tensile stresses in the cohesive element between internal layers from reached load equal to 185 kN, (about 2mm) (a) to final step increment that corresponds to reached load equal to 342 kN, (about 7 mm) (c) by Turon's formulation, case IV. Legend: MPa.

The ***Figure 8.20*** and ***8.21*** show the contours of the tensile stresses perpendicular to the surface in the cohesive layer for four consecutive increment step. At reached load equal to 185 kN (***Figure 8.20a***) the tensile stresses increases and the crack start to propagate between the external and internal layers (***Figure 8.20***), the tensile stress reaches the maximum value in correspondence of the maximum load reached by the simulation, about 453 kN and applied compression displacement between 5.6 mm and 5.9 mm (***Figure 8.20b-c***). According to the cohesive law, crack propagation causes a decrease in the stiffness, and consequently, a reduction in the tensile stress in the subsequent increment step (***Figure 8.20d***) when the damage of the interface is over. The inner layer (***Figure 8.21***) shows the same damage evolution later, from the reached load about 342 kN and applied displacement about 7.3 mm.

The ***Figure 8.22*** shows the contours of the shear stress in the cohesive element, between the external and internal layers (left side) and between the inner layers (right side).

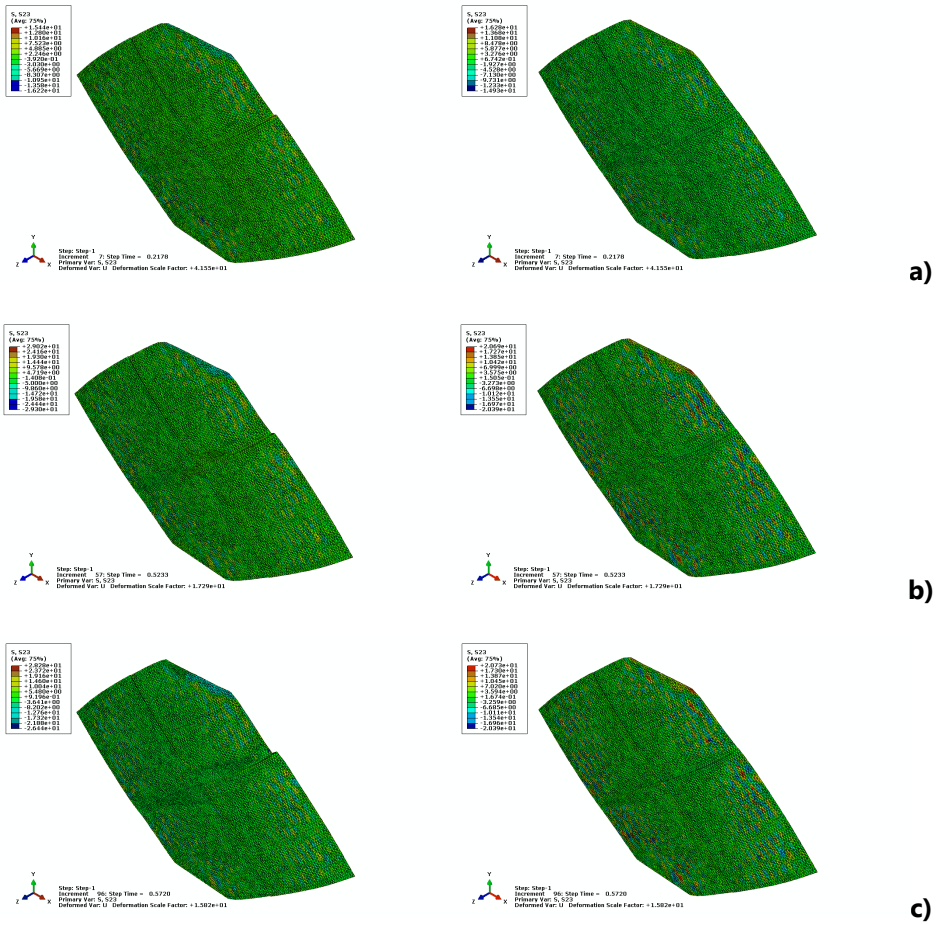

a)

b)

c)

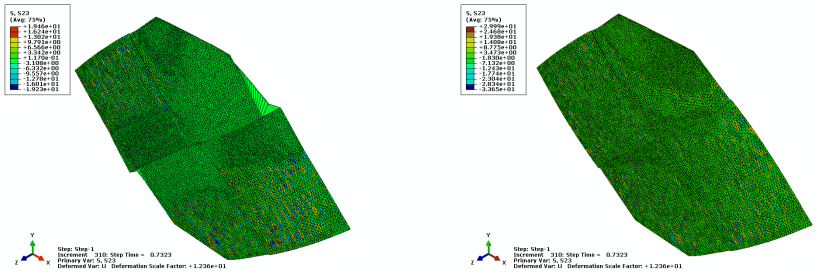

d)

Figure 8.22: contours of the shear stresses in the cohesive element between the external and internal layers (left side) and between the internal layers (right side), by Turon's formulation, case IV. Legend: MPa.

The first contour (***Figure 8.22a***), shows that the shear stress in the cohesive elements is still relatively equal and the next increment (***Figure 8.22b***), shows a moderate increase in the external element while a little decrease in the internal one. In the third contour (***Figure 8.22c***), the shear stress is concentrated in correspondence to the crack propagation in the external layer (left side) and finally by increasing the displacement (about 7.4 mm), the shear stress further increases in the cohesive elements, (***Figure 8.22d***). This corresponds to the maximum displacement reaches by the simulation.

About stiffness values, in the Diehl's penalty approach, it is equal to 7812.5 N/mm^3 and is related to the fracture toughness, G_c (*equation 30*), while in the Turon's approach, the best results are obtained to the stiffness equal to 10^4 N/mm^3, related to the shear modulus (*equation 29*). Below, in ***Figure 8.23*** are shown both the Diehl's and the Turon's curves. It should be noted that in the Diehl's formulation the normal stiffness is equal to the tangential stiffness since one assumes that the fracture toughness is equal in mode I and mode II. Contrary to Diehl different values for normal and tangential stiffness are considered in Turon's equations, derived from elastic and shear modulus, respectively (see ***Table 9***).

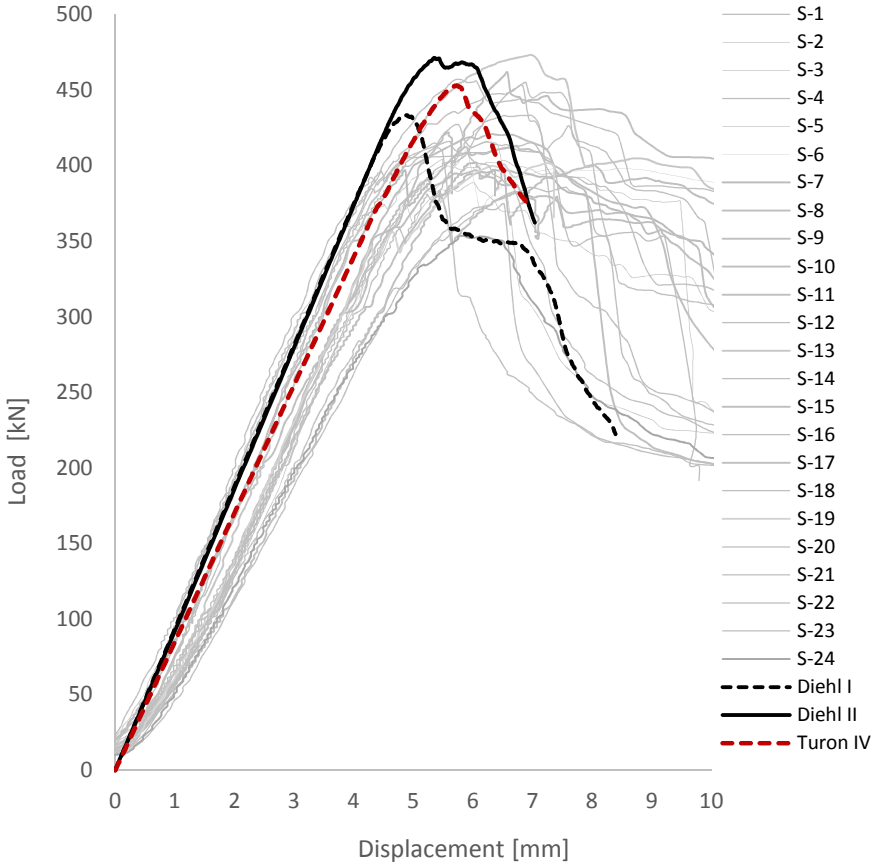

***Figure 8.23*:** load-displacement curves obtained with two different approaches, Diehl vs. Turon.

In the end, the values of model parameters, that consist of a value indicating the stiffness, strength and energy dissipation of the CLT element, were directly set from the experiments. Only the latter has been obtained from the literature, as in all previous cases, by (Dourado et al. 2008; E. I. Saavedra Flores et al. 2016). Since it is considered most important for the overall structural response to get a good approximation of the initial stiffness of the cohesive zone, the stiffness parameter for mode II is chosen equal to the shear modulus reported in ***Table 4*** considering a thickness of the cohesive element equal to 1mm. The mode I stiffness parameter of the CZM that has been obtained and adjusted by fitting simulations to measured force-displacement curves ranges from 10^2 to 10^5 N/mm^3.

As in the previous models, the mode interaction in damage initiation is defined by a quadratic stress criterion, while the interaction in damage evolution follows the model of (Benzeggagh and Kenane 1996). The strength parameters are calibrated using both the experimental data showed in ***Table 4*** and the strength value of interface equal to 2.7 MPa, calculated as reported in *section 8.2.1*. One considers the shear stress τ applied in the cohesive element between

the layers, while the rolling shear in the surface within the single layer. The load-displacement curves for a calibrated model, with the value of shear strength defined in *section 6*, are displayed in ***Figure 8.24***.
The initial stiffness and the maximum load of the calibrated models show a not good agreement with the experiments, in particular, the cases with a lower strength of interface (2.7 MPa). The case with the normal interface stiffness equal to 10^3 N/mm^3 coupled with a higher value of interface strength (16.2 MPa) also not match with the actual experimental damage evolution, (***Figure 8.24***). The latest two cases with the normal interface stiffness equal to 10^4 and 10^5 N/mm^3 show a higher value of maximum load (380 kN and 410 kN, respectively) than the other cases. These models allows a better description of the failure of the sample, ***Figure 8.24***. Nevertheless, the shape of the curves differs from the previous models (Diehl and Turon) and not reproduces accurately the nonlinear elastic law that characterises the behaviour before the failure. Thus, these models are not able to describe the softening law and the failure of the CLT specimens adequately. As shown in ***Figures 8.25*** and ***8.26***, the internal layers are not influenced by a significant failure, while the external layers are subjected to a substantial failure and a major displacement.

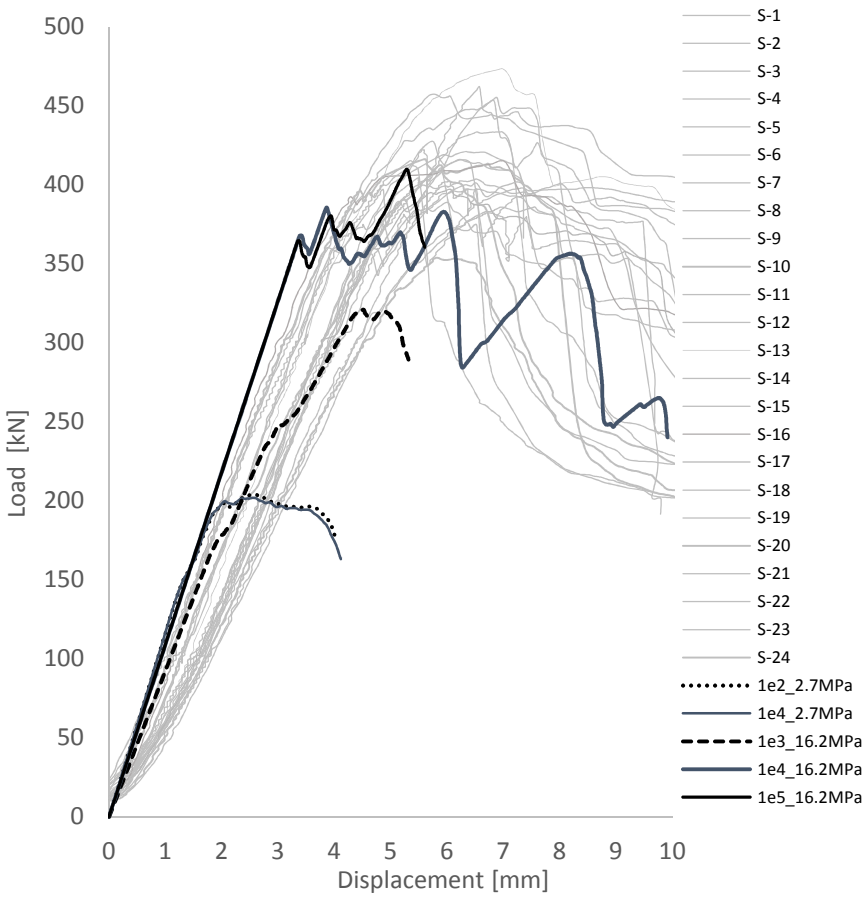

Figure 8.24: *load-displacement curves obtained by setting stiffness and shear strength (perpendicular to the grain and the rolling shear) from the experimental results.*

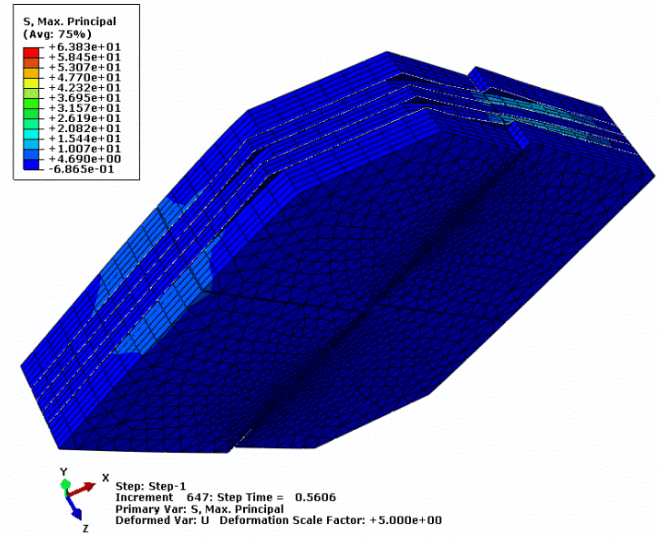

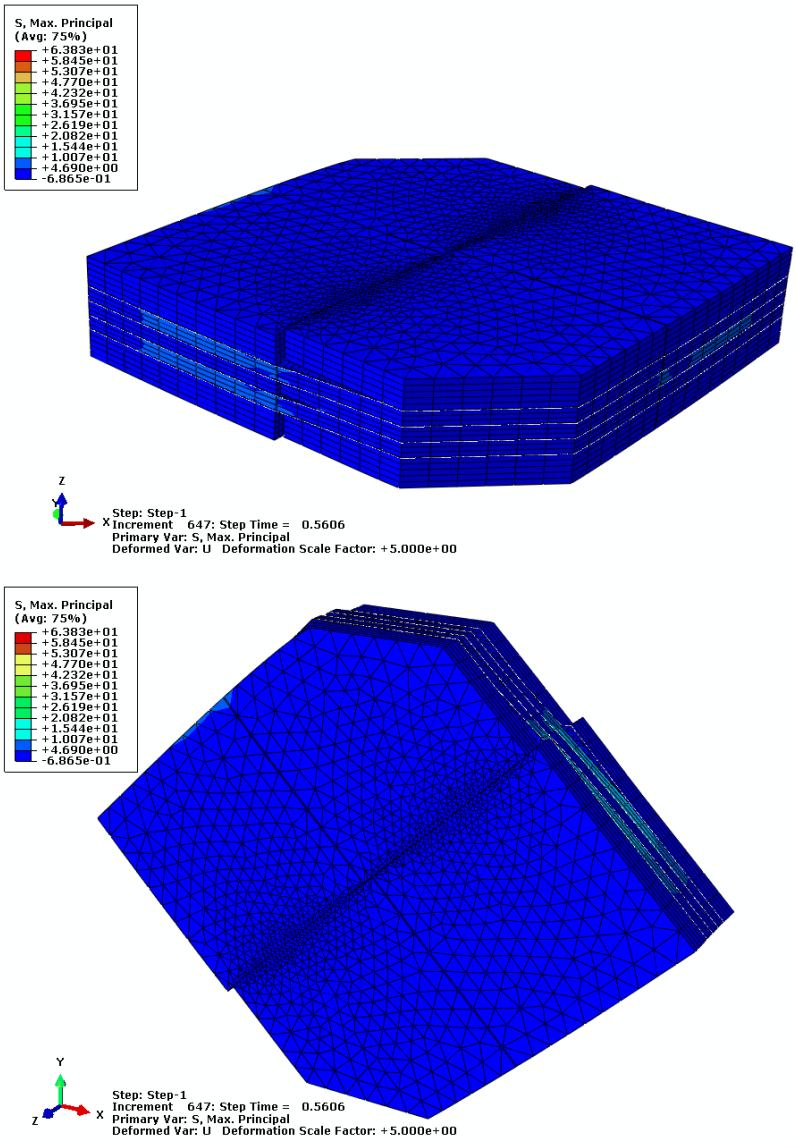

Figure 8.25: failure of the CLT element with calibrated model, case with normal stiffness equal to 10^5 N/mm^{3}and interface strength equal to 16.2 MPa. Legend: MPa.

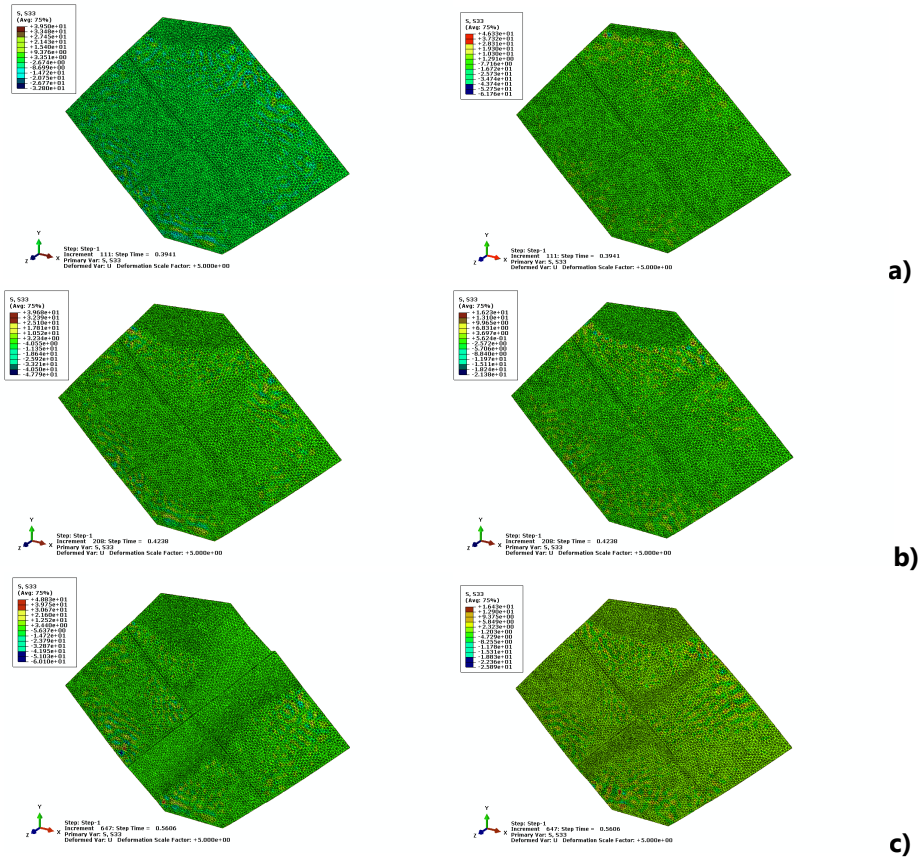

Figure 8.26: contours of tensile stresses in the cohesive element between the external and internal layers (left side) and between the inner layers (right side). From applied displacement equal to 4mm(a) to final load reached 360 kN and applied displacement equal to 5.6mm (c), case with normal stiffness equal to 10^5 N/mm^3 and interface strength equal to 16.2 MPa. Legend: MPa.

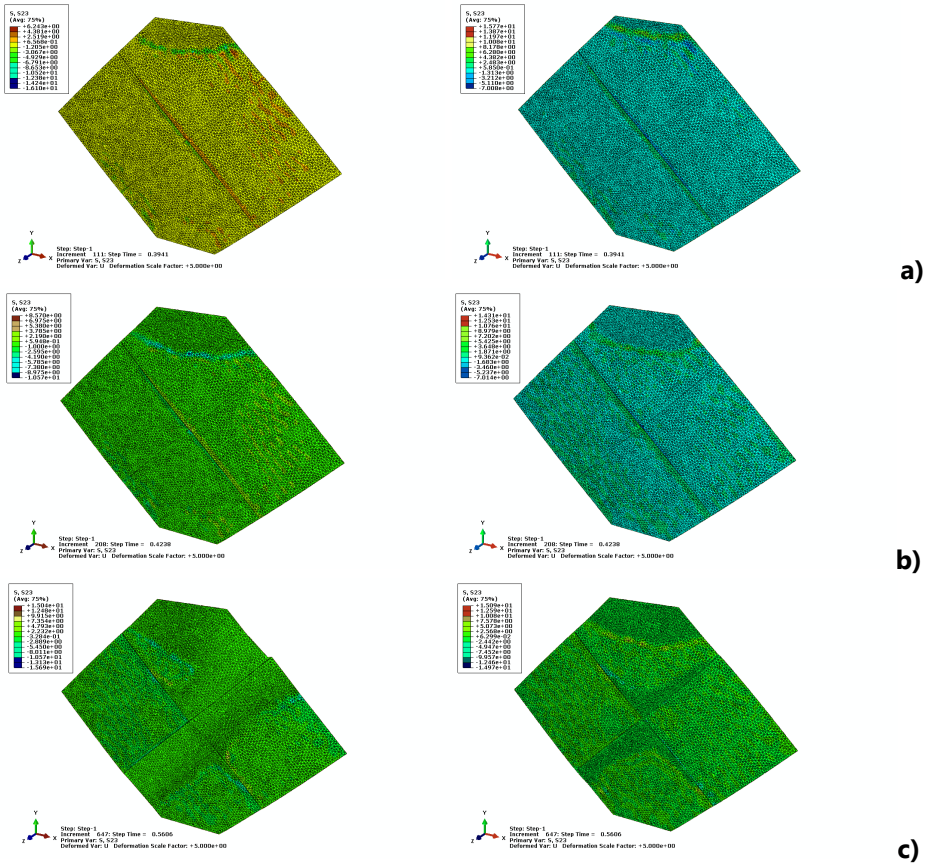

***Figure 8.27*: contours of the shear stresses in the cohesive element between the external and internal layers (left side) and between the internal layers (right side). From applied displacement equal to 4mm (a) to final load reached 360 kN and applied displacement equal to5.6mm (c), case with normal stiffness equal to 10^5 N/mm^3 and interface strength equal to 16.2 MPa Legend: MPa.**

The ***Figure 8.26*** shows the contours of the tensile stresses perpendicular to the surface in the cohesive elements for three consecutive increment step. From the applied displacement, equal to 4 mm (***Figure 8.26a***) the tensile stresses increases and the crack start to propagate after the displacement equal to 4.4 mm, with a load about of 365 kN only in the cohesive element between the external and internal wooden layer (left side in ***Figure 8.26b-c***). According to the cohesive law, crack propagation causes a decrease in the stiffness, and consequently, a decrease in the tensile stress in the subsequent increment of displacement. While in the inner layer (right side in ***Figure 8.26***), a progressive increase of the tensile stress is detected without the failure in the layers.
The ***Figure 8.27*** shows that the shear stress in the cohesive elements is still relatively low and the next increment (***Figure 8.27b***), shows an increase in the shear at the cohesive element in contact with the external wooden layer, which

reaches the failure at displacement about of 5.3 mm(left side in ***Figure 8.27c***). In the right side of ***Figure 8.27***, are shown the shear stress evolution of the cohesive element in contact with two internal wooden layers. In all displacement increments, the shear stress is lower than the cohesive element near the external layer, and the cohesive element is not able to describe the failure of the internal layer.

From the cases showed in ***Figure 8.24***, one more time is evident that the tangential stiffness plays the most influential role in the overall behaviour of the panel and results too low if one takes into consideration the shear modulus of the panel. Thus, the subsequent step consists in varying the tangential stiffness in the range of 10^2 and 10^4 N/mm^3 (***Figure 8.28)***. Each case reported below, is characterised by interface strength as previously defined and reported in ***Table 4***.

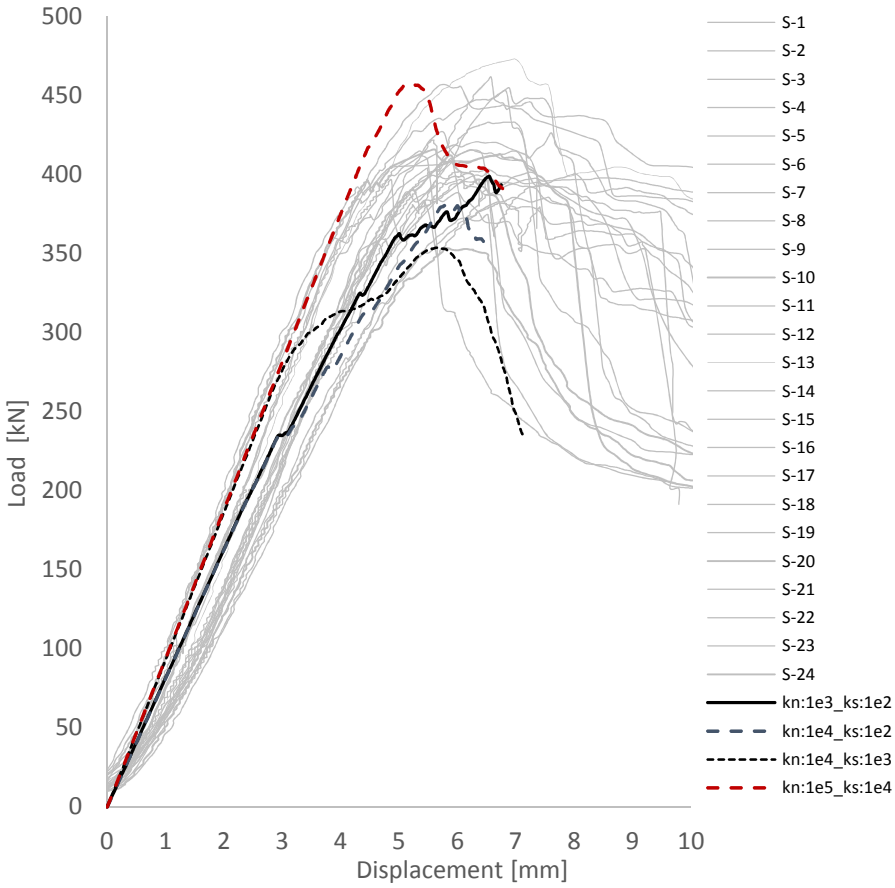

Figure 8.28: load-displacement curves obtained by setting normal (k_n) and tangential (k_s) stiffness with shear strength (perpendicular to the grain and the rolling shear) from the experimental results.

The best match results from the interface strength that is equal to 16.20 MPa (red dashed line in ***Figure 8.28***). Cases with lower interface strength (2.7 MPa)

show a not adequate behaviour if compared with the experimental curves (black lines in ***Figure 8.28***). A closer examination of the ***Figure 8.28*** highlights other important issues: the initial stiffness of the panel before the damage takes place and the role of the dissipated energy considered in the simulation. The first issue suggests that is adequate to consider the shear modulus of timber material in the range of 350-400 MPa, in any case not over 450 MPa, as reported in ***Table 5***. The second one shows the possibility to increase the dissipated energy to characterise the cohesive interface, to obtain a greater ductility before the softening law takes place. With reference to the above curve with normal stiffness and tangential stiffness equal to 10^5 and 10^4 kN/mm^3 respectively, below (***Figure 8.28***) are reported for the same stiffness parameters, an example to lower shear modulus (350 MPa - *CASE* I) and to higher dissipated energy (0.15 N/mm - *CASE* II).

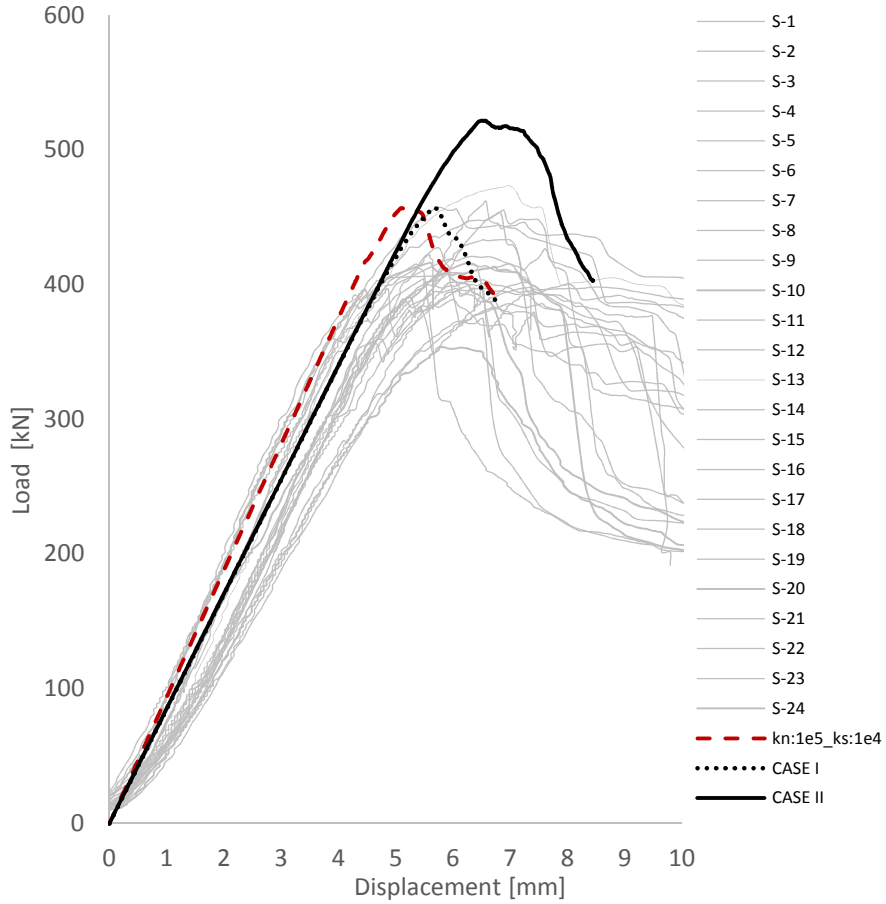

Figure 8.29: load-displacement curves obtained by setting a lower shear modulus to characterise the timber material (*CASE I*), and by setting a higher fracture energy to characterise the cohesive interfaces (*CASE II*).

8.2.1 Experimental data for adhesive strength

The investigation of quality of the bonded interface is carried out in (K. Sikora, Harte, and McPolin 2014) and also in (Martins et al. 2013). The studies involved the tolerance testing of the boards, shear tests of the edge bonds and delamination test. The same tests are performed in the laboratory of the CNR-IVALSA Institute, and the results will be used to simulate the behaviour of the pieces.

To ensure a uniform moisture content in the specimens during the testing, boards were stored in conditioning chamber (65 ± 5% R.H., 20 ± 2°C). After reconditioning, different samples of CLT panel are tested in a compressive testing machine; the two types differ in a thickness of internal boards. The thickness values for each specimen are reported in ***Table 12***. Each of the test pieces comprised four glue lines and has a 50 x 50 mm^2 square cross section.

Specimens ID	n° of samples	Thickness of board [mm]
A (1to 8)	8	40-20-40-20-40
B (9 to 12)	4	40-20-20-20-40

Table 12: *thickness values for each board.*

A single-component polyurethane adhesive, formulated for the manufacture of engineered wood product (PUREBOND HB S309), is used to bond the edges of the shear test specimens. The 0.1 mm adhesive layer is applied on one surface of each glue line, and 1 MPa pressure is applied by compressive testing machine. The test programme and procedure are in accordance with Annex D of (*EN 16351:2015 Timber, Timber Structure - Cross Laminated Timber - Requirements, CEN* 2015) that is based on (*EN 392:1995 Glued Laminated Timber - Shear Test of Glue Lines, CEN* 1995). The load was applied under displacement control at a rate of 3 mm/min, ensuring failure after no less than 20 s. The shear strength is determined for every of four glue lines from four test, and the results are given in ***Table 13*** and ***Figures 8.28-8.29***. The shear strength is calculated in accordance with (*EN 16351:2015 Timber, Timber Structure - Cross Laminated Timber - Requirements, CEN* 2015) as:

$$f_V = k \frac{f_U}{A} \tag{31}$$

where f_U is the ultimate load in [N], A is the shear area in [mm^2], k is the modification factor, and it is equal to 0.78 + 0.0044t, and t is a thickness in [mm]. In ***Table 13*** is reported the wood failure percentage of a split glue area that is the ratio of the area with wood failures and the glued area before splitting. The wood percentage failures are above 90% except for 77% of specimens three due to a resin pocket, and of 85% for specimens 4. Wood failure percentages results for PUR type adhesives are generally very high and exhibited a small variation, which

corresponds to results in the literature. Ultimate loads of each test and the determined average are also given in ***Table 13.*** For the sake of brevity, ***Table 13*** shows only the results of specimens "B", which correspond to the same stratification of the CLT panels adopted in the compression tests. The mean shear strength for all tested glue lines is 2.71 N/mm^2.

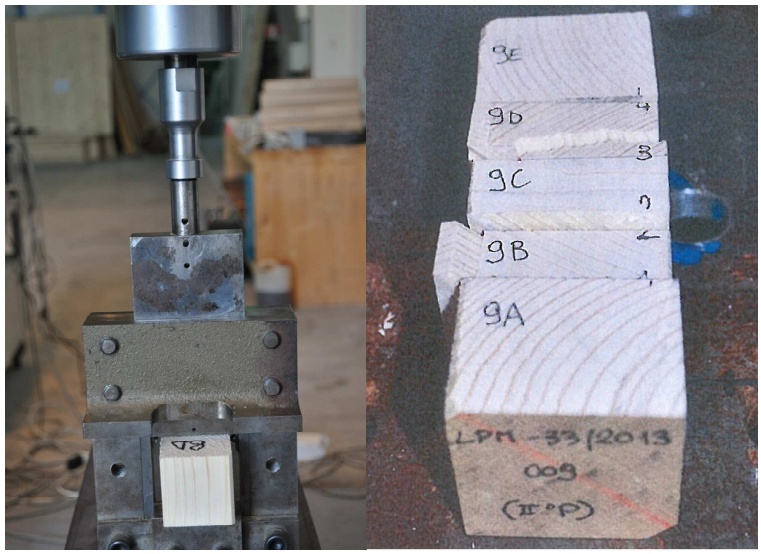

***Figure 8.30*:** specimens during the test in the shearing machine (left), specimen 9 after the shear test (right, 90% wood failure).

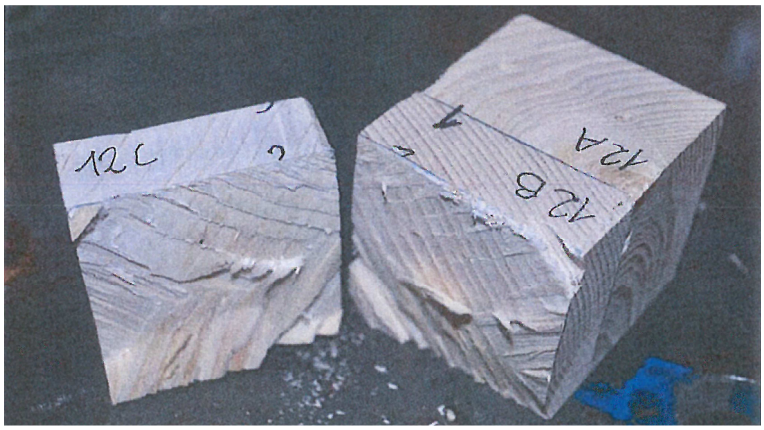

***Figure 8.31*:** glue line 12_II (100%wood failure).

Specimen ID		Ultimate Load [N]	Wood percentage failure [%]	Shear strength [N/mm^2]	Shear Area [mm^2]
9	I	5002	80	1.86	2694
	II	4305	90	1.63	2641
	III	8179	100	3.14	2607
	IV	5747	90	2.22	2590
10	I	5041	100	1.97	2555
	II	6855	100	2.65	2589
	III	8042	100	3.08	2612
	IV	6718	90	2.54	2644
11	I	6237	100	2.30	2708
	II	9052	80	3.38	2675
	III	11642	50	4.40	2644
	IV	6237	Resin pocket	2.39	2606
12	I	9278	100	3.41	2719
	II	8179	100	3.11	2628
	III	6169	70	2.37	2599
	IV	7581	70	2.94	2576
Minimum shear strength				1.63	
Maximum shear strength				4.40	
Mean shear strength				***2.71***	
Standard deviation				0.70	
COV				25.96	

Table 13: shear strength and wood percentage failure.

Chapter 9
Conclusion and future remarks

The primary objective of this research project was to find a viable method that allows the description of the nonlinear behaviour of the Cross-Laminated Timber. The CLT component, due to its structure, has far more strength and stiffness than the resistant grade of the individual timber specimen. However, the laminated composition and then the discontinuities within the CLT elements (glue lines) are the most important focus to understand the development of the nonlinear behaviour and their failure.

This study has presented numerical simulations of failure in a surface-bonded element using Cohesive Zone Model technology in a commercial Finite Element Analysis code (FEA). A practical penalty framework has been assumed to address the problematic issue of determining various cohesive element properties when only a single input was known, the critical fracture energy G_c. Comparison with experimental data demonstrates the accuracy of the FEA results for the nonlinear behaviour and damage evolution in the CLT panel.

Several parameters have been considered, their influence and meaning into the FEA. As stated previously, the main parameter that defines the cohesive material is the maximum interfacial strength, *t [MPa]*. This can be treated just a dependent penalty parameter that is directly related to the physical value G_c and the penalty value of cohesive ductility, δ_f. As the cohesive ductility penalty is stiffened, the value of *t* will increase. Since this value will be the stress action in normal and tangential to the cohesive element at the time that damage initiates and the crack begins to propagate, its value can have a strong influence on the solution. In particular, if its value is set higher than the maximum allowable stress that the adjacent material, connected to the cohesive element can endure, then a good solution will not be possible, and the simulation often will terminate. In this case, the cohesive ductility penalty will be clearly too stiff for the physics of the problem defined. This result may be easily explained. Bonding a weak material (relatively low ultimate strength) with a high strength adhesive is likely to cause a bulk material failure in the weak material and not a failure in the bond interface. This also points out that the values of normal and tangential stresses to the cohesive element near the crack front is ill-defined since a penalty parameter drives it. This is consistent with the view that using an energy-based approach to analyse the failure, one takes a global or smeared approach to the problem, as opposite view

to a highly local or detailed analysis that is utilised with classical fracture mechanics methods.

It worth to noting that the penalty method proposed by (Diehl 2008a) and applied to the CLT elements in the present research, leads to an estimation of the interfacial strength which is very close to the calculated value of the shear stress in the internal layers of the CLT (***Table 14***). Due to the good agreement with experimental results, the presented approach can represent a suitable tool for the characterization of the nonlinear behaviour of the CLT including both the damage evolution and failure mode. In the below, the predicted and experimental stresses are summarised (***Table 14***). From the literature, the main parameters to define the mechanical behaviour of the CLT under the in-plane shear load are the pure shear strength, the shear strength perpendicular to the grain in each layer, the torsional shear component and the rolling shear, the shear stiffness (Jobstl et al. 2004; Andreolli, Rigamonti, and Tomasi 2014). From the experimental data, the same range of values has been obtained, with an overestimation of about 26% for the shear strength perpendicular to the grain, while the rolling shear and the pure shear values are confirmed. Also, the numerical approach permits one to establish a range of value, which should be determined by careful consideration and study for the singular problem, able to describe the behaviour of CLT element. It worth to noting that sizing the cohesive penalty approach must be done about the level of detail desired in the model (mesh density).

	Shear strength perp. to the grain	***Rolling shear strength***	***Interface strength***	***Internal layer strength***
Literature	12.80	0.7 to 1.5	-	-
Experimental data	6.5 - 16.20	1.50	-	-
Diehl's Numerical approach	-	-	12.5	1.50
	Experimental data	**EN 338:2009 (C24)**	**(Unterwieser and Schickhofer 2014)**	**DIN 1052:2004**
Pure shear strength [MPa]	*4.2*	*4.0*	*5.0*	*2.5*

Table 14: *summary of predicted and experimental values of shear strength expressed in N/mm².*

Another issue to consider is the selection of the (interface) stiffness parameter, *K*. It worth to remark that the effective elastic properties of the whole laminated element depend on the properties of both the cohesive surfaces and the bulk constitutive relations of the layers. Although the compliance of the cohesive surface can contribute to the global deformation, its only purpose is to simulate a fracture. Thus, the effective elastic properties of the wooden elements will not be affected by the cohesive surface. However, this might not totally be true. The

complications in the absorption of the adhesive arise from not being able to accurately and with certainty determine the initial surface properties of the timber elements.
Superficial defects of the surface may allow for increased absorption, thus making any reasonable estimates difficult. The absorption of the resin into the timber grain through the pressure that would be applied by the glueing clamps can effectively be considered as a form of resin impregnation and can explain the higher value of the initial stiffness in the experimental load-displacement curves than the lower values in the simulations.
However, also the penalty value of stiffness given by Diehl, approaches accurately both the experimental data and the result obtained with the Turon's formulation. Thus, the same conclusion can be drawn concerning the results achieved by using the actual value of the interface strength to calculate the interface stiffness and the penalty value of the interface stiffness. In both cases, the formulations provide an adequate stiffness to ensure a sufficiently stiff connection between two neighbouring layers. Alternatively, the interface stiffness has been identified by fitting the experimental data starting from the elastic modulus and shear modulus of CLT. In this way, a different range of values is determined and different shape of load-displacement curves is detected, with a lower accuracy in the failure mode of the CLT panel. However, models can be sufficient to describe the main features of interface failure for the simulation of bonded layers.
Another important parameter to study when dealing with failure simulations is the impact of the FE mesh on the results. The effects of the mesh size of the FE Model, including the cohesive elements, depend on the combination of all the different parameters that have an impact on the results instead of the parameters individually. In literature, one can find many different minimum lengths of the cohesive element mesh, which are reported in the present research, needed in the fracture process zone. However, is not always that obvious, since it is the combination of the different parameters, which results in an accurate set of FE results.

In the end, the major findings are summarised in the follow:

- The non-linear behaviour of the Cross Laminated Timber panels, with a good agreement of the softening law, was defined through the comparison between the experimental and numerical results;

- The main non-linear mechanical parameters were defined using a damaged model. The continuous part is characterised by elastic orthotropic constants while traction-separation law describes the behaviour of the discontinuities (glued lines).

- The framework will provide the capability to perform the damage analysis to determine the non-linear response of CLT under in-plane shear load.

The simulations also demonstrated the ability to track the failure path due to the cohesive elements.

- The framework provides the basis for investigating the damage state predictions in the non-linear behaviour of CLT elements.

9.1 New application and further research

Further analysis would help build a complete understanding of the limits and nonlinear properties of this construction material.
In first should be enhanced the approach about the initial stiffness of the wooden element due to the possible effects of the adhesive absorption.
More accurate investigations would be desirable about the influence of the length of the cohesive elements as well as the effect of the length of the continuum mesh. Additionally, different 3D models should be used for the modelling of the CLT failure considering the asymmetrical configuration of the slip surfaces within the single layer and different value of dissipated energy to characterise the cohesive interfaces, with the aim to assess the possibility to obtain a better fitting of the experimental data.
Finally, the most ambitious objective would be to develop the possibility of using CLT panels for rehabilitation and strengthening of existing buildings against seismic force. Some research is already available in this field in both the masonry buildings and the reinforced concrete frame buildings. The first results of this study, confirm that the Cross-Laminated Timber is a suitable new technology of strengthening and can prevent the collapse of an already severely damaged building.

BIBLIOGRAPHY

Anderson, T. L. I. 2005. *Fracture Mechanics - Fundamentals and Applications*.

Andreolli, M., M. Rigamonti, and R. Tomasi. 2014. 'Diagonal Compression Test on Cross Laminated Timber Panels'. In *The 13th World Conference on Timber Engineering*, edited by Alexander Salenikovich, 9.

Andreolli, M., R. Tomasi, and A. Polastri. 2012. 'Experimental Investigation on in-Plane Behaviour of Cross-Laminated Timber Elements'. In *CIB - W18*, 1–11.

ANSI/APA PRG 320-2012 Standard for Performance-Rated Cross-Laminated Timber. The Engineered Wood Association. 2012. *ANSI/APA PRG 320-2012 Standard for Performance-Rated Cross-Laminated Timber*.

Ardalany, Manoochehr, Bruce Deam, and Massimo Fragiacomo. 2012. 'Experimental Results of Fracture Energy and Fracture Toughness of Radiata Pine Laminated Veneer Lumber (LVL) in Mode I (Opening)'. *Materials and Structures* 45 (8): 1189–1205. doi:10.1617/s11527-012-9826-1.

Ardalany, Manoochehr, Massimo Fragiacomo, and Peter Moss. 2015. 'Modelling of Laminated Veneer Lumber Beams with Holes Using Cohesive Elements'. *Journal of Structural Engineering* 2 (1): 1–13. doi:10.1061/(ASCE)ST.1943-541X.0001338.

Barenblatt, G.I. 1962. 'The Mathematical Theory of Equilibrium Cracks in Brittle Fracture'. In *Adv. Appl. Mech.*, 7:55–129. doi:10.1016/S0065-2156(08)70121-2.

Bauer, H., and G. Schickhofer. 2016. 'Test Configurations and Analysis for Determining Characteristic Properties of Cross Laminated Timber (CLT)'. In *World Conference on Timber Engineering, WCTE 2016, August 22-25*. Vienna, Austria.

Bažant, Zdeněk P. 2001. 'Concrete Fracture Models: Testing and Practice'. *Engineering Fracture Mechanics* 69 (2): 165–205. doi:10.1016/S0013-7944(01)00084-4.

Benzeggagh, M. L., and M. Kenane. 1996. 'Measurement of Mixed-Mode Delamination Fracture Toughness of Unidirectional Glass/epoxy Composites with Mixed-Mode Bending Apparatus'. *Composites Science and Technology* 56 (4): 439–49.

Betti, Michele, Michele Brunetti, Marco Pio Lauriola, Michela Nocetti, Francesco Ravalli, and Benedetto Pizzo. 2016. 'Comparison of Newly Proposed Test Methods to Evaluate the Bonding Quality of Cross-Laminated Timber (CLT) Panels by Means of Experimental Data and Finite Element (FE) Analysis'. *Construction and Building Materials* 125. Elsevier Ltd: 952–63. doi:10.1016/j.conbuildmat.2016.08.113.

Blass, HJ., and P. Fellmoser. 2004. 'Design of Solid Wood Panels with Cross Layers'. In *8th World Conference on Timber Engineering*, 14:1001–6. http://holz.vaka.kit.edu/public/36.pdf.

Blass, HJ., and R. Goerlacher. 2002. 'Zum Trag- Und Verformungsverhalten von Brettsperrholzelementen Bei Beanspruchung in Plattenebene'. *Bauen Mit*

Holz 104 (11): 34–41.

Blau, Peter J. 2001. 'The Significance and Use of the Friction Coefficient'. *Tribology International* 34 (9): 585–91. doi:10.1016/S0301-679X(01)00050-0.

Bodig, Jozsef, and Benjamin A. Jayne. 1993. *Mechanics of Wood and Wood Composites*. Reprint ed. New York: Malabar, Fla.: Krieger Pub., 1993.

Bogensperger, T.a, T.b Moosbrugger, and G.c Silly. 2010. 'Verification of CLT-Plates under Loads in Plane'. *11th World Conference on Timber Engineering 2010, WCTE 2010* 1: 231–40.

Bogensperger, T., T.H. Moosbrugger, and G Schickhofer. 2007. 'New Test Configuration for Clt Wall Elements under Shear Load'. In *MEETING FORTY BLED*. SLOVENIA.

Bosl, R. 2002. 'Zum Nachweis Des Trag-Und Verformungsverhaltens von Wandscheiben Aus Brettlagenholz'. Dissertation, Universitat der Bundeswehr Munchen, Fakultat fur Bauingenieur- und Vermessungswesen (in German).

Bostrom, L. 1992. 'Method for Determination of the Softening Behaviour of Wood and the Applicability of a Nonlinear Fracture Mechanics Model'. Report TVBM-1012, Lund Sweden.

Bradner, R. 2016. 'Group Action of Axially-Loaded Screws in the Narrow Face of Cross Laminated Timber'. In *World Conference on Timber Engineering, WCTE 2016, August 22-25*. Vienna, Austria.

Brandner, R., T. Bogensperger, and G. Schickhofer. 2013. 'In Plane Shear Strength Of Cross Laminated Timber (CLT): Test Configuration, Quantification and Influencing Parameters'. In *International Council for Research and Innovation in Building and Construction, CIB-W18*, 1–13.

Brandner, R., G. Flatscher, A. Ringhofer, G. Schickhofer, and A. Thiel. 2016. 'Cross Laminated Timber (CLT): Overview and Development'. *European Journal of Wood and Wood Products* 74 (3): 331–51. doi:10.1007/s00107-015-0999-5.

Broek, David. 1986. *Elementary Engineering Fracture Mechanics*. Edited by Martinus Nijhoff Publishers. Dordrecht: Springer Netherlands. doi:10.1007/978-94-009-4333-9.

Camanho, Pedro Ponces, C.G. Dávila, and M. F. de Moura. 2003. 'Numerical Simulation of Mixed-Mode Progressive Delamination in Composite Materials'. *Journal of Composite Materials* 37 (16): 1415–38.

Carrington, H. 1922. 'The Elastic Constants of Spruce as Affected by Moisture Content'. *Aeronautical Journal* 26: 462–471.

Ceccotti, A. 2010. *Il Progetto Sofie, in Il Progetto Sostenibile N. 25, Edicom Edizioni*.

Ceccotti, A, C Sandhass, and M Yasumura. 2011. *Il Progetto Sofie. Prestazioni Sismiche Di Edifici in X-Lam, in L'Edilizia, N. 169, Speciale Legno: Progettazione, Strutture, Sismica, De Lettera Editore*. Edited by De Lettera Editore.

Ceccotti, Ario, Maurizio Follesa, and Marco Pio Lauriola. 2007. 'La Sperimentazione Sismica Sulle Costruzioni Di Legno: Attualità E Prospettive'. In *Seminario Internazionale CIAS*, 261–80.

Czaderski, C, R Steiger, M Howald, S Olia, A Gulzow, and P Niemz. 2007. 'Tests

and Calculations on 3-Layered Cross-Laminated Solid Wood Panels Supported at All Edges'. *Holz Als Roh-Und Werkstoff* 65 (5): 383–402.

Daudeville, L. 1999. *Fracture in Spruce: Experiment and Numerical Analysis by Linear and Nonlinear Fracture Mechanics*. Holz als R. Ó Springer-Verlag 1999.

Diehl, T. 2004. 'Modeling Surface-Bonded Structures with ABAQUS Cohesive Elements : Beam-Type Solutions'. *2004 ABAQUS Users' Conference*, 1–27.

———. 2008a. 'On Using a Penalty-Based Cohesive-Zone Finite Element Approach, Part I: Elastic Solution Benchmarks'. *International Journal of Adhesion and Adhesives* 28 (4–5): 237–55. doi:10.1016/j.ijadhadh.2007.06.003.

———. 2008b. 'On Using a Penalty-Based Cohesive-Zone Finite Element Approach, Part II: Inelastic Peeling of an Epoxy-Bonded Aluminum Strip'. *International Journal of Adhesion and Adhesives* 28 (4–5): 256–65. doi:10.1016/j.ijadhadh.2007.06.004.

Dinwoodie, J. M. 1981. *Timber: Its Nature and Behaviour*. New York.

Dourado, N., S. Morel, M. F S F de Moura, G. Valentin, and J. Morais. 2008. 'Comparison of Fracture Properties of Two Wood Species through Cohesive Crack Simulations'. *Composites Part A: Applied Science and Manufacturing* 39 (2): 415–27. doi:10.1016/j.compositesa.2007.08.025.

Dugdale, D.S. 1960. 'Yielding of Steel Sheets Containing Slits'. *Journal of the Mechanics and Physics of Solids* 8 (2): 100–104. doi:10.1016/0022-5096(60)90013-2.

Dujic, Bruno, Simona Klobcar, and Roko Zarnic. 2007. 'Influence of Openings on Shear Capacity of Wooden Walls'. In *Proceedings of the 40th CIB-W18 Meeting*, 16:5–17.

EN 13353:2008 Solid Wood Panels (SWP). Requirements, CEN. 2008.

EN 13354:2008. Solid Wood Panels (SWP) – Bonding Quality – Test Method. CEN. 2008.

EN 13986+A1:2015 Wood-Based Panels for Use in Construction - Characteristics, Evaluation of Conformity and Marking, CEN. 2015.

'EN 14080:2013 Timber Structures — Glued Laminated Timber and Glued Solid Timber — Requirements - British Standards Institute'. 2013.

EN 15425: Adhesives – One Component Polyurethane for Load Bearing Timber Structures – Classification and Performance Requirements. 2008.

EN 16351:2015 Timber, Timber Structure - Cross Laminated Timber - Requirements, CEN. 2015.

'EN 301: Adhesives, Phenolic and Aminoplastic, for Load-Bearing Timber Structures - Classification and Performance Requirements'. 2013.

EN 338: Structural Timber — Strength Classes - British Standards Institute. 2009. British Standards Institute.

EN 392:1995 Glued Laminated Timber - Shear Test of Glue Lines, CEN. 1995.

EN 408:2010 Timber Structures - Structural Timber and Glued Laminated Timber - Determination of Some Physical and Mechanical Properties, CEN. 2010. Vol. 44.

EN 789:2005 Determination of Mechanical Properties of Wood-Based Panels, CEN.

2005.

'EOTA-ETA-14/0349: Cross Laminated Timber - Solid Wood Slab Elements to Be Used as Structural Elements in Buildings.' 2014.

Faherty, K. F., and T. G. Williamson. 1999. *Wood Engineering and Construction*. Edited by McGraw-Hill. Handbook.

Falk, R., H ., and François Colling. 1995. 'Laminating Effects in Glued-Laminated Timber Beams'. *Journal of Structural Engineering*, no. December: 1857–63.

Falk, M. L., A. Needleman, and J. R. Rice. 2001. 'A Critical Evaluation of Cohesive Zone Models of Dynamic Fracture'. *Journal de Physique IV* 11: 43–50. doi:10.1051/jp4:2001506.

Feio, A. 2005. 'Inspection and Diagnosis of Historical Timber Structures: NDT Correlations and Structural Behaviour'. Universidade do Minho, Guimaraes, 2005, 208 pp.

Flaig, M., and H.J. Blass. 2013. 'Shear Strength and Shear Stiffness of CLT-Beams Loaded in Plane'. *International Council for Research and Innovation in Building and Construction - Working Commission W18 - Timber Structures*, no. August: 243–58.

Fragiacomo, M., B. Dujic, and I. Sustersic. 2011. 'Elastic and Ductile Design of Multi-Storey Crosslam Massive Wooden Buildings under Seismic Actions'. *Engineering Structures* 33 (11). Elsevier Ltd: 3043–53. http://dx.doi.org/10.1016/j.engstruct.2011.05.020.

Gereke, Thomas, and Peter Niemz. 2010. 'Moisture-Induced Stresses in Spruce Cross-Laminates'. *Engineering Structures* 32 (2): 600–606.

Gibson, L. J., and M. F. Ashby. 1988. 'Cellular Solids, Structure and Properties'. *Oxford: Pergamoon*.

Griffith, A. A. 1920. 'The Phenomenon of Rupture and Flow in Solids'. *Philos. Trans. R. Soc. Lond.* A221: 163–98.

Gubana, A. 2009. 'Consolidamento Sismico Di Solai in Legno Con Pannelli XLam'. In *Convegno Nazionale Sicurezza E Conservazione*. http://www.iuav.it/ricerca1/attivita-/aree-temat/conservazi/controllo-/eventi/seminario-/09-a_gubana.pdf.

Gulzow, A, D Gsell, and R Steiger. 2008. 'Non-Destructive Evaluation of Elastic Parameters of Square-Shaped Cross-Laminated Solid Wood Panels, Built up Symmetrically with 3 Layers'. *Holz Als Roh-Und Werkstoff* 66 (1): 19–37.

Hayhurst, D R. 1972. 'Creep Rupture under Multi-Axial State of Stress'. *Journal of Mechanics and Physics of Solids* 20: 381–90.

Hillerborg, A., M. Modeer, and P-E. Petersson. 1976. 'Analysis of Crack Formation and Crack Growth in Concrete by Means of Fracture Mechanics and Finite Elements Hillerborg 1976.pdf'. *Cement and Concrete Research*, 773–82.

Holmberg, Stefan, Kent Persson, and Hans Petersson. 1999. 'Nonlinear Mechanical Behaviour and Analysis of Wood and Fibre Materials'. *Computers & Structures* 72 (4–5): 459–80. doi:10.1016/S0045-7949(98)00331-9.

Hui, C.- Y., J. A., S. J. Bennison, and J. D. Londono. 2003. 'Crack Blunting and the Strength of Soft Elastic Solids'. *Proceedings of the Royal Society A:*

Mathematical, Physical and Engineering Sciences 459 (2034): 1489–1516. doi:10.1098/rspa.2002.1057.

Irwin, G. R. 1948. 'Fracture Dynamics'. *Fracturing of Metals, American Society for Metals*, 147–66.

Irwin, G.R. 1960. 'Plastic Zone near a Crack and Fracture Toughness'. In *Proceedings of Seventh Sagamore Ordnance Materials Conference 4*, 63–78.

Jeitler, Georg. 2004. 'Versuchstechnische Ermittlung Der Verdrehungskenngrössen von Orthogonal Verklebten Brettlamellen [Experimental Determination of Torsion Properties of Orthogonally Bonded Board Segments]'. Master's thesis, Graz University of Technology (in German).

Jernkvist, L.O. 2001a. 'Fracture of Wood under Mixed Mode Loading: I. Deviation of Fracture Criteria'. *Engineering Fracture Mechanics* 68 (5): 549–63.

———. 2001b. 'Fracture of Wood under Mixed Mode Loading: II. Experimental Investigation of Picea Abies'. *Engineering Fracture Mechanics* 68 (5): 565–76.

Jirásek, M. 2016. 'Modelling of Localised Inelastic Deformation, LID 2016, Advanced Course, 19-23 September, Prague'.

Jobstl, RA., T. Bogensperger, and G. Schickhofer. 2008. 'In-Plane Shear Strength of Cross Laminated Timber (CLT)'. In *CIB-W18/41-12-3*, 1–23. St. Andrews, Canada.

Jobstl, RA., T. Bogensperger, G. Schickhofer, and G. Jeitler. 2004. 'Mechanical Behaviour of Two Orthogonally Glued Boards Technical Experiment to Determine Torsional Parameters'. In *WCTE*. Lahti, Finland.

Jorissen, André, and Massimo Fragiacomo. 2011. 'General Notes on Ductility in Timber Structures'. *Engineering Structures* 33 (11): 2987–97. doi:10.1016/j.engstruct.2011.07.024.

Kachanov, L.M. 1958. 'Time of Rupture Process under Creep Conditions'. *Izvestija Akademii Nauk SSSR, Otdelenie Techniceskich Nauk* 8: 26–31.

Kretschmann, D. 2010. *Wood Handbook: Wood as an Engineering Material. USDA - General Technical Report*. Vol. General Te. doi:General Technical Report FPL-GTR-190.

Leckie, F A, and D R Hayhurst. 1974. 'Creep Rupture of Structures'. *Proceedings of the Royal Society of London. Series A, Mathematical and Physical Sciences (1934-1990)* 340 (1622): 323–47. doi:10.1098/rspa.1974.0155.

Li, J. 2000. 'Three-Dimensional Effects in the Prediction of Flange Delamination in Composite Slin-Stringer Pull-off Specimens'. In *15th Conference of the American Society for Composites*. Texas, USA.

Li, J, and J K Sen. 2000. 'Analysis of Frame-to-Skin Joint Pull-Off Tests and Prediction of the Delamination Failure'. In *42nd AIAA/ASME/ASCE/AHS/ASC Structures, Structural Dynamics and Materials Conference*. Seattle, WA, USA.

Li, W., and T. Siegmund. 2002. 'An Analysis of Crack Growth in Thin-Sheet Metal Via a Cohesive Zone Model'. *Engineering Fracture Mechanics* 69: 2073–93.

Maiti, Spandan, and Philippe H. Geubelle. 2005. 'A Cohesive Model for Fatigue Failure of Polymers'. *Engineering Fracture Mechanics* 72 (5): 691–708. doi:10.1016/j.engfracmech.2004.06.005.

Martins, Sabrina A., Cláudio H.S. Dell Menezzi, Joana M. Ferraz, and Mário R. Souza. 2013. 'Bonding Behavior of Eucalyptus Benthamii Wood to Manufacture Edge Glued Panels'. *Maderas. Ciencia Y Tecnología* 15 (1): 79–92. doi:10.4067/S0718-221X2013.

Mestek, P., and P. Dietsch. 2014. 'Design Concept for CLT - Reinforced with Self-Tapping Screws'. In *Focus Solid Timber Solutions - European Conference on Cross Laminated Timber (CLT)*, 103–18.

Mestek, Peter, Kreuzinger Heinrich, and Stefan Winter. 2008. 'Design of Cross Laminated Timber (CLT)'. In *10th World Conference on Timber Engineering*, 156–63.

Moody, R C, and R Hernandez. 1997. 'Engineered Wood Products-A Guide for Specifiers, Designers and Users'. In *Chapter*, 1:1–39.

Muszynski, L, and M E Launey. 2010. 'Advanced Imaging Techniques in Wood-Based Panels Research.' In *Wood-Based Panels - An Introduction for Specialists. COST Action E49 Workshop*, edited by H Thoemen, M Irle, and M Sernek, 177–201. Brunel University Press.

Needleman, A. 1987. 'A Continuum Model for Void Nucleation by Inclusion Debonding'. *Journal of Applied Mechanics* 54 (3): 525. http://appliedmechanics.asmedigitalcollection.asme.org/article.aspx?articleid=1408962.

———. 1990. 'An Analysis of Decohesion along an Imperfect Interface'. *International Journal of Fracture* 42: 21–40.

Oppel, M., and K. Rautenstrauch. 2016. 'Multi-Faceted Elastic-Plastic Material Behaviour with Softening and Damage'. In *World Conference on Timber Engineering, WCTE 2016, August 22-25*. Vienna, Austria.

Orowan, E. 1949. 'Fracture and Strength of Solids'. *Report of Progress in Physics* 12.

Oudjene, M., and M. Khelifa. 2009. 'Finite Element Modelling of Wooden Structures at Large Deformations and Brittle Failure Prediction'. *Materials and Design* 30 (10): 4081–87. http://dx.doi.org/10.1016/j.matdes.2009.05.024.

Park, Kyoungsoo, Glaucio H. Paulino, and Jeffery R. Roesler. 2009. 'A Unified Potential-Based Cohesive Model of Mixed-Mode Fracture'. *Journal of the Mechanics and Physics of Solids* 57 (6): 891–908. doi:10.1016/j.jmps.2008.10.003.

Polastri, A., I. Giongo, S. Pacchioli, and M. Piazza. 2016. 'Structural Analysis of CLT Multi-Storey Buildings Assembled with the Innovative X-RAD Connection System: Case-Study on a Tall-Buildings'. In *World Conference on Timber Engineering, WCTE 2016, August 22-25*. Vienna, Austria.

Rabotnov, Y. N. 1968. 'Creep Rupture'. In *Proc. 12th International Congress of Applied Mechanics, Stanford*, 324–49. Springer.

Rice, J. R. 1980. 'The Mechanics of Earthquake Rupture'. In *Physics of the Earth's Interior*, 555–649. doi:10.1.1.161.3251.

Rice, J.R. 1968. 'A Path Independent Integral and the Approximate Analysis of Strain Concentration by Notches and Cracks'. *Journal of Appl. Mech.* 35: 379–

86.

Rinaldin, Giovanni, Claudio Amadio, and Massimo Fragiacomo. 2013. 'A Component Approach for the Hysteretic Behaviour of Connections in Cross-Laminated Wooden Structures'. *Earthquake Engineering & Structural Dynamics* 42 (13): 2023–42. http://doi.wiley.com/10.1002/eqe.2310.

Saavedra Flores, E. I., I. Dayyani, R. M. Ajaj, R. Castro-Triguero, F. A. DiazDelao, R. Das, and P. González Soto. 2015. 'Analysis of Cross-Laminated Timber by Computational Homogenisation and Experimental Validation'. *Composite Structures* 121. Elsevier Ltd: 386–94. doi:10.1016/j.compstruct.2014.11.042.

Saavedra Flores, E. I, K. Saavedra, J. Hinojosa, Y. Chandra, and R. Das. 2016. 'Multi-Scale Modelling of Rolling Shear Failure in Cross-Laminated Timber Structures by Homogenisation and Cohesive Zone Models'. *International Journal of Solids and Structures* 81. Elsevier Ltd: 219–32. doi:10.1016/j.ijsolstr.2015.11.027.

Saavedra Flores, E., K. Saavedra, J. Hinojosa, and R. Das. 2016. 'Progressive Damage Modelling in Cross-Laminated Timber Structures by Computational Homogenisation and Cohesive Zone Models'. In *World Conference on Timber Engineering, WCTE 2016, August 22-25*. Vienna, Austria.

Sandhaas, Carmen, Jan-Willem Van de Kuilen, and Hans Joachim Blass. 2012. 'Constitutive Model for Wood Based on Continuum Damage Mechanics'. In *World Conference on Timber Engineering*.

Scheider, I. 2001. 'Cohesive Model for Crack Propagation Analyses of Structures with Elastic – Plastic Material Behavior'. *GKSS Research Center, Geesthacht*, 1–41.

Scheider, I., and W. Brocks. 2003. 'Simulation of Cup–cone Fracture Using the Cohesive Model'. *Engineering Fracture Mechanics* 70 (14): 1943–61. doi:10.1016/S0013-7944(03)00133-4.

Sebera, Václav, Lech Muszyński, Jan Tippner, Melanie Noyel, Thomas Pisaneschi, and Benjamin Sundberg. 2015. 'FE Analysis of CLT Panel Subjected to Torsion and Verified by DIC'. *Materials and Structures* 48 (1–2): 451–59. http://link.springer.com/10.1617/s11527-013-0195-1.

Sharpe, WN. 2008. 'Springer Handbook Experimental Solid Mechanics'. *Springer*.

Siegmund, T, and W Brocks. 1999. 'Tensile Decohesion by Local Failure Criteria'. *Technische Mechanik* 4: 261–70. http://opensigle.inist.fr/handle/10068/264714.

Sikora, K, A M Harte, and D McPolin. 2014. 'Bond Quality of Cross-Laminated Timber from Irish Sitka Spruce'. *Civil Engineering Research in Ireland 2014*, 10–13. http://www.irishtimber.org/uploads/1/9/2/0/19209479/sikora_et_al__bond_quality_of_clt_from_irish_sitka_spruce_ah.pdf.

Sikora, Karol S., Daniel O. McPolin, and Annette M. Harte. 2016. 'Shear Strength and Durability Testing of Adhesive Bonds in Cross-Laminated Timber'. *The Journal of Adhesion* 92 (7–9): 758–77. doi:10.1080/00218464.2015.1094391.

Soltis, L., and D. Rammer. 1993. 'Shear Strength of Unchecked Glued-Laminated Beams'. *Forrest Products Journal* 53705 (1): 51 – 57.

Steiger, R, A Gulzow, and D Gsell. 2008. 'Non-Destructive Evaluation of Elastic Material Properties of Cross-Laminated Timber (CLT)'. In *Conference COST E*, 29–30. http://www.coste53.net/downloads/Delft/Presentations/COSTE53-Conference_Delft_Steiger_Guelzow_Gsell.pdf.

Stürzenbecher, R., K. Hofstetter, and J. Eberhardsteiner. 2010. 'Structural Design of Cross Laminated Timber (CLT) by Advanced Plate Theories'. *Composites Science and Technology* 70 (9). Elsevier Ltd: 1368–79. http://dx.doi.org/10.1016/j.compscitech.2010.04.016.

Sustersic, I., and B. Dujic. 2014. 'Seismic Strengthening of Existing Concrete and Masonry Buildings with Crosslam Timber Panels'. In *Materials and Joints in Timber Structures*, 713–23. Dordrecht: Springer Netherlands. http://link.springer.com/10.1007/978-94-007-7811-5_64.

Sustersic, I, and B Dujic. 2014. 'Seismic Shaking Table Testing of a Reinforced Concrete Frame with Masonry Infill Strengthened with Cross Laminated Timber Panels'. In *World Conference on Timber Engineering WCTE 2014, Quebec City, Canada 10-14 August*.

Sustersic, I, and Bruno Dujic. 2012. 'Simplified Cross-Laminated Timber Wall Modelling for Linear-Elastic Seismic Analysis'. In *International Council for Research and Innovation in Building and Construction, CIB-W18*, 1:1–7.

Sustersic, Iztok, Massimo Fragiacomo, and Bruno Dujic. 2012. 'Influence of the Connection Behaviour on the Seismic Resistance of Multi-Storey Crosslam Buildings'. *World Conference on Timber Engineering 2012: Architecture and Engineering Case Studies, WCTE 2012* 3 (Figure 1): 402–10.

Sutton, MichaelA. 2008. 'Digital Image Correlation for Shape and Deformation Measurements'. *Springer Handbook of Experimental Solid Mechanics SE - 20*, 565–600. http://dx.doi.org/10.1007/978-0-387-30877-7_20.

Thiel, A, and G Schickhofer. 2010. 'CLT Designer: The Software Tool for Designing Cross Laminated Timber Elements: 1D- Plate-Design'. In *World Conference on Timber Engineering, WCTE 2010*. Italy.

Turon, A., C. G. Dávila, P. P. Camanho, and J. Costa. 2007. 'An Engineering Solution for Mesh Size Effects in the Simulation of Delamination Using Cohesive Zone Models'. *Engineering Fracture Mechanics* 74 (10): 1665–82. doi:10.1016/j.engfracmech.2006.08.025.

Tvergaard, V, and J W Hutchinson. 1992. 'The Relation between Crack Growth Resistance and Fracture Process Parameters in Elastic-Plastic Solids'. *Journal of Mechanics and Physics of Solids* 40 (6): 1377–97. doi:10.1016/0022-5096(92)90020-3.

Unterwieser, H, and Gerhard Schickhofer. 2014. 'Characteristic Values and Test Configurations of CLT with Focus on Selected Properties'. *Focus Solid Timber Solutions - European Conference on Cross Laminated Timber (CLT)*, 35–65.

Ural, Ani, Venkat R. Krishnan, and Katerina D. Papoulia. 2009. 'A Cohesive Zone Model for Fatigue Crack Growth Allowing for Crack Retardation'. *International Journal of Solids and Structures* 46 (11–12): 2453–62. doi:10.1016/j.ijsolstr.2009.01.031.

Vallée, Till, Thomas Tannert, and Simon Fecht. 2015. 'Adhesively Bonded Connections in the Context of Timber Engineering – A Review'. *The Journal of Adhesion*, September, 1–31. doi:10.1080/00218464.2015.1071255.

Volokh, K. Y. 2004. 'Comparison between Cohesive Zone Models'. *Communications in Numerical Methods in Engineering* 20 (11): 845–56. doi:10.1002/cnm.717.

Wallner, G. 2004. 'Versuchstechnische Ermittlung Der Verschiebungskenngrößen von Orthogonal Verklebten Brettlamellen'. Master's thesis, Graz University of Technology (in German).

Zou, Z., S.R. Reid, S. Li, and P.D. Soden. 2001. 'Mode Separation of Energy Release Rate for Delamination in Composite Laminates Using Sublaminates'. *International Journal of Solids and Structures* 38: 2597–2613.